ADVANCED FUNCTIONAL MATERIALS
www.afm-journal.de

Lead-Free Halide Perovskite Materials and Optoelectronic Devices: Progress and Prospective

*Iago López-Fernández, Donato Valli, Chun-Yun Wang, Subarna Samanta, Takuya Okamoto, Yi-Teng Huang, Kun Sun, Yang Liu, Vladimir S. Chirvony, Avijit Patra, Juliette Zito, Luca De Trizio, Deepika Gaur, Hong-Tao Sun, Zhiguo Xia, Xiaoming Li, Haibo Zeng, Iván Mora-Seró, Narayan Pradhan, Juan P. Martínez-Pastor, Peter Müller-Buschbaum, Vasudevanpillai Biju, Tushar Debnath, Michael Saliba, Elke Debroye, Robert L. Z. Hoye, Ivan Infante, Liberato Manna, and Lakshminarayana Polavarapu**

Halide perovskites, in the form of thin films and colloidal nanocrystals, have recently taken semiconductor optoelectronics research by storm, and have emerged as promising candidates for high-performance solar cells, light-emitting diodes (LEDs), lasers, photodetectors, and radiation detectors. The impressive optical and optoelectronic properties, along with the rapid increase in efficiencies of solar cells and LEDs, have greatly attracted researchers across many disciplines. However, most advances made so far in terms of preparation (colloidal nanocrystals and thin films), and the devices with highest efficiencies are based on Pb-based halide perovskites, which have raised concerns over their commercialization due to the toxicity of Pb. This has triggered the search for lower-toxicity Pb-free halide perovskites and has led to significant progress in the last few years. In this roadmap review, researchers of different expertise have joined together to summarize the latest progress, outstanding challenges, and future directions of Pb-free halide perovskite thin films and nanocrystals, regarding their synthesis, optical spectroscopy, and optoelectronic devices, to guide the researchers currently working in this area as well as those that will join the field in the future.

1. Introduction

Over the last decade, halide perovskites (HPs) with a general formula ABX_3 (where A = $CH_3NH_3^+$ (MA), $HC(NH_2)_2^+$ (FA), or Cs^+; B = Pb^{2+} or Sn^{2+}; X = Cl, Br or I) have emerged at the forefront of materials for high-performance optoelectronics.[1–5] Although they have been known since the late 19th century,[6,7] they have regained broad attention after the demonstration of their potential as photoactive materials for solar cells in 2009 and for light emission in 2012 by Kojima et al.[1,8], and subsequently for LEDs in 2014 by Tan et al.[9] The 2012 breakthroughs[10,11] in HP solar cells ignited research into this field, which then spread into different sub-areas of optoelectronics.[3,4] Since then, this class of materials, especially the lead halide perovskites (LHPs), has been greatly exploited in terms of their chemistry,

I. López-Fernández, Y. Liu, D. Gaur, L. Polavarapu
CINBIO
Universidade de Vigo
Materials Chemistry and Physics Group
Department of Physical Chemistry
Campus Universitario Lagoas Marcosende
Vigo 36310, Spain
E-mail: lakshmi@uvigo.es

The ORCID identification number(s) for the author(s) of this article can be found under https://doi.org/10.1002/adfm.202307896

DOI: 10.1002/adfm.202307896

D. Valli, E. Debroye
Department of Chemistry
KU Leuven
Celestijnenlaan 200F, Leuven 3001, Belgium

C.-Y. Wang, M. Saliba
Institute for Photovoltaics (ipv)
University of Stuttgart
Pfaffenwaldring 47, 70569 Stuttgart, Germany

C.-Y. Wang, M. Saliba
Helmholtz Young Investigator Group FRONTRUNNER
IEK5-Photovoltaik
Forschungszentrum Jülich
52425 Jülich, Germany

S. Samanta, T. Debnath
Centre for Nanotechnology
Indian Institute of Technology Guwahati
Guwahati, Assam 781039, India

optical spectroscopy, and optoelectronic devices.[2,12–15] They have received a great deal of attention from researchers working on solar cells, LEDs, lasers, and X-ray detectors.[3,12,16–20] The optical and electrical properties of LHPs, such as strong light absorption, tunable bandgap, long charge-carrier lifetime and diffusion length, solution processability, and high defect tolerance are ideal for optoelectronic devices. As a result of the intense efforts of researchers across the globe, the power conversion efficiency (PCE) of LHP single-junction solar cells has increased from 3.8% to over 25%,[1,21] while the efficiency of HP-silicon tandem solar cells has surpassed 32%.[22] In parallel, there has also been significant progress in HP LEDs, with external quantum efficiencies (EQEs) surpassing 25% for both green and red colors.[23–25] Currently, perovskite solar cells and LEDs are being intensively investigated to further improve their EQE and long-term stability by device engineering and device encapsulation, tuning the composition, and reducing the trap states through passivation.[2,4,15,18,26,27]

Parallel to all this, we have also witnessed important developments in the field of colloidal HP nanocrystals (NCs) in terms of shape and composition-controlled synthesis, self-assembly, understanding of their optical properties, and their applications to optoelectronic devices.[2,12,18,19,28–30] Unlike bulk perovskites, the optical properties of colloidal NCs are tunable not only by their composition but also through quantum confinement effects.[2,19,28,31] Most notably, the near-unity photoluminescence quantum yield (PLQY) of LHP NCs makes them promising sources for light-emitting applications including LEDs, lasers, and single-photon generation.[2] In addition, they have also been used in the fabrication of solar cells, even though their PCEs are relatively low compared to that of bulk thin films (over 25% for bulk thin films versus over 15% for colloidal NCs).[18,2,32–34] Despite great success, LHP NCs are currently undergoing further advancements regarding their colloidal synthesis, screening of ligands for improving the stability and PLQY, and efficiency of the corresponding optoelectronic devices. Besides, recently there has been an increasing interest in HP (bulk and NCs)-based X-ray detectors, and significant advancements have been made in the fabrication of high-sensitivity radiation detectors.[35–37]

Despite rapid progress in LHPs (thin films and NCs) with a steep increase in efficiencies of the corresponding optoelectronic devices, their toxicity and instability (long-term as well as operational) has been a major concern to advance the field in a way similar to that of silicon-based devices.[38–41] The instability issues are being tackled by using 2D/3D perovskites and through surface passivation as well as device encapsulation.[2,41,42] Still, the lifetime of HP solar cells is far behind that of silicon-based solar cell modules (25 years) and the operational stability of LEDs is even worse, with some of the best-reported lifetimes being only tens of hours.[43,44] These LHPs are very sensitive to heat, air, light, moisture, and water, and their degradation releases compounds such as PbI_2 that can have a very adverse impact on the environment.[45,46] This is especially problematic when PbI_2 (or other compounds containing heavy metal ions) dissolves in water systems, leading to the accumulation of toxic metal ions, which then can be up-taken by living organisms.[47]

The ideal scenario would be the replacement of Pb with nontoxic elements in halide perovskites without compromising

T. Okamoto, V. Biju
Research Institute for Electronic Science
Hokkaido University
Sapporo, Hokkaido 001–0020, Japan

T. Okamoto, V. Biju
Graduate School of Environmental Science
Hokkaido University
Sapporo, Hokkaido 060–0810, Japan

Y.-T. Huang, R. L. Z. Hoye
Inorganic Chemistry Laboratory
Department of Chemistry
University of Oxford
South Parks Road, Oxford OX1 3QR, UK

K. Sun, P. Müller-Buschbaum
Technical University of Munich
TUM School of Natural Sciences
Department of Physics
Chair for Functional Materials
James-Franck-Str. 1, 85748 Garching, Germany

Y. Liu, X. Li, H. Zeng
MIIT Key Laboratory of Advanced Display Material and Devices
School of Materials Science and Engineering
Nanjing University of Science and Technology
Nanjing 210094, China

V. S. Chirvony, J. P. Martínez-Pastor
UMDO
Instituto de Ciencia de los Materiales
Universidad de Valencia
Valencia 46980, Spain

A. Patra, N. Pradhan
School of Materials Sciences
Indian Association for the Cultivation of Science
Kolkata 700032, India

J. Zito, L. De Trizio, L. Manna
Istituto Italiano di Tecnologia – IIT
Via Morego 30, Genova 16163, Italy

H.-T. Sun
Research Center for Materials Nanoarchitectonics (MANA)
National Institute for Materials Science (NIMS)
Tsukuba, Ibaraki 305-0047, Japan

Z. Xia
School of Physics and Optoelectronics
State Key Laboratory of Luminescent Materials and Devices and Guangdong Provincial Key Laboratory of Fiber Laser Materials and Applied Techniques
South China University of Technology
Guangzhou, Guangdong 510641, P. R. China

I. Mora-Seró
Institute of Advanced Materials (INAM)
Universitat Jaume I
Castelló de la Plana, Castelló 12006, Spain

P. Müller-Buschbaum
Heinz Maier-Leibnitz Zentrum (MLZ)
Technical University of Munich
Lichtenbergstr. 1, 85748 Garching, Germany

I. Infante
BCMaterials
Basque Center for Materials
Applications, and Nanostructures
UPV/EHU Science Park
Leioa 48940, Spain

I. Infante
Ikerbasque
Basque Foundation for Science
Bilbao 48009, Spain

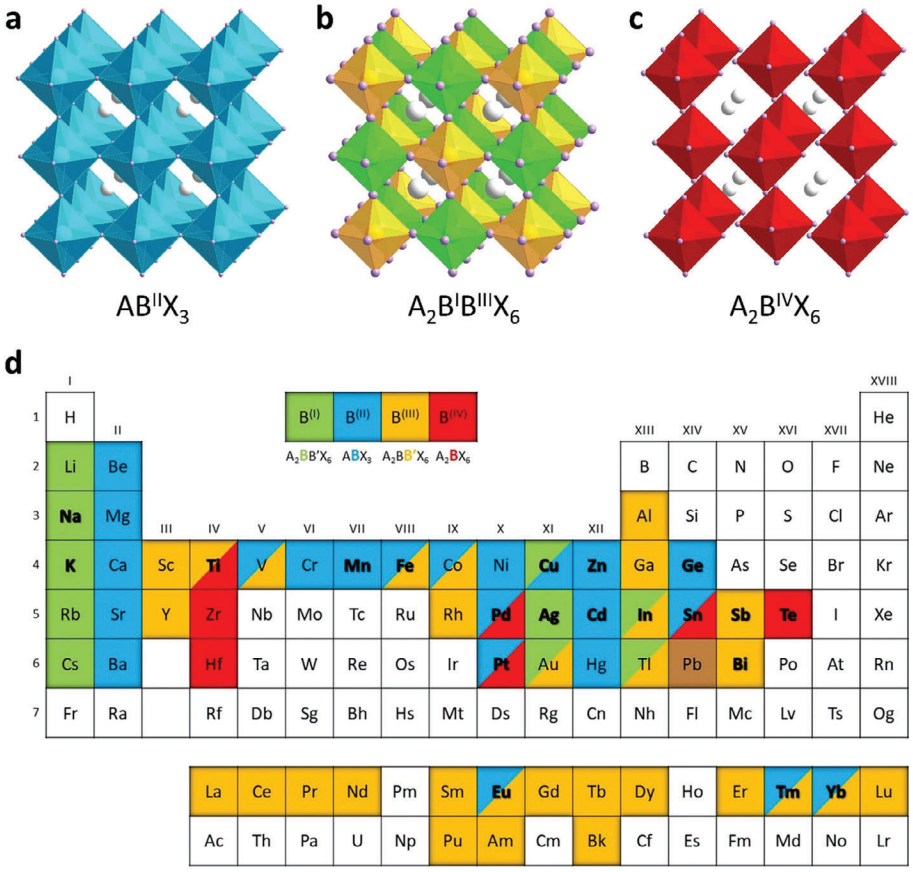

Figure 1. Crystal structures of ABX_3 HPs (a), $A_2B^IB^{III}X_6$ DPs (b), and $A_2B^{IV}X_6$ vacancy-ordered perovskites (c). d) Periodic table highlighting the elements that can replace Pb in LHPs. The elements that can occupy the B^I, B^{II}, B^{III}, and B^{IV} sites of the crystal structures shown in (a–c) are labeled with green, blue, yellow, and red, respectively.

performance. Several studies have tackled this issue and have proposed different elements that could substitute the lead atoms based on similarity in size, charge, chemical reactivity, properties, and structural tolerance.[48–52] **Figure 1** reports the structure of HPs, halide elpasolites (double perovskites (DPs)), and vacancy-ordered perovskites with various possible elements in the periodic table (see below). The elements that could fit in the B-site (with different oxidation states) of each structure are labeled with the same colour, while the elements that have been more frequently reported are highlighted in bold. Among them, the elements in the same group as Pb (Group 14), which are tin (Sn^{2+}) and germanium (Ge^{2+}), have been the first choices (Figure 1). Especially Sn-based HPs have received significant attention because of their properties that are indeed similar to those of LHPs. However, the reported performances of Sn (or Ge)-based optoelectronic devices are significantly poorer than those of LHPs.[52] In addition, they exhibit low stability due to the rapid oxidation of Sn^{2+} and Ge^{2+} to Sn^{4+} and Ge^{4+} under environmental conditions. As a result, it has been extremely challenging to synthesize stable Sn (or Ge)-based HP thin films and NCs with the same level of control achieved for LHPs.[2,5,53] Moreover, there is a debate that Sn is even more toxic than Pb, although this aspect needs to be investigated in more detail.[38] Despite these issues, there has been some success in the size and shape-controlled synthesis of colloidal $ASnX_3$ perovskite NCs,[54–56] and significant advances have been made also in the fabrication of Sn-based 2D perovskite thin films.[57,58] Ge-based compounds are much less toxic, but their poor stability and performance limit their use. Moreover, only certain Ge-perovskites such as $CsGeI_3$ exhibit suitable bandgap for solar cells.[52,59] Another possible replacement for Pb^{2+} ions is a combination of a monovalent cation and a trivalent cation, resulting in the formation of DPs with the general formula $A_2B^IB^{III}X_6$.[2,17] As shown with a color code in Figure 1, various combinations of DPs with different B^I and B^{III} cations (B^I (green) = Li, Na, K, Rb, Cs, Ag; B^{III} (yellow) = Al, Ga, In, Sb, Bi) are theoretically possible according to the Goldschmidt's tolerance factor.[48–51] Among them, Cs_2AgBiX_6 and $Cs_2(Ag/Na/K)(Bi/In)X_6$ stand out as the most extensively studied ones for their high stability, low toxicity and long charge carrier lifetime (comparable to those of LHPs).[60] There are also reports of DPs where the B^{III} cation is a lanthanide.[61,62] Another interesting class of materials is that of vacancy-ordered DPs, with formula $A_2B^{IV}X_6$, which can be thought of as resulting from the substitution of B^I and B^{III} ions by a B^{IV} cation and a vacancy.[63,64] $A_3B_2X_9$ is another type of Pb-free system that has been investigated, although, strictly speaking, it does not belong to the perovskite family based on its crystal structure.

Table 1. Summary of synthesis methods used for THP NCs with various shapes.

Serial Number	Composition	Synthetic Method	Shape of NCs	Reference
1.	$CsSnX_3$ (X = Cl, Br, I)	HI	Nanocubes	[55]
2.	$FASnI_3$	HI	Nanocubes	[66]
3.	$CsSnI_3$ + $(R\text{-}NH_3^+)_2Cs_{n-1}Sn_nI_{3n+1})$ nanosheets	HI	Nanocubes + Nanosheets	[56]
4.	$CsSnI_3$	HI	Nanocubes	[71]
5.	Cs_2SnI_6	HI	Quantum Dots, Nanorods, Nanowires, Nanobelts, Nanoplatelets	[78]
6.	$(OCTAm)_2SnBr_4$	Facile aqueous acid-based method	2D Layered Structure	[75]
7.	$CsSnI_3$	HI	Nanoplatelets or Nanosheets	[67]
8.	$L_2[ASnX_3]_{n-1}SnX_4$, where A = FA, and X = Cl, Br, or I	LARP	Nanoplatelets	[74]
9.	$CsSnX_3$ (X = Br, I)	CVD	Nanowires	[81]
10.	$CsSnX_3$ (X = Cl, Br, I)	CVD	Nanowires	[82]
11.	$CsSnX_3$ (X = Cl, Br, I)	HI	Nanocubes	[54]
12.	PEA_2SnX_4 (X = Br, I)	LARP	Nanoplatelets	[76]
13.	$MASnBr_{3-x}I_x$	HI	Quantum Dots	[73]
14.	$CsSnBr_3$	HI	Nanocages	[84]
15.	$CsSnX_3$ (X = Cl, Br, I)	Solvothermal	nanorods	[83]
16.	Cs_4SnBr_6	HI	Hexagonal	[68]
17.	Cs_2SnI_6	HI	Quasi-spherical	[79]
18.	$(4Tm)_2SnI_4$	LARP	–	[77]
19.	$FASnI_3$	HI	Nanocubes	[69]
20.	$CsSnX_3$ (X = Cl, Br, I)	HI	Nanocubes	[70]
21.	Cs_2SnI_6	Metal ion metathesis	Nanoplatelets	[80]

This review provides a discussion on the state-of-the-art of Pb-free perovskite materials regarding their preparation, optical properties (linear and nonlinear), degradation mechanisms, and their application to solar cells, LEDs, and X-ray detectors. In terms of materials, we will discuss both colloidal NCs as well as bulk thin films (2D layered and 3D). As a note of caution, while we will discuss the synthesis of colloidal HP NCs, the discussion on optoelectronic applications is mainly focussed on thin films, powders, or single crystals. This is because the potential of Pb-free colloidal HP NCs for optoelectronic devices is still relatively unexplored owing to the instability of some compositions (for example the Sn^{2+}-based ones) and their low photoluminescence. On the other hand, the optical properties of Pb-free HP NCs as well as thin films in terms of their absorption, photoluminescence, charge carrier dynamics, spin relaxation dynamics, and charge transport properties will be briefly summarized. The Pb-free HP that will be discussed here include $ASnX_3$, $A_2B^IB^{III}X_6$ DPs, and vacancy-ordered $A_2B^{IV}X_6$. We will highlight the research progress in these systems in terms of their fabrication and efficiencies of the corresponding optoelectronic devices along with the outstanding challenges. Finally, an outlook of these Pb-free HP material systems and devices will be presented in terms of their synthesis/fabrication with improved stability and efficiency, having in mind the ultimate goal of their translation from the laboratory to real-world applications.

2. Synthesis of PB-Free Perovskite Materials

2.1. Synthesis of Tin Halide Perovskite NCs

One of the outstanding challenges in the field of colloidal halide perovskite NCs is to synthesize stable tin halide perovskite (THP) NCs.[2] Despite the great progress in the shape-controlled synthesis of LHP NCs, only a few reports have demonstrated to date the synthesis of $ASnX_3$ counterparts (**Table 1**).[2,54,55,65–67] A wide range of approaches (such as the hot injection (HI), ligand-assisted reprecipitation (LARP), hydrothermal, ultrasonication, and emulsion synthesis, etc.)[2] have been employed for the preparation of LHP NCs. Among all, HI and LARP are the most commonly adapted approaches for the synthesis of THP NCs.[2,46,54,55,65–67] The THP NCs can be broadly classified into three categories: i) $ASnX_3$ (A = Cs, FA, MA; X = Cl, Br, I) type 3D HPs, ii) A'_2SnX_4 (A' = organic ligands; X = Cl, Br, I) type 2D layered perovskites and iii) A_2SnX_6 (A = Cs, FA, MA; X = Cl, Br, I) type perovskites. In this section, we summarize the main achievements in these directions, point out the key issues that remain unresolved, and present our perspectives on future research directions.

$ASnX_3$ Type **3D** Perovskite NCs. The synthesis of $ASnX_3$-type $CsSnX_3$ NCs via the HI route was first reported by Jellicoe et al.[54] They synthesized the NCs by dissolving SnX_2 salts in tri-n-octyl

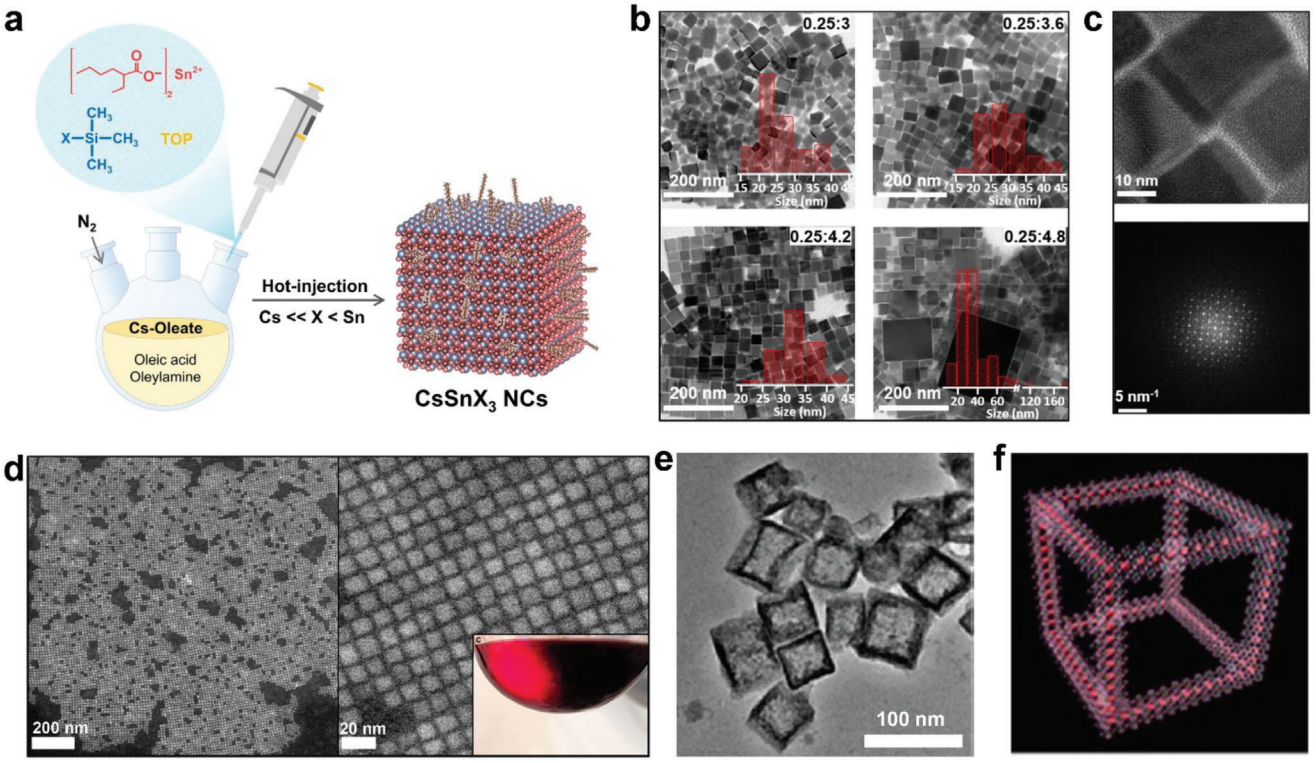

Figure 2. a) Schematic of the synthesis of $CsSnX_3$ (X = Cl, Br, I) perovskite NCs via the HI route. b) Low-resolution transmission electron microscopy (TEM) images of $CsSnI_3$ NCs with different Cs:Sn ratios. The insets show the histograms of particle size for the corresponding $CsSnI_3$ NCs. c) HRTEM image and corresponding selected area electron diffraction pattern of the sample synthesized with a Cs:Sn ratio of 0.25:4.2. The panels a, b and c are adapted with permission.[55] Copyright 2021, American Chemical Society. d) Dark-field scanning transmission electron microscopy (STEM) images of $FASnI_3$ NCs at two different magnifications. The figure is adapted with permission.[66] Copyright 2023, American Chemical Society. e) TEM image of $CsSnBr_3$ nanocages. f) Corresponding schematic model of a nanocage structure. The panels e and f are adapted with permission.[72] Copyright 2017, Tsinghua University Press and Springer-Verlag Berlin Heidelberg.

phosphine (TOP) followed by their injection into a Cs-oleate precursor solution containing oleic acid (OA) and oleylamine (OLA) as ligands. However, the obtained NCs showed poor stability and low PLQYs. Later, it was found that the change of capping ligands can tune the morphology of $CsSnI_3$ from nanocubes to nanoplatelets (NPls), though the PLQY is still low.[67] The similarity between these two works is the use of SnI_2 as the source of both Sn^{2+} and I^-, resulting in a Sn/I ratio of 1:2 in the reaction medium. From the perspective of synthetic chemistry, a more flexible approach that enables facile tuning of reactants (different Sn/I ratios and ligands) is needed to suppress the formation of detrimental structural defects (Sn and halide vacancies) causing nonradiative charge-carrier recombination.[55,56,66–71]

In a recent report, Liu et al. developed a theory-guided colloidal HI synthesis strategy to obtain high-quality $CsSnI_3$ NCs by the rational fine-tuning of the reactant ratio in a wide range.[55] **Figure 2**a shows the schematic of the synthesis of THP NCs where Cs_2CO_3 was initially loaded into a three-neck flask along with octadecene (ODE), OA, and OLA and was then degassed at 80 °C. Subsequently, a mixture of tin(II) 2-ethylhexanoate ($Sn(Oct)_2$), trimethylsilyl iodide (TMSI), and TOP was swiftly injected into the reaction flask at 180 °C, which led to a rapid salt metathesis reaction and resulted in fast nucleation and growth of $CsSnI_3$ NCs. It has been found that the relative amount of the precursors plays a crucial role in governing the phase purity, size distribution, and optical properties of NCs, and importantly, a Sn-rich condition is required for the growth of THP NCs with a high PLQY. All these experimental results are in good agreement with the predictions based on density functional calculations (DFT) and molecular dynamics simulations (MD). Figure 2b presents low-resolution TEM images of the resulting NCs, indicating that with the increase of the Sn amount (when going from a Cs:Sn ratio of 0.25:3 to 0.25:4.8), the average size of cubic-shaped NCs increases from 26 nm (for 0.25:3) to 37 nm (for 0.25:4.8). Figure 2c shows the high-resolution TEM and corresponding selected area electron diffraction pattern of the 0.25:4.2 sample, in which it is possible to appreciate the single-crystalline nature of the NCs. It is noted that the synthesis of $CsSnI_3$ NCs was carried out in an inert atmosphere owing to their extreme sensitivity to air. In a similar synthesis, Wang et al.[71] tried to investigate the role of surfactants on the growth kinetics of $CsSnI_3$ NCs and revealed the formation of intermediate complexes between zwitterionic phosphatidylcholine and the precursors. It was found that the steric hindrance of branched fatty acid side-chains of phosphatidylcholine can regulate the growth kinetics of $CsSnX_3$, enabling the synthesis of $CsSnX_3$ NCs with a PLQY of 12%, which is among the highest ever reported.[71] Interestingly, Kang et al. found that the use of stannous oxalate (SnC_2O_4), Cs_2CO_3, and NH_4I as the precursors of Sn, Cs, and I, respectively, yields $CsSnI_3$ NCs with greatly enhanced stability yet having a low PLQY.[70] In light of

these results, we envisage that simultaneously tuning the precursor ratio in a wide range (as discussed above) and using some specific capping ligands, e.g., multifunctional ligands, that can passivate the NCs' surface might yield highly luminescent, highly stable $CsSnI_3$ NCs.

It was also found that the type of precursors could affect the in-situ colloidal stability of THP NCs and their final morphology. For example, Wang et al. used tin(II) 2-ethylhexanoate ($Sn(Oct)_2$) and $MgBr_2{\cdot}6H_2O$ as the separate precursors for Sn and Br, respectively, for the synthesis of $CsSnBr_3$ NCs by the HI approach.[72] In this particular case, a hollow nanocage morphology was achieved via nanocubes self-assembly at >200 °C (Figures 2e, f). Notably, the selection of tin precursor, i.e., $Sn(Oct)_2$ in this case, is the key factor for the self-assembly process via the oriented attachment of the branched ethylhexanoate group. These nanocages feature a superior stability againstmoisture, oxygen, and light at ambient conditions with respect to THP nanocubes. Nevertheless, it should be noted that the shape-controlled synthesis of stable colloidal THP NCs is still in an early stage compared to that of LHP NCs in terms of the rational control over the reactivity of reactants used for the synthesis, understanding of reaction mechanisms and reproducibility of the synthesis.[56,65] In this regard, Gahlot et al. attempted to obtain stable, tunable, and monodisperse $CsSnI_3$ NCs exhibiting well-defined excitonic peaks by an optimized synthetic route.[56] It was found that the presence of excess SnI_2 precursor and the substoichiometric Sn:ligand ratio are the keys to obtaining stable $CsSnI_3$ NCs. Furthermore, optical and structural characterizations along with first-principle DFT calculations suggested the presence of 2D $(R\text{-}NH_3^+)_2SnI_4$ nanosheets, where $R = C_{18}H_{35}$. Under specific synthetic conditions, stable mixtures of 3D $CsSnI_3$ NCs and 2D (i.e., Ruddlesden–Popper $(R\text{-}NH_3^+)2Cs_{n-1}Sn_nI_{3n+1}$ with $n > 1$) nanosheets can be obtained, although their photophysical properties need to be investigated in more details. Very recently, Zhang et al.[65] reported on the mechanistic insight into the precursor chemistry of $CsSnI_3$ perovskite NCs through a combination of various characterization techniques. They identified that the active intermediate complexes, polymeric alkanoate iodides that form via the reaction of the iodide source with oligomers present in the tin (II) carboxylates, play a role in governing the reactivity of the tin-iodide precursor, resulting in the variation in the size, size uniformity, and PLQY of $CsSnI_3$ NCs.[65] The understanding of the reaction mechanism in the synthesis of THP NCs would not only lead to improved synthesis strategies, but also might offer guidelines for fabricating high-quality polycrystalline films that can be used for optoelectronic devices such as LEDs and photovoltaics, considering the similar defect formation mechanisms in both LHP NCs and polycrystalline films.

There are also a few reports on the synthesis of organic-inorganic hybrid THP NCs. In 2021, Dai et al. reported the synthesis of monodisperse $FASnI_3$ perovskite NCs by the LARP approach (**Figure 3**a). They found that $FASnI_3$ NCs of different sizes can be readily synthesized by a swift injection of FA oleate precursor into SnI_2 precursor under vigorous stirring at different temperatures.[69] The quantized energy levels are strongly dependent on the size of the NCs as shown in Figure 3b,c. Interestingly, these quantum-confined NCs with separate energy states slow down the relaxation of hot carriers by two orders of magnitude compared to LHP NCs under the same excitation conditions. The observed build-up time of the ground-state bleach at the band edge is two orders of magnitude slower in $FASnI_3$ NCs than in LHP bulk and NCs, which the authors attribute to a phonon bottleneck effect (see also the optical properties section of this review for more details).[69] Similarly, Dirin et al. synthesized $FASnI_3$ NCs with good size distribution via the HI approach.[66] They found that 10 nm $FASnI_3$ NCs exhibit an unusually large band gap, which cannot be explained merely by quantum confinement effects. The distortion of the lattice through the split of I-sites was thus proposed (Figure 3d), considering that a reduction in the symmetry and bending of the Sn−I−Sn bond can reduce the overlap of Sn and I 5p orbitals. In addition, the HI approach has also been used for the synthesis of $MASnBr_{3-x}I_x$ and $Cs_xFA_{1-x}SnI_3$ NCs.[69,73] We point out that all reported hybrid THP NCs exhibit extremely low PLQYs, suggesting a high density of structural defects contributing to nonradiative recombination. Future studies should be focused on boosting their PLQYs, understanding the reaction mechanism, as well as the unusual photophysical properties of THP NCs.

A'_2SnX_4-type **2D layered** Perovskites. In 2016, Weidman et al. first reported the LARP synthesis of A'_2SnX_4-type 2D layered perovskite NPls with $L_2[ASnX_3]_{n-1}SnX_4$ formula, where L represents long-chain ligands such as butylammonium or octylammonium, A is Cs, FA, or MA, and n is the number of octahedral units cells (thickness) of the NPls.[74] The layered NPls were synthesized by dissolving the respective precursor salts, i.e., AX, SnX_2, and LX in dimethylformamide (DMF) followed by mixing them with toluene. The thickness of the NPLs can be tuned by varying the $LX/SnX_2/AX$ ratio. Here, the long-chain organic ligand occupies the A-cations sites on the surface and thus hinders the growth of NCs along one dimension (Figures 4a,b), leading to the formation of layered NPls. In contrast to 3D NCs, these 2D perovskites exhibit a higher PLQY and stability against humidity. For instance, Wang et al. synthesized 2D layered $(OCTAm)_2SnBr_4$ crystals with near-unity PLQY by a facile aqueous acid-based synthetic method.[75] At first, stannous oxide powder was dissolved in hydrobromic acid by sonication, followed by the addition of aqueous H_3PO_2 to prevent the oxidation of Sn (II). Octylamine was then added to the above reaction mixture. The solution was then heated to 80 °C for 30 min and then cooled at 4 °C to obtain $(OCTAm)_2SnBr_4$ crystals. **Figure 4**c illustrates the typical 2D $(octylammonium)_2SnBr_4$ layered perovskite, wherein $SnBr_6$ octahedral layers are separated by octylammonium ions. Figure 4d presents the high-resolution TEM images along with the corresponding FFT pattern that shows the interplanar spacing to be 20 Å having a proper matching with the (100) plane. Interestingly, the PLQY of the 2D layered perovskite sample remains unchanged even after 240 days of storage under ambient air and humidity

In addition, layered NPls can be obtained by replacing the A-site cation with larger organic cations such as 2-phenylethan-1-aminium ($PEA = C_6H_5(CH_2)_2\ NH_3^+$)[76] and 2-(3″′,4′-dimethyl-[2,2′:5′,2″:5″,2″′-quaterthiophen]−5-yl) ethan-1-ammonium (4Tm).[77] Both, PEA_2SnX_4 and $(4Tm)_2SnI_4$ layered NPls with high PLQYs can be synthesized via the LARP approach. Figure 4e shows the schematic illustration of well-aligned (left) and disordered (right) 2D PEA_2SnX_4 (X = Cl, Br, I) NPls, while Figure 4f presents a schematic model of the $(4Tm)_2SnI_4$

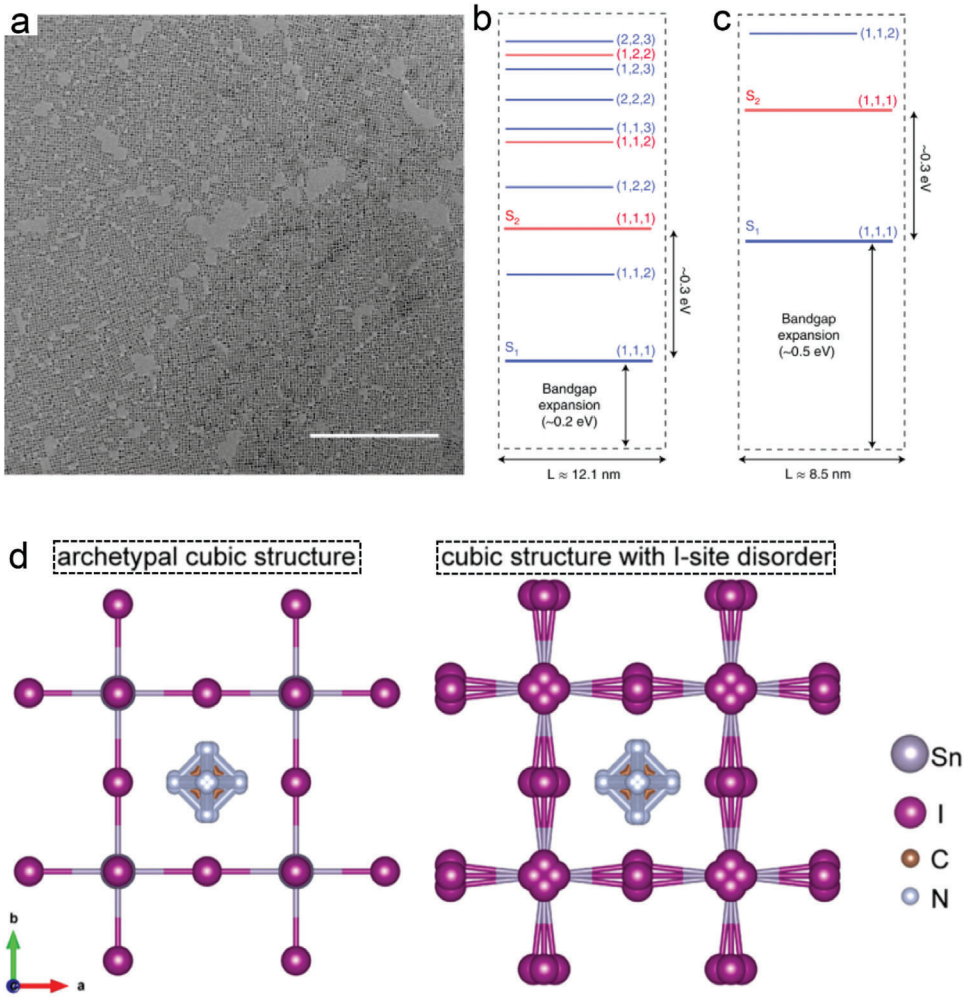

Figure 3. a) TEM image of $FASnI_3$ NCs (scale bar, 500 nm). b,c) Quantized energy levels in ≈12.1 nm and ≈8.5 nm $FASnI_3$ NCs, assuming an ideal quantum box model. Reproduced with permission.[69] Copyright 2021, Springer Nature Limited. d) Schematic of archetypal cubic structure (left) and cubic structure with I-site disorder (right). Reproduced with permission.[66] Copyright 2023, American Chemical Society.

crystal. It is noted that thin-film field-effect transistors made using $(4Tm)_2SnI_4$ showed enhanced hole mobility up to 2.32 $cm^2 V^{-1} s^{-1}$ with a dramatically improved stability over the previous benchmark material $(PEA)_2SnI_4$.[77] These 2D layered THPs have also been exploited for LEDs, while the NC-based LEDs face severe challenges regarding their stability (discussed in the section of Sn-based LEDs).

Vacancy-ordered A_2SnX_6 type double perovskite. The vacancy-ordered A_2SnX_6 DPs are typically prepared by the HI approach. Wang et al. synthesized Cs_2SnI_6 NCs of different shapes by injecting Cs-oleate into a reaction mixture of SnI_4, ODE, OA, and OLA.[78] **Figure 5**a depicts a sketch of their synthesis route of Cs_2SnI_6 DPs along with a photograph of the as-prepared samples under UV light. Under their reaction conditions, they observed the initial formation of Cs_2SnI_6 quantum dots which evolved by time into nanorods, then to nanowires (NWs), and finally nanobelts and NPls. Besides, other morphologies of Cs_2SnI_6 NCs such as ligand-free quasi-spheres of different sizes (Figure 5b,c)[79] and NPls were also previously reported.[80] The size of the quasi-spherical Cs_2SnI_6 NCs is controllable by the reaction temperature of the HI synthesis, and the various optical properties (photoinduced absorption (PIA), absorption maximum, transient absorption bleach (TA bleach), PL, and diffuse reflectance (DR)) of the NCs are strongly dependent on their average diameter, as illustrated in Figure 5b.[79]

We point out that other methods such as chemical vapor deposition (CVD) and solvothermal reaction were also used for the synthesis of tin-based nanostructures such as $CsSnX_3$ NWs and NCs.[81–83] Although some efforts have been devoted to the synthesis of THP NCs (as discussed above), we should note that the stability and photophysical properties (*e.g.*, PLQYs) of THP NCs are inferior to their Pb-based counterparts. Future studies should focus on developing more rational synthetic approaches to allow effective suppression of detrimental structural defects in THP NCs, and boosting their stability in harsh environments. This might be achieved by ligand engineering or by forming THPs in porous matrices such as TiO_2 and SiO_2.

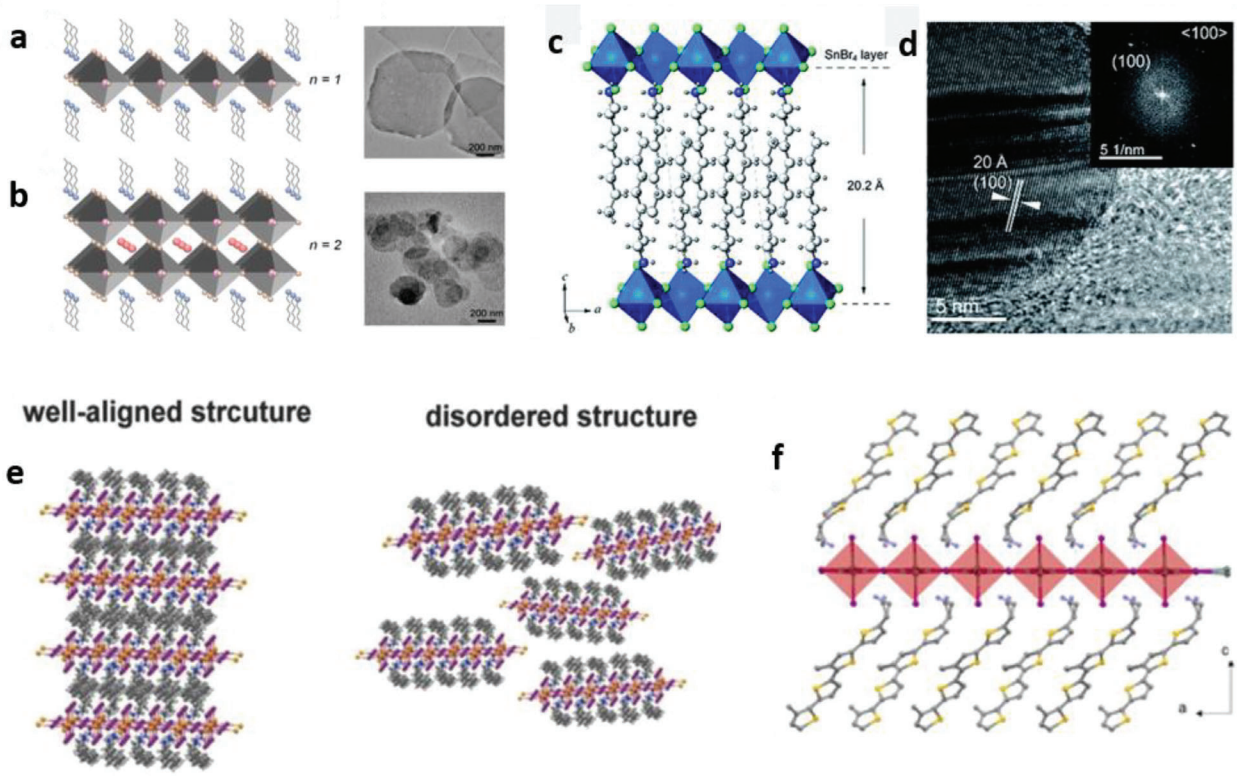

Figure 4. 2D layered Sn-based perovskite NPls: a,b) Schematic illustration of 2D $L_2[ASnI_3]_{n-1}SnI_4$ NPls for n = 1 and 2, respectively, and corresponding TEM image of the NPls for n = 1 and 2 (right side). Reproduced with permission.[74] Copyright 2016, American Chemical Society. c,d) Schematic of the crystal structure and HRTEM image of $(OCTAm)_2SnBr_4$ NCs, respectively. Reproduced under the terms of CC BY-NC 3.0.[75] Copyright 2019, The Authors, published by The Royal Society of Chemistry. e) Schematic illustration of well-aligned (left) and disordered (right) 2D PEA_2SnX_4 (X = Cl, Br, I) NPls. Reproduced with permission.[76] f) Schematic of 2D $(4Tm)_2SnI_4$ crystal structure. Reproduced with permission.[77] Copyright 2019, American Chemical Society.

2.2. Synthesis of Double Perovskite NCs

In the last few years, various DP materials featuring interesting optical properties have been synthesized at the nanoscale, comprising Cs_2AgBiX_6 (X = Cl, Br, I), $Cs_2AgInCl_6$, $Cs_2NaInCl_6$, $Cs_2NaBiCl_6$, and Cs_2AgSbX_6 NCs (X = Cl, Br).[2] Their broadband and largely Stokes-shifted luminescence, in particular, holds great potential for a variety of applications complementary to those of the narrow-band emitting LHP NCs, e.g., for single-component white LEDs, transparent luminescent solar concentrators, X-ray scintillators, remote thermometry and beyond.[85]

2.2.1. Synthesis

The stoichiometries of inorganic DP NCs comprise a minimum of three different metal cation species, which can be as high as six in the case of doped/alloyed systems (e.g., Bi-doped $Cs_2Ag_{1-x-y}Na_xK_yInCl_6$ NCs).[2,86] From an experimental standpoint, they require the use of flexible colloidal synthesis procedures. In this regard, the early approaches developed for the synthesis of LHP NCs, dating back to 2015, were based on the use of metal halide salts (e.g., PbX_2) as both the metal cation and halide precursors that were reacted with Cs-carboxylates. Such a synthesis scheme, however, was not easily extendable to quaternary or quinary NC compounds, just like the DPs.[30,87,88] Early reports on the synthesis of DP NCs appeared only in 2018, after Imran et al.[89] and Creutz et al. (**Figure 6**a).[90] developed new HI synthesis procedures that relied on benzoyl or silyl halides as halide precursors. In those approaches, the halide precursors were injected in a reaction mixture prepared by mixing the metal cation precursors (e.g., acetates, oxides, and carbonates) and surfactants at the desired temperature, triggering the formation of the NCs. It should be emphasized that side reactions, which could occur prior to the injection of the halide precursor (e.g., reduction of Ag^+ to Ag^0)[86], should be carefully monitored to achieve control over the quality of the final DP NCs. The halide composition of the DP NCs is easily tunable by treating them with respective silyl halides (Figure 6b). The DP NCs typically have a cubic shape with a high degree of monodispersity (Figure 6c). Later, it was shown that the DP NCs can be synthesized by injection of Cs-oleate into a metal and halide precursor mixture at high temperature,[91] similar to the HI synthesis of LHP NCs.

2.2.2. Compositional Engineering

Most of the quaternary DP systems feature a weak PL emission or even no PL emission owing either to an indirect band gap (Cs_2AgBiX_6, Cs_2AgSbX_6) or to a direct band gap

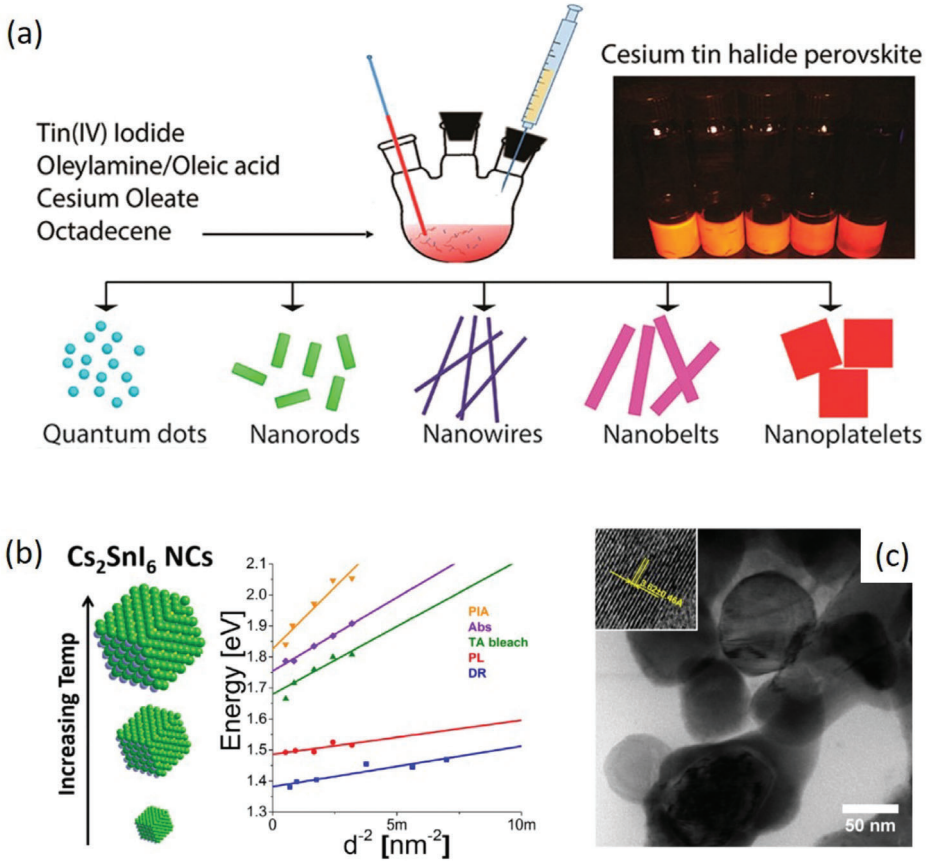

Figure 5. a) Schematic illustration for the controlled synthesis of perovskite Cs_2SnI_6 NCs of different shapes (left panel) and photograph of the as-prepared Cs_2SnI_6 samples under UV light (right panel). Reproduced with permission.[78] Copyright 2016, American Chemical Society. b,c) Scheme of ligand-free Cs_2SnI_6 NCs of different sizes and the effect of size on the band gap of the NCs (b), and the corresponding TEM image (c). Reproduced with permission.[79] Copyright 2017, American Chemical Society.

characterized by a parity-forbidden transition ($Cs_2AgInCl_6$) or by a parity-allowed transition with a weak oscillator strength (Cs_2NaInX_6 and Cs_2NaBiX_6).[17,92] Unsurprisingly, a variety of compositional engineering strategies have therefore been developed to enhance the PL of these DP compounds and ultimately disclose their full potential.[2]

Doping: The introduction of Bi^{3+} dopants in $Cs_2AgInCl_6$ NCs yields an orange PL emission with a PLQY of up to ≈11%,[93] further boosted to ≈26% by the introduction of Ce^{3+} as co-dopants.[94] Similarly, the use of Sb^{3+} dopants in $Cs_2NaInCl_6$ and Cs_2KInCl_6 NCs induces a bright PL emission, respectively in the blue and green regions, with QY values of ≈15–18%.[95] The broad and largely Stokes shifted PL emission of both Bi^{3+} doped and Sb^{3+} doped DP NCs is ascribed to the formation of self-trapped excitons (STEs) favored by the localization of the carriers—at the [$BiCl_6$] and [$SbCl_6$] octahedra, respectively—and by the softness of the DP lattice. The introduction of Mn^{2+} dopants in both $Cs_2AgBiCl_6$ and $Cs_2AgInCl_6$ NCs also gives rise to a broad orange PL emission with QY values as high as ≈16% attributed, in this case, to $^4T_1 \rightarrow {}^6A_1$ atomic-like d–d transitions at the Mn^{2+} centers (Figure 6d, e).[96,97] Interestingly, Sb^{3+}-Mn^{2+} co-doped $Cs_2NaInCl_6$ NCs exhibit a tunable dual-emission covering the white-light spectrum with the orange-red PL component likely originating from an energy transfer process between the STEs and Mn^{2+} dopants.[98] The use of lanthanide dopants (Ln^{3+}) in $Cs_2AgInCl_6$ or Cs_2AgBiX_6 (X = Cl, Br) NCs instead confers them a near-infrared PL emission (≈1000 nm with Yb^{3+}[96,99,100,101] and ≈1537 nm with Er^{3+}[99,101]) resulting from atomic-like f–f transitions characteristic of the Ln^{3+} centers.

Alloying: Alternative strategies to increase the PL emission of DP compounds involve the synthesis of quinary systems by employing a combination of B^I and B'^I ions (or B^{III} and B'^{III} ions). Provided that both $A_2B^IB^{III}X_6$ and $A_2B'^IB^{III}X_6$ (or $A_2B^IB^{III}X_6$ and $A_2B^IB'^{III}X_6$) DPs have the same crystal structure with small lattice parameters mismatch, allowing them to mix into solid solutions at any ratio, this approach is referred to as alloying. For instance, the use of both In^{3+} and Bi^{3+} ions leads to the formation of alloyed $Cs_2Ag(In_xBi_{1-x})Cl_6$ NCs, whose band gap can be tuned from indirect (x = 0, 0.25, 0.5) to direct (x = 0.75 and 0.9).[102,103] As a result, the intermediate $Cs_2Ag(In_{0.9}Bi_{0.1})Cl_6$ composition displays a dual-color PL emission reaching a QY of 36% in the violet region.[103] Similarly, the combination of Bi^{3+} and Sb^{3+} ions in alloyed $Cs_2Ag(Bi_xSb_{1-x})X_6$ (X = Cl, Br) also induces indirect-to-direct band gap transitions and boosts the intensity of their blue PL emission.[104,105] On the other hand, alloying of Na^+ and Ag^+ ions confers to $Cs_2(Ag_xNa_{1-x})BiCl_6$ NCs a largely Stokes-shifted PL emission centered in the red region with a maximum PLQY of ~3% attained for the $Cs_2(Ag_{0.05}Na_{0.95})BiCl_6$

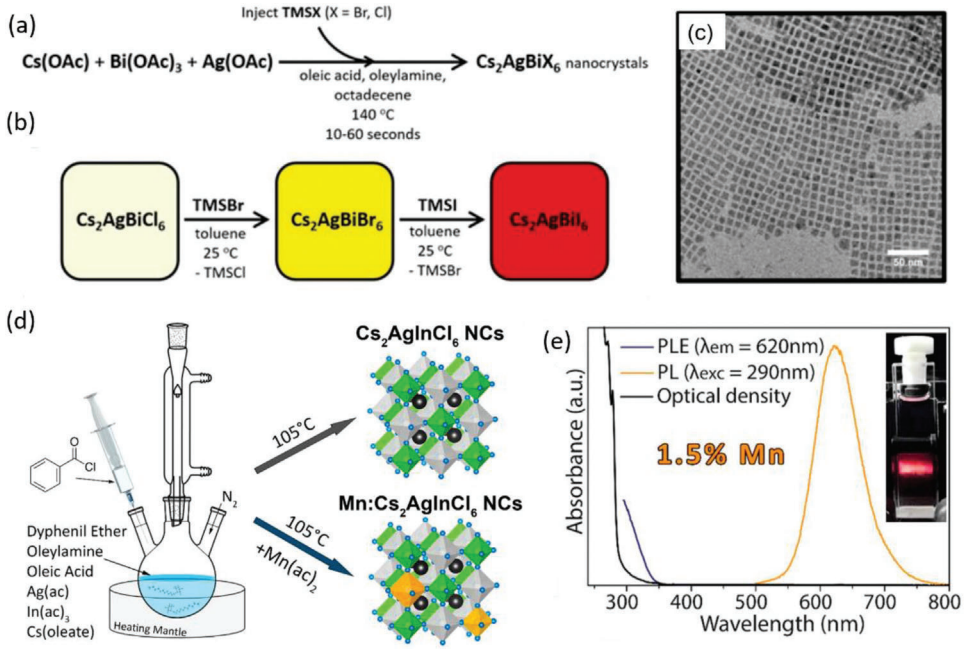

Figure 6. a,b) Synthesis of Cs_2AgBiX_6 NCs and halide composition tuning by adding TMSX (X = Br or I). c) TEM image of $Cs_2AgBiBr_6$ NCs. Reproduced with permission.[90] Copyright 2018, American Chemical Society. d) Schematic of hot-injection synthesis of $Cs_2AgInCl_6$ NCs and Mn^{2+}-doped $Cs_2AgInCl_6$ NCs. e) Absorption, PL, and excitation (PLE) spectra of 1.5% Mn^{2+}-doped $Cs_2AgInCl_6$ NCs. Reproduced with permission.[97] Copyright 2018, American Chemical Society.

composition.[106,107] In this case, the PL emission is ascribed to the radiative recombination of trapped excitons localized in spatially connected $BiCl_6$–$AgCl_6$ octahedra and favored by the beneficial shielding effect of the Na-rich DP matrix.

Doping and Alloying: In analogy with what has been observed in the bulk, the simultaneous doping and alloying of DP compounds represent the most valuable approach to boost their PLQYs at the nanoscale.[92,97,108] As a matter of fact, the introduction of Mn^{2+} dopants in alloyed $Cs_2Ag(In_xBi_{1-x})Cl_6$ NCs, while suppressing the STE emission from the DP matrix, promotes a pure Mn^{2+}-related orange PL emission with a PLQY as high as 44.6% for the $Cs_2Ag(In_{0.9}Bi_{0.1})Cl_6$ stoichiometry.[109] Interestingly, the use of Bi^{3+} dopants in alloyed $Cs_2(Ag_xNa_{1-x})InCl_6$ NCs also yields bright orange PL emission with PLQY values reaching 22% without the use of Mn^{2+} dopants.[110] Here, both the doping with Bi^{3+} ions and the alloying of Na^+ sites with Ag^+ ions are essential to achieve a PL emission, as the latter stems, again, from the radiative recombination of trapped excitons localized in proximal $BiCl_6$–$AgCl_6$ pairs of octahedra. Crucially, the introduction of small amounts of K^+ ions into Bi^{3+}-doped $Cs_2(Ag_xNa_{1-x})InCl_6$ NCs results in a more favorable inter-ligand packing (probably owing to a slight increase in the lattice parameters) therefore boosting the PLQY up to 67% with the $Cs_2(Ag_{0.20}Na_{0.73}K_{0.07})InCl_6$ stoichiometry.[86]

2.2.3. Dimensional Engineering

Another approach to tune the optical properties of DP NCs (and in general of semiconductor NCs) is to regulate their size in order to access quantum confinement effects (e.g., going from 3D to 2D and 0D systems).[2,41] However, the control over the dimensionality of DPs is relatively limited. In fact, for thin film DPs, the dimensionality is controllable from 3D and 2D using organic spacer molecules, and that enables switching from an indirect bandgap of $Cs_2AgBiBr_6$ into a direct one.[113] A few attempts have also been made to obtain DP NPls with control over thickness.[41,111,114] For example, Cs_2AgBiX_6 (X = Cl, Br, I) DP NPls with some control over their thickness have been synthesized by temperature-controlled hot-injection synthesis (Figures 7a-c).[111] However, the NPls exhibit absorption and PL features that are similar to those of bulk $Cs_2AgBiBr_6$ DPs (**Figure 7**b). The reaction yields monolayer NPls at room temperature, and they exhibit blue-shifted emission, likely due to direct bandgap exciton recombination.[111] However, the $Cs_2AgBiBr_6$ NPls were found to be weakly luminescent. Interestingly, the 2D $Cs_2AgIn_xBi_{1-x}Cl_6$ ($0 \le x \le 1$) DP NPls with a relatively high PLQY of 40% have been synthesized and their application to electrically driven LEDs was demonstrated (Figure 7d–f), though the EQE is only ≈0.01%, which is far lower than that of LHPs.[112]

2.2.4. Surface Engineering

Unfortunately, DP NCs often have much lower PLQYs compared to their bulk counterparts. This difference is commonly ascribed to an incomplete surface passivation of colloidal NCs after the synthesis and/or washing which leads to the presence of under-coordinated ions at their surface and can, in turn, result in the emergence of mid-gap electronic states.[115–117] In contrast to the "defect tolerant" LHP systems, DP systems are particularly prone to the formation of these so-called surface trap

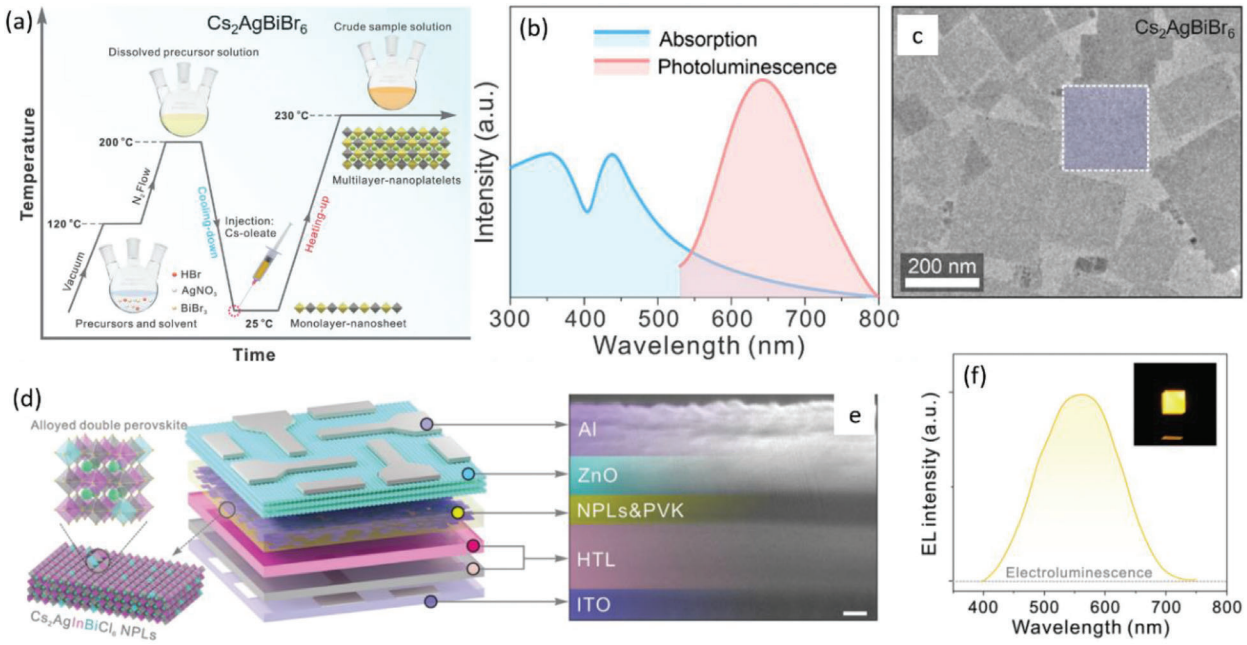

Figure 7. a) Schematic of the synthesis of $Cs_2AgBiBr_6$ DP NPls. (b,c) UV–vis absorption and PL spectra (b) and corresponding TEM image (c) of $Cs_2AgBiBr_6$ DP NPls. Reproduced with permission.[111] Copyright 2021, American Chemical Society. DP NPl LEDs: d) Schematic of device architecture of DP-NPl LEDs; e) cross-sectional scanning electron microscopy (SEM) image of the device; and f) electroluminescence (EL) spectra of the device. Reproduced with permission.[112] Copyright 2023, Wiley-VCH GmbH.

states.[118] For example, the lower PL QY values observed in Sb^{3+}-doped $Cs_2NaInCl_6$ and Cs_2KInCl_6 NCs (≈15–18%) compared to those of the bulk materials (≈90%) are attributed to an efficient hole trapping in mid-gap trap states that originates from the under-coordinated surface Cl sites. These traps compete with the emissive $SbCl_6$ centers for charge-carrier localization.[95] Similarly, the ultrafast component of the PL decay curves recorded in all $Cs_2(Ag_xNa_{1-x})BiCl_6$ NC samples, which renders a fraction of the NCs non-emissive or dark at cryogenic temperature, is consistent with the rapid dissociation of trapped charge-carriers (located at the $BiCl_6$–$AgCl_6$ centers) by non-radiative electron trapping at under-coordinated surface Bi sites.[101] Analogously, the ultrafast trapping of holes revealed in Bi^{3+}-doped $Cs_2(Ag_xNa_{1-x})InCl_6$ NCs is ascribed to mid-gap trap states originating from under-coordinated surface Cl sites, which prevent their localization at the emissive $BiCl_6$–$AgCl_6$ centers.[27]

To mitigate this issue and to narrow the gap between bulk and nano-sized DP materials in terms of PLQYs, a few surface engineering strategies have recently been explored. In particular, by systematically varying the hydrocarbon chain length of both alkylamines and carboxylic acids employed as surfactants in the synthesis of Bi^{3+}-doped $Cs_2(Ag_xNa_{1-x})InCl_6$ NCs, it is possible to raise the PLQY from 22% with the standard combination of oleylamine and oleic acid (see above) up to 37% with the optimal combination of decylamine and dodecanoic acid.[27] Interestingly, by employing $GeCl_4$ as the Cl precursor for the synthesis of Bi^{3+}-doped $Cs_2(Ag_xNa_{1-x})InCl_6$ NCs, the PLQY further rise up to 60%, most likely owing to the formation of NCs with Cl-rich surfaces, i.e., exhibiting a low density of under-coordinated Cl surface sites.[119]

2.2.5. Future Challenges and Outlooks

Overall, considering the huge array of potentially compatible B^I and B^{III} cations, only a few (complex) DP systems have been experimentally investigated to date, especially at the nanoscale. For instance, the combination of doping and alloying approaches, which gives optimal results in terms of PL efficiency, has been reported only in two cases. Moreover, co-doping approaches, involving two substituent ions, have not been yet fully exploited to achieve bright and tunable PL emission in DP NCs. Therefore, we believe that the development of increasingly sophisticated compositional engineering strategies will represent an interesting research direction in the field. A few reports demonstrated the potential of 2D DP NPls for photocatalytic and LEDs, but they haven't been explored as much as the 2D LHP NPls.

While our knowledge of the ligand shell of Pb-based perovskite NCs is reaching maturity, we know much less about the surface passivation of DP NCs, which seems to play a crucial role in the formation of detrimental surface trap states. In this context, ligand shell engineering via direct synthesis or post-synthesis ligand exchange would help to improve the PLQY of DP NCs and represent another important research direction. Alternative approaches to get rid of surface traps rely on the growth of a (thick) shell of a wider band gap material onto the (photo)active NC core. These have been vastly exploited in II–VI and IV–VI metal chalcogenides but not yet in DP NCs.

3. Optical Properties and Charge Carrier Dynamics

The optical properties of HPs are strongly dependent on the $[BX_6]^{4-}$ octahedral network. For instance, replacing Pb with Sn

Table 2. Comparison of ultrafast processes, mobility and diffusion length of charge-carriers in Pb-based versus Pb-free perovskites.

Perovskite Material	Cooling	Spin Relaxation	Trapping	Recombination	Mobility [$cm^2 V^{-1} s^{-1}$]	Diffusion length
$CsPbCl_3$ NCs	290 fs[139]		1.6 ns[139]	12.7 ns[139]	30[157–160]	
$CsPbBr_3$ NCs	310 – 390 fs[125,131]	1.9 – 3 ps[126,161]	45 ps[140]	2 ns[140]	4500[162]	9.2 μm[162]
$CsPbI_3$ NCs	560 – 580 fs[125,140,141]	6 – 32 ps (≈50K)[132,161], 3.2 ps[126]	215 ps[140]	>2 ns[140]	118[163]	1 – 1.5 μm[164]
$MAPbBr_3$ NCs	270[131]	6 ps[161]			57 – 97[165]	0.1 – 10 μm[166]
$MAPbI_3$ NCs	400 fs[142]	7 ps[167], 10 ps (77K)[161]		5.6 ns[142]	30 – 70[158–160]	0.1 – 10 μm[166]
$FAPbBr_3$ NCs	210 fs[131]				14[168,169]	6.25 μm[170]
2D-Layered Perovskites	200-700 fs[171]	7 ps[172]	15 ps[173]	>150 ps[173]	6 – 11[174]	<1 – 2.4 μm[170,175]
$Cs_2AgBiBr_6$ NCs	250 – 800 fs[132,135,176]		40 ps[176], 4.7 and 49 ps[135]	100 ns[176]	0.37[177]	0.11 – 0.23 μm[177,178]
$FASnI_3$ NCs	14.3 ps[69]				22[179]	
CsSnBr3 NCs		18 ps[149]				
CsMnBr3 NCs	50 ps and 400 ps[151]			605 ps[151]		
$Cs_3Bi_2I_9$	1 ps and 30 ps[156]			>3 ns[156]	4.6 – 6[180,181]	62 – 143 μm[180]

results in a decrease of their bandgap and thus leads to a red-shifted emission. In contrast, Bi-based DPs are very weakly emissive due to their indirect bandgap nature. Therefore, understanding the optical properties and hot-carrier dynamics is critical for the design of suitable materials for high-efficiency optoelectronic devices. In the last few decades, the charge carrier dynamics of various semiconductors have been significantly explored. For example, the extraction of hot carriers prior to their relaxation could help to overcome the Shockley–Queisser limit in a single junction solar cell.[120] The majority of the works on hot carrier dynamics in different semiconductors have been focused on relaxation, extraction, and multiplication,[121–123] and the early works on hot carrier dynamics of Pb-based chalcogenides[123] have been used as a basis for later studies on Pb-halide perovskites.[124] Halide-dependent hot carrier relaxation has been studied in Pb-halide perovskites via ultrafast TA and PL (e.g., streak camera imaging, up-conversion) techniques.[125,126] The hot carrier relaxation is often found to be phonon-mediated in LHPs, leading to the evolution of both small and large polarons.[127–130] Moreover, strong cation-dependent carrier relaxation has also been reported.[131] While significant advances have been made in understanding the charge carrier dynamics of LHPs, Pb-free perovskites are comparatively much less explored in this direction. This section briefly discusses the current understanding of the optical properties and charge carrier relaxation of THPs as well as DPs. **Table 2** summarizes the time scales for hot carrier cooling, spin relaxation, trapping, recombination, charge-carrier mobility, and diffusion length for Pb-free systems in comparison with LHPs.

Among all Pb-free perovskites, Bi-based Cs_2AgBiX_6 DP NCs (X = Cl, Br, I) have gained significant attention due to their chemical stability and interesting optoelectronic properties.[2,103,132,133,40] **Figure 8**a shows the absorption and PL spectra of a $Cs_2AgBiBr_6$ thin film at room temperature (295 K) and a cryogenic temperature (4 K).[134] The absorption spectrum at room temperature shows a strong peak at ≈2.8 eV, which becomes a little narrower at 4 K without any spectral shift. Besides, a large Stokes shift in the PL spectra is observed both at room temperature (295 K) and at cryogenic temperatures (4 K), without any appreciable difference in their PL maxima. Unlike Pb-perovskites, Bi-based DPs exhibit very weak PL, with a PLQY of less than 1%. Generally, the sharp and intense feature in the absorption spectrum of Cs_2AgBiX_6 DPs is attributed to bound excitons, while the broad and large Stokes-shifted PL has been assigned to self-trapped emission or phonon-assisted indirect bandgap emission (Figure 8b).[40,132,134,135] The strong exciton resonance in the absorption spectrum and large Stokes-shifted PL have significant consequences on the charge carrier dynamics, which will be discussed in the later part of this section. Similar to Pb-perovskites, the optical properties of $ASnX_3$ NCs are tunable by their halide composition as well as their dimensions. Figure 8c,d reports the absorption and PL spectra of $FASnI_3$ NCs grown at different reaction temperatures (from 25 to 125 °C) which correspond to a size range of 7.3 to 12. 1 nm.[69] A wide tunability of the optical spectra, from 650 to 750 nm, is clearly evident for this size range. The size of the NCs has an important consequence on their charge carrier dynamics, as revealed later on in this section.

To understand the marked differences in the optical properties of Cs_2AgBiX_6 DPs from those of Pb-based perovskites, the charge carrier dynamics of these materials have been investigated using several ultrafast optical spectroscopic techniques, such as TA, time-resolved PL imaging, and terahertz pump-probe.[2,40] For instance, Dey et al. studied the charge carrier dynamics of Cs_2AgBiX_6 NCs using ultrafast pump-probe and time-resolved PL spectroscopy. The high energy PL peak was attributed to direct band gap emission caused by the formation of a direct bound exciton, while the commonly observed low energy PL with a large Stokes shift was assigned to the indirect transition.[132] The time-resolved PL emission spectra acquired with above-bandgap excitation revealed that the PL spectra continuously redshifted from 430 nm in the first 10 ps and finally settled at 650 nm

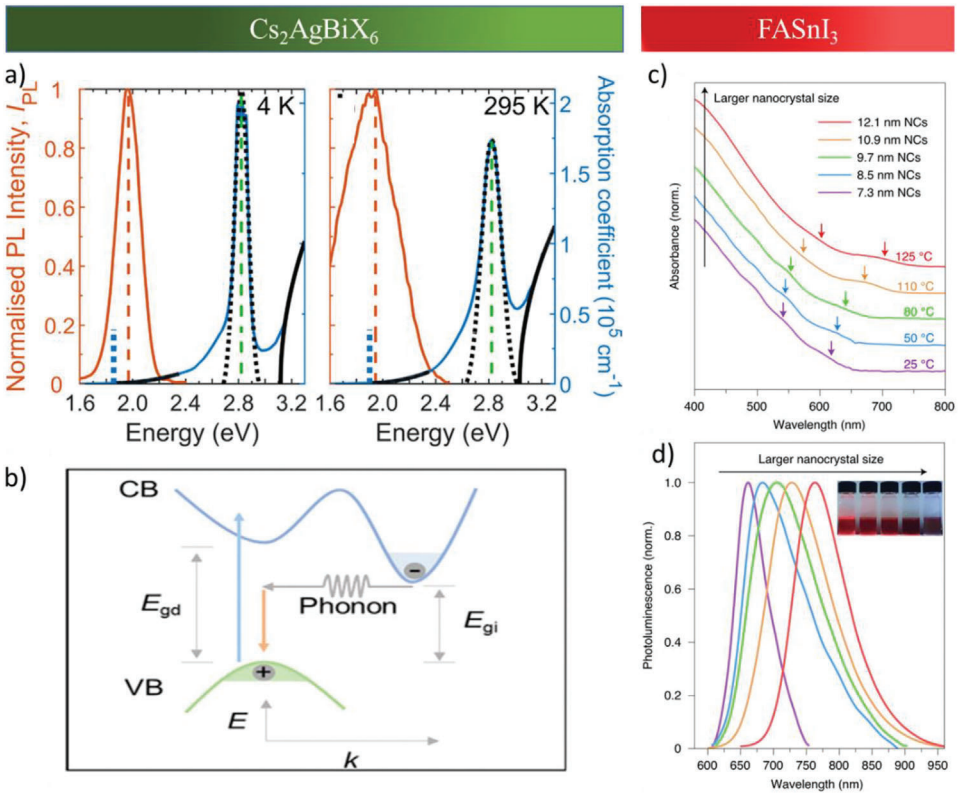

Figure 8. a) Steady-state absorption and PL spectra of a $Cs_2AgBiBr_6$ thin film at 4 K and 295 K. b) Schematic illustration of optical transitions in indirect bandgap $Cs_2AgBiBr_6$ semiconductor, and a typical phonon induced transition (Egd and Egi refers to direct and indirect bandgap, respectively). Steady State absorption (c) and PL (d) spectra of $FASnI_3$ NCs prepared at different growth temperatures, corresponding to NCs of different sizes. The inset of (d) is a photograph of the corresponding colloidal suspensions. Figures are reproduced with permission.[134] (a),[135] (b), and [69] (c,d). Copyright 2021, American Chemical Society, Reproduced under the terms of CC BY-NC 4.0.[135] Copyright 2021, The Authors, published by American Association for the Advancement of Science and Copyright 2021, Springer Nature.

(Figures 9a,b). The authors attributed the 1 eV redshift within the first 10 ps to the electron scattering from the X-point to the minimum of the conduction band, thus the direct bound exciton becomes indirect, as shown in **Figure 9**d. The faster PL decay (≈3 ps) at 450 nm is consistent with the large binding energy of the direct bound exciton (Figure 9b). In contrast, due to the transfer of direct to indirect bound exciton via electron intervalley scattering, the effective mass of the electron is reduced, leading to smaller exciton binding energy and slower PL decay at the red region of the spectrum (Figure 9b). Furthermore, femtosecond TA spectra in the first 3 ps evidence a low energy bleach at 430 nm due to the direct bound exciton as well as a high energy bleach due to higher lying energy states (Figure 9c). The bleach at 430 nm has a finite rise of ≈320 fs due to the hole-trapping process, inducing the formation of the bound exciton, while the higher energetic bleach has a pulse-width limited rise (Figure 9d).

As discussed previously, the optical properties of DPs are tunable by partially replacing Bi with In or by partially replacing Ag with Na. In this regard, Luo et al. demonstrated an increase in PLQY of $Cs_2AgInCl_6$ DPs by partly replacing Ag with Na.[92] The increase in PLQY is assigned to the reduction in the electronic dimensionality of the semiconductor by the breakdown of dark transition. Similarly, and as already mentioned, Yang et al. demonstrated the tunability of the indirect bandgap of DPs into direct bandgap by partially replacing Bi with In, by forming $Cs_2AgIn_xBi_{1-x}Cl_6$ DPs. Both the direct and indirect bandgap DP NCs were investigated by TA as well as DFT calculations (Figure 9e,f).[103] While the early time TA spectra of $Cs_2AgBiCl_6$ and $Cs_2AgIn_xBi_{1-x}Cl_6$ NCs are very similar, the later time spectra show an enhancement of the induced absorption signal in the below-bandgap region of In-alloyed DPs. In contrast, pure Bi-based DPs show bleaching at a longer time delay in the sub-bandgap states (>450 nm). Accordingly, the transition is referred to as indirect bandgap transition in the presence of high-density trap states. The presence of a strong induced absorption signal and the absence of sub-bandgap bleaching signal in In-incorporated DPs suggest a direct bandgap transition with negligible trap states.

A further detailed time-resolved investigation of $Cs_2AgBiBr_6$ DPs has been carried out by considering stronger self-trapping of free carriers through deformation potential caused by Fröhlich coupling.[135] By the combined study of transient reflection (TR), time-resolved terahertz spectroscopy (TRTS) (Figure 9g), and DFT calculations it was shown that ultrafast self-trapping in $Cs_2AgBiBr_6$ DPs causes the formation of highly localized polarons within a few picoseconds, leading to enhancement in

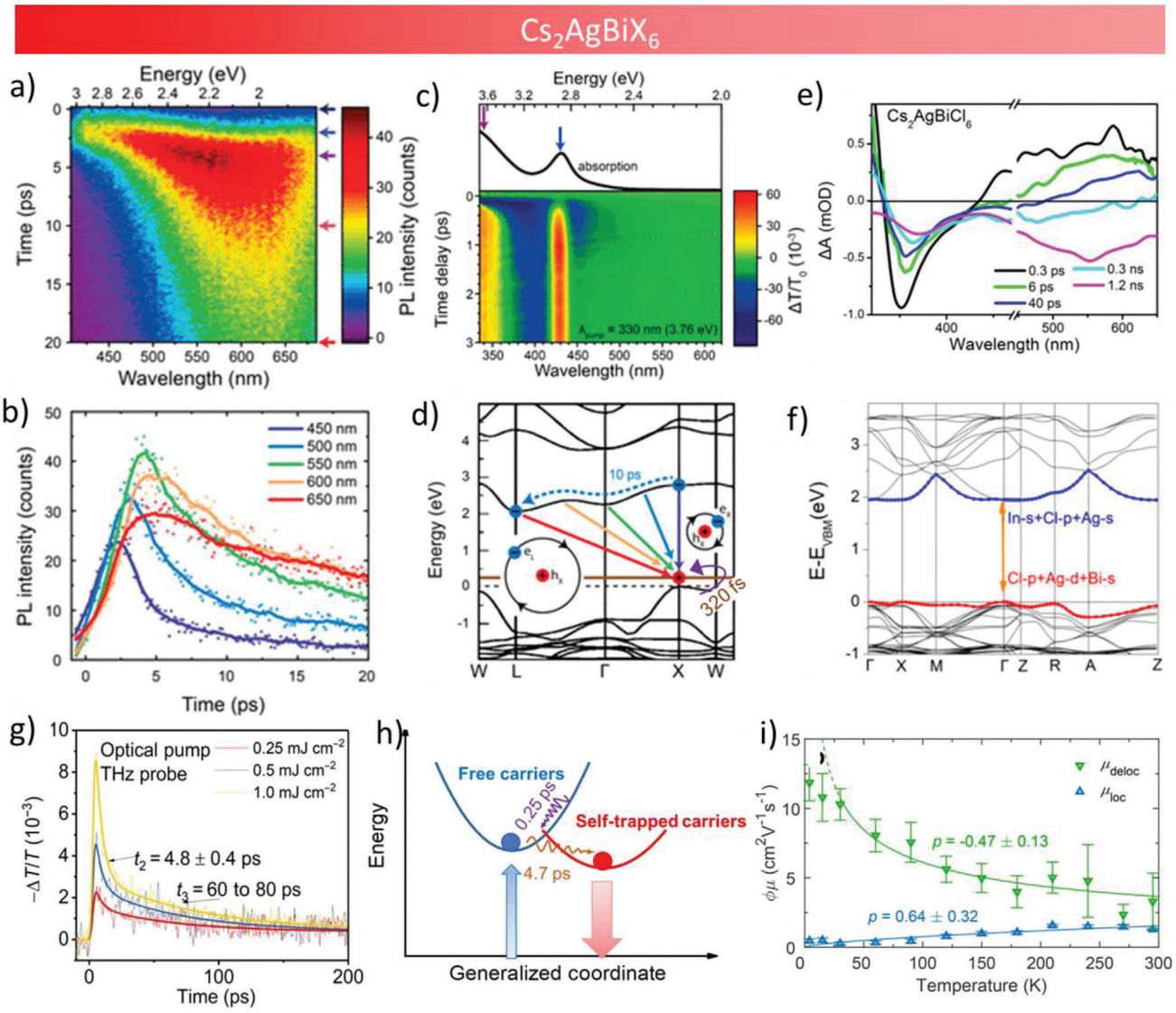

Figure 9. a) Time-resolved PL spectra of $Cs_2AgBiBr_6$ DP NCs, b) corresponding PL decay transients at different wavelengths upon 375 nm laser excitation, and c) TA spectra of the same sample upon 330 nm pump excitation (linear absorption spectrum is also shown on the top for comparison). d) Schematic illustration showing ultrafast hole trapping and electron intervalley scattering, thereby direct to indirect bound exciton formation in $Cs_2AgBiBr_6$ NCs. e) TA spectra $Cs_2AgIn_{0.75}Bi_{0.25}Cl_6$ at indicated time delays upon 320 nm pump excitation. f) Band structure of the $Cs_2AgIn_{0.75}Bi_{0.25}Cl_6$ showing direct bandgap character upon In incorporation. g) Terahertz transmission kinetics of $Cs_2AgBiBr_6$ polycrystalline sample under different pump fluences in time-resolved terahertz spectroscopy (TRTS) measurements. h) Generalized energetic schematic of DP for carrier self-trapping in ultrafast timescale. i) Temperature-dependent effective charge carrier mobilities for the delocalized (green) and localized (blue) states. Reproduced with permission.[132] (a–d),[103] (e,f),[135] (g,h), and r[134] (i). Copyright 2020 and 2018 American Chemical Society; Reproduced under the terms of CC BY-NC 4.0.[135] Copyright 2021, The Authors, published by American Association for the Advancement of Science.

the radiative recombination. The self-trapping in $Cs_2AgBiBr_6$ DPs with a decay time of ≈4.7 ps is in contrast to the typically observed subpicosecond Fröhlich polaron formation time in Pb-based perovskites. The observed sub-picosecond (0.25 ps) component of the direct exciton relaxation is consistent with the period of a typical longitudinal optical (LO)-phonon vibration. Therefore, the fast decay is attributed to the hot carrier relaxation via LO-phonons and the formation of a Fröhlich polaron. The slower component of the relaxation, which is an order of magnitude slower (4.7 ps), is translated to a phonon energy of ≈1 meV, typical for an acoustic phonon frequency. Therefore, the slow component is attributed to the electron–acoustic phonon coupling and ultrafast self-trapping of the carriers by the acoustic phonons (Figure 9h). These results are consistent with the TRTS measurements (Figure 9g), which probe the photoconductivity of the material and thus are insensitive to the charge-neutral exciton. This further supports the argument of carrier-phonon interaction, although due to the limited time-resolution (≈1 ps) the sub-picosecond electron-LO-phonon coupling can not be resolved in this case. Furthermore, the Herz group performed cryogenic THz photoconductivity measurements on several DPs to reveal strong carrier-lattice interaction, leading to

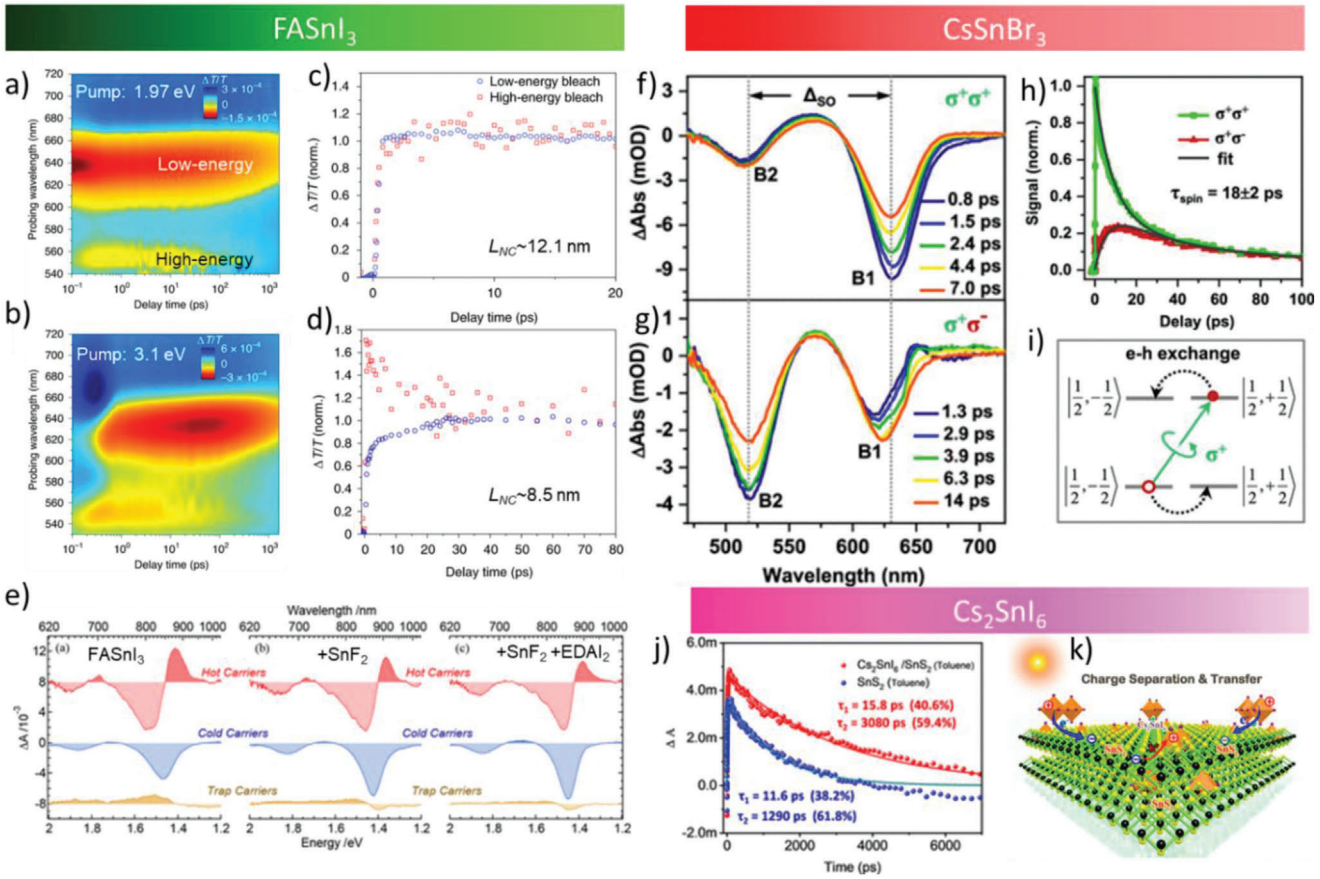

Figure 10. TA spectra of $FASnI_3$ NCs under a) 1.97 eV and b) 3.1 eV pump excitation. Low and high energy bleach transients for $FASnI_3$ NCs of sizes c) 12.1 nm and d) 8.5 nm under 3.1 eV excitation. e) Singular-value decomposition component spectra obtained from TA measurements of pure $FASnI_3$, $FASnI_3$ +SnF_2 and $FASnI_3$ +SnF_2 $EDAI_2$, respectively. TA spectra of $CsSnBr_3$ NCs with f) co- and g) counter-circular pump-probe polarization configurations ($\lambda_{pump} = 640$ nm). h) Normalized TA kinetics of the low energy bleach (640 nm, B1) with co- (green) and counter- (red) circular polarization condition, and their simultaneous exponential fit with 18 ps spin-relaxation time. i) Schematic illustration for the electron-hole exchange induced spin-relaxation process. j) TA kinetic traces of Cs_2SnI_6 and Cs_2SnI_6/SnS_2 at the broad positive absorption (PA) feature (540 nm) upon 375 nm pump excitation. k) Schematic for the charge separation and transfer in Cs_2SnI_6/SnS_2 heterostructure. Reproduced with permission.[69] (a–d),[148] (e),[149] (f–i),[150] (j,k). Copyright 2021, Springer Nature; Copyright 2020, 2021 and 2019, American Chemical Society.

the formation of polarons.[133,134] By fitting the early time transients in the optical pump terahertz probe experiments, they were able to access the charge-carrier mobility before and after their localization with a simple two-level model in both $Cs_2AgBiBr_6$ and Cu_2AgBiI_6. A rapid decay in the transient at a cryogenic temperature reveals that the mobility of the initial delocalized state, e.g., in $Cs_2AgBiBr_6$, is much higher (≈12 $cm^2\ V^{-1}\ s^{-1}$) than the final localized state (≈0.5 $cm^2\ V^{-1}\ s^{-1}$).[134] In contrast, the high-temperature transients do not show any rapid decay, indicating the charge-carrier mobility of the localized state (≈1.3 $cm^2\ V^{-1}\ s^{-1}$) approaching the value of the initial delocalized state (≈3 $cm^2\ V^{-1}\ s^{-1}$). Indeed, the charge-carrier mobility shows a negative exponent for the initial delocalized state suggesting bandlike transport, while a positive exponent was observed for the localized state, indicating temperature-dependent charge hopping in the localized, self-trapped states (Figure 9i). Interestingly, the localization rate is found to be temperature-indepndent. The values of the charge-carrier mobility at the localized state and the localization rate were further used to estimate the charge-carrier diffusion length which was found to be ≈400 nm.[133] This value is in good agreement with typical Pb-based perovskites,[136,137] suggesting that $Cs_2AgBiBr_6$ is promising for optoelectronic applications.

The other important class of LHPs are $ASnX_3$ systems (both thin films and NCs), which are extremely challenging to obtain in stable form as they suffer from poor stability due to the oxidation of Sn^{2+} to Sn^{4+}(see Section 6). Yet, there are few reports on the optical properties and charge carrier dynamics in these perovskites that show promising opportunities for optoelectronic applications. For instance, Dai et al. recently performed a systematic work on the size-dependent carrier cooling dynamics of $FASnI_3$ NCs via TA spectroscopy upon excitation at near bandgap (630 nm) as well as above bandgap (400 nm) (Figures 10a, b).[69] The TA spectra show two bleaching features, one at the band edge and the other at ≈0.3 eV higher than the band edge, and are consistent with the absorption spectra. The appearance of the higher energy bleach upon band-edge excitation can be ascribed to the depopulation of the ground state only (**Figure 10**a), as the second excited state is not populated under

this condition. A similar result was observed in smaller-size LHP QDs.[138] However, upon above bandgap excitation (400 nm), the higher energy bleach evolves much faster than the lower energy bleach (Figure 10b). This has been studied via probing the two bleach transients for different size $FASnI_3$ NCs (Figures 10c, d). For large-size NCs (12 nm), a sub-picosecond buildup of the low-energy bleach corresponding to rapid carrier cooling (<1 ps) from higher energy states was observed, and is similar to Pb-halide perovskites.[125,129,131,139–142] In contrast, for smaller NCs with strong quantum confinement, an extremely slow evolution (≈15 ps) of the low-energy bleach was observed with a concomitant decay of the high-energy bleach. This indicates the slower carrier cooling from the higher energy state to the lower energy state is due to direct relaxation to the band edge state. This slow carrier cooling was reported to be a unique observation in strongly confined Pb-free perovskites due to phonon bottleneck effect, which is around one to two orders slower than Pb-based perovskites (Table 2). Moreover, this slow cooling is an order of magnitude slower than typical II-VI and IV-VI NCs,[143–145] although properly engineered II-VI alloyed or core–shell NCs show comparable (≈8 ps)[146,147] or even slower (≈1 ns)[122] carrier cooling dynamics. Besides, Narra et al. studied the effect of additives SnF_2 and ethylenediammonium diiodide ($EDAI_2$) on the charge carrier dynamics of $FASnI_3$.[148] The singular-value decomposition analysis of the TA data reveals a significant reduction of the trap states upon the addition of SnF_2 or $EDAI_2$ (Figure 10e). In addition, the shallow- and deep-trap mediated charge recombination proceeds extremely slowly upon the addition of these additives, typically 5–10 times slower as compared to that of pristine $FASnI_3$.

The spin-relaxation of Sn-perovskites was found to be longer as compared to that of Pb-counterparts, and the trend is similar to their PL lifetimes. For instance, Liang et al. studied the spin-relaxation dynamics of $CsSnBr_3$ NCs in which the spin-orbit coupling is much weaker than LHPs.[149] This provides an opportunity to have a larger spin-relaxation lifetime and therefore may have a useful application in spintronic. Figure 10f,g shows the transient absorption spectra (640 nm excitation) of $CsSnBr_3$ at co- and counter-circular pump/probe polarization configurations. The bleach signal at the band edge position (640 nm, labeled as B1) is due to the state-filling effect of electron and hole, while the bleach signal at higher energy (520 nm, labeled as B2) is due to the state-filling effect of the hole only. This is because the higher energy transition (causing the appearance of B2) cannot be populated by the pump pulse excitation, which is similar to the earlier discussion on $FASnI_3$[69] and $CsPbBr_3$.[138] Figure 10h compares the B1 transients for co- and counter-circular polarization condition, along with their simultaneous fit that yields a spin-relaxation time of 18 ps. The concerted mechanism of spin-relaxation process via electron–hole exchange is depicted in Figure 10i. The reported spin-relaxation time for $CsSnBr_3$ NCs is the longest at room temperature as compared to that of Pb-halide perovskites (see Table 2). Besides, the charge carrier relaxation in Sn-based perovskites can be modified/controlled by combining them with other materials or vice versa. For example, Wang et al. fabricated a heterojunction consisting of lead-free Cs_2SnI_6 perovskite NC/SnS_2 nanosheet hybrid that leads to prolonged charge separation as compared to a SnS_2 nanosheet alone (Figures 10j,k).[150] The spatial charge separation boosts the photocatalytic CO_2 reduction by a few folds compared to the SnS_2 nanosheet.

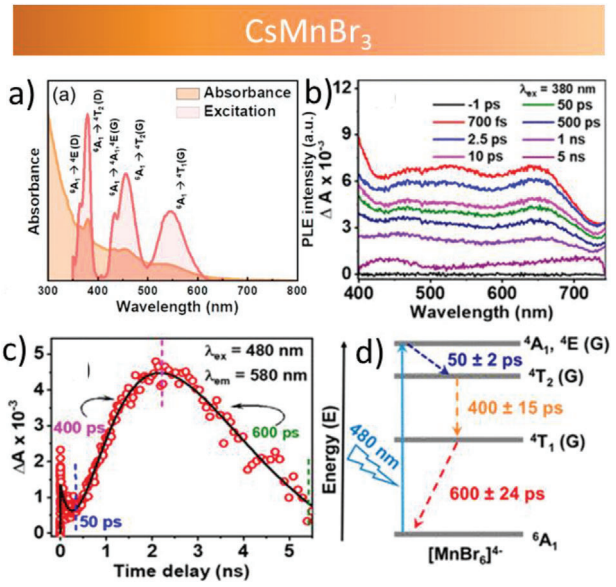

Figure 11. a) PLE and absorption spectra of $CsMnBr_3$ NCs with assigned d-d transitions of Mn^{2+}, b) TA spectra of $CsMnBr_3$ NCs upon 380 nm pump excitation and c) the corresponding transient kinetics at 580 nm (λ_{pump} = 480 nm). d) Schematic depiction of charge carrier relaxation pathways from excited state to ground state of Mn^{2+}. Reproduced with permission.[151] (a–d). Copyright 2021, American Chemical Society.

Besides Sn, there are some reports demonstrating the replacement of Pb with Mn to obtain $CsMnX_3$ NCs. The charge carrier relaxation properties of these materials were also investigated.[151–153] Unlike the Pb and Sn-based perovskite systems, the emission from $CsMnX_3$ stems from the octahedrally coordinated Mn^{2+} complex. The optical absorption and PLE spectra of $CsMnBr_3$ NCs show several resonances (**Figure 11**a), corresponding to the d–d transitions present in the octahedrally coordinated Mn^{2+}. The PL decay in this system is strongly dependent on the excitation of a particular d–d transition of the absorption feature. Therefore, pump wavelength-dependent TA spectroscopy was performed to understand the decay dynamics. Figure 11b shows the TA spectra of $CsMnBr_3$ NCs upon 380 nm excitation that shows a monotonous decay within a few ns timescale. The decay trace at 580 nm upon 480 nm pump shows interesting photophysics, where initially a fast decay was observed within 50 ps, followed by a rise of 400 ps (Figure 11c). The delay in populating the low-lying excited state of Mn is about 400 ps before returning to the ground state in another 600 ps (Figure 11c). The proposed charge carrier relaxation mechanism is illustrated in Figure 11d. Interestingly, the 400 ps time constant for populating the low-lying states (i.e., cooling to Mn state) matches well with an earlier report on Mn-doped CdTeSe alloyed NCs where 700 ps timescale was observed and attributed to a similar phenomenon.[154] In addition, ultrafast charge carrier dynamic studies were also performed

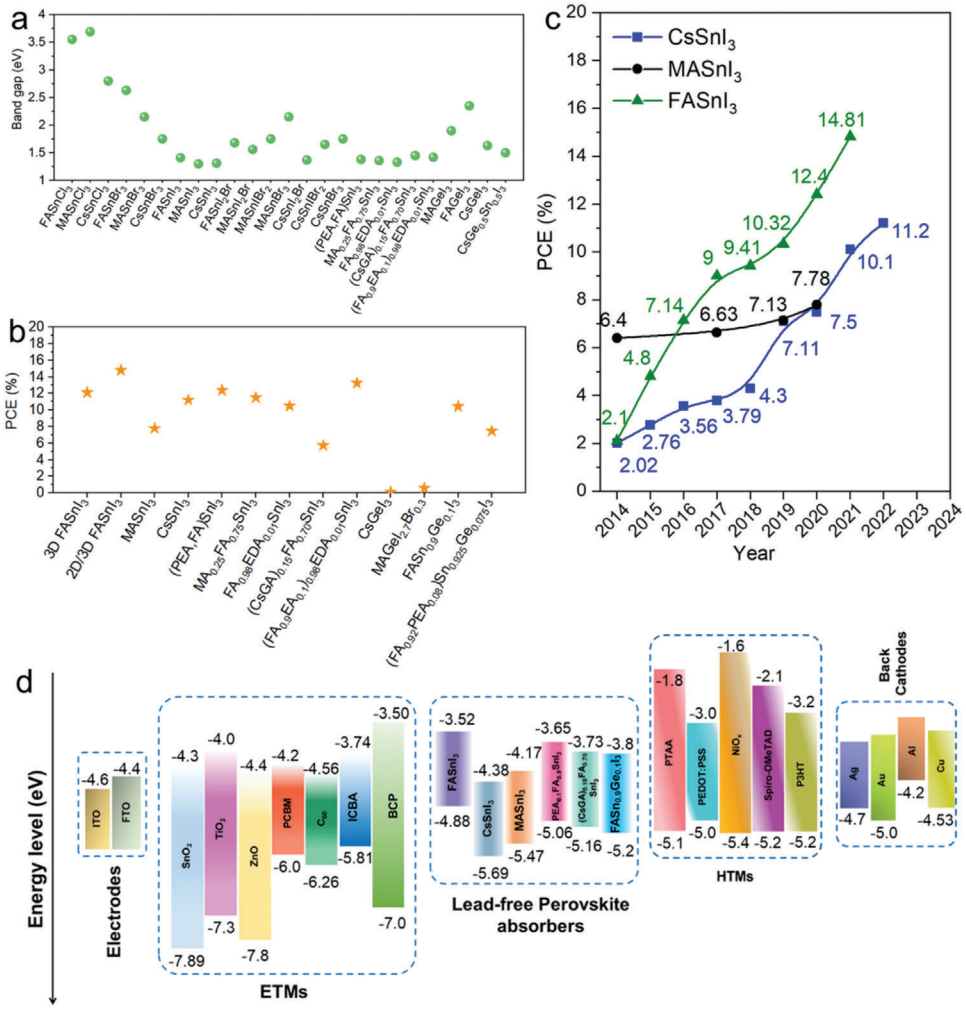

Figure 12. a) Optical bandgaps of Sn- and Ge-based perovskites. b) Record efficiencies of representative Sn- and Ge-based perovskite solar cells. c) PCE trend of Sn-based perovskite solar cells.[189–200,59] The bandgap and PCE data are obtained from references.[201–204] Schematic representation of the energy band diagram of different Sn- and Sn/Ge-based perovskite absorbers in comparison with energy levels of different electrodes, HTMs, ETMs, and back electrodes. d) The data are collected from references[199,201,205] and the figure is adapted with permission.[201] Copyright 2022, Wiley-VCH.

on Pb-free non-perovskite materials, e.g., $Cs_3Bi_2I_9$ single crystal where strong carrier-phonon coupling could lead to polaron formation.[155,156]

4. Optoelectronic Devices

4.1. Solar Cells

4.1.1. Sn- and Ge-Based Perovskite Solar Cells

Current Status: Halide perovskite solar cells (PSCs) have gained enormous attention in scientific research and the photovoltaics industry, owing to their outstanding optoelectronic properties and low-cost production. For LHPs, a record PCE of 26% for single-junction PSCs has been achieved,[2] which is comparable to that of single-junction c-Si solar cells (26.8%).[182] Furthermore, the unencapsulated PSC devices maintained ≈90% of their initial efficiency after continuous light exposure for 500 h.[2] However, the use of toxic Pb may slow down the pace of scale-up for commercialization. As discussed in previous sections, various lower-toxicity compounds have been investigated to replace LHPs, such as Sn/Ge-based halides with perovskite structure, some DPs, and Bi/Sb-based halides with perovskite-like structure.[183–186,2,52] Among these candidates, ABX_3 (B = Sn, Ge) Pb-free perovskites are the most similar to $APbX_3$ in terms of structure and properties and have theoretical efficiencies exceeding 20% under 1-sun illumination.[187,188]

Among the ABX_3 (B = Sn, Ge) perovskites shown in **Figure 12**a, $ASnI_3$ (A = Cs, FA, MA) perovskites have direct bandgaps in the range of 1.2–1.4 eV, which have great potential to achieve a high efficiency close to the Shockley-Queisser (SQ) limit (≈33%). However, the record PCE for Sn-based perovskite solar cells has only reached 14.81%,[206] which is far behind the theoretical value as well as the PCEs achieved for LHP solar cells. The main issues are: 1) $ASnI_3$ perovskites suffer from serious oxidation, resulting in high background carrier density and high defect density; 2) they exhibit poor film quality because of their rapid crystallization; 3) non-radiative recombination leads to a

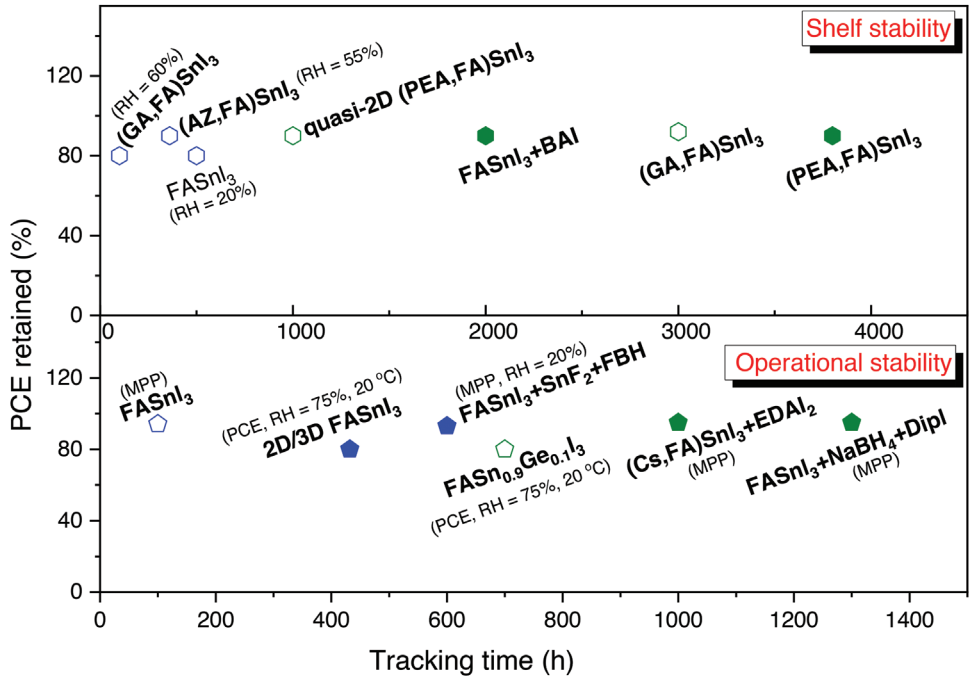

Figure 13. Shelf stability and operational stability of representative Sn- and Sn/Ge-based LFP solar cells under different conditions, i.e., encapsulated (color filled), unencapsulated (unfilled), ambient air (blue), N_2 (green), MPP and relative humidity (RH). The data are extracted from refs. [201,202,213].

low open-circuit voltage and fill factor;[204] 4) there is inefficient charge-carrier extraction due to poor energy level alignment with charge transport layers. In order to improve efficiency and stability, various engineering approaches have been applied in the last decade, including composition modification (A-site cations and halides), structure dimension tuning by constructing quasi-2D structure or 2D/3D heterostructure, solvent engineering, interfacial engineering via surface/grain boundary passivation using additives, and device architecture engineering.[2,202,204,207–210]

Generally, Sn-based perovskites are very sensitive to ambient conditions that directly affect the efficiency of PSCs and their long-term stability. Composition engineering is one of the most effective approaches to tailor the optoelectronic properties of Sn-based perovskites. The optical bandgap (1.2–3.55 eV), lattice stability, and crystallinity of lead-free perovskites can be tuned by modifying the chemical composition of A- or X-site atoms in accordance with Goldschmidt tolerance factor.[203,211,212] $FASnI_3$ PSCs have shown faster progress in efficiency and stability than $CsSnI_3$ and $MASnI_3$ PSCs (Figures 12b,c). On the other hand, $AGeI_3$ perovskites have wider optical bandgaps (1.6–1.9 eV) and are even less stable than $ASnI_3$.[204]

A-site cation engineering has been proven to be an effective way to enhance the efficiency and stability of Sn-based perovskites.[213] Some additives, such as Sn halides, reducing agents (Sn powder, hydrazine (N_2H_4) compounds, and gallic acid) and large organic cations, have also been used to enhance the stability.[186,214] It has been found that SnF_2 can facilitate the formation of dense and compact films with large grains, and is extensively used as an additive for Sn-based PSCs.[202] Large organic cations, like phenethylammonium (PEA), butylammonium (BA), and its derivatives can facilitate the formation of a quasi-2D or 2D/3D heterostructure to minimize the efficiency loss by impeding degradation from outside to the perovskite grains.[213] Especially PEA has been the most popular organic cation to fabricate 2D/3D Sn-based PSCs, because it can induce the perpendicular growth of the perovskite domain. In this regard, He et al.[215] achieved the highest PCE of 14.81% for Sn-based PSCs in 2021 by using 4-fluoro-phenethylammonium bromide (FPEABr) as an additive in the perovskite films. Some other organic additives such as ethylenediammonium diiodide ($EDAI_2$), guanidinium ($CH_6N_3^+$, GA), and azetidinium (AZ) were used to enhance the quality and orientation of 2D/3D perovskite films.[213,216]

Regarding Ge-based perovskites, the most interesting ones are the Ge-Sn alloyed HP, which have better stability and narrower bandgaps than pure Ge-based perovskites. The efficiency of pure Ge-based PSCs is lower than 1%.[204] On the other hand, a PCE of 10.43% for $FASn_{0.9}Ge_{0.1}I_3$ PSC[199] and a PCE of 13.24% for $Ge_{0.01}(FA0_{.9}EA_{0.1})_{0.98}EDA_{0.01}SnI_3$ PSCs have been achieved.[197] The partial substitution of the formamidinium cation with the ethylammonium (EA) cation results in more stable THP crystals with suppressed trap density. Furthermore, the more favorable energy levels of the EA-substituted Sn-based perovskites enhance the charge extraction into the charge transport layers and thus reduce the charge carrier recombination (Figure 12d).[197]

Stability is still one of the major concerns for Sn-based PSCs. Shelf-life and operational stability of representative Sn- and Sn/Ge-based LFP solar cells under different conditions are summarized in **Figure 13**. Regarding the device architecture of Sn-based PSCs, the p-i-n structure has better stability than the n-i-p structure. In the n-i-p structure, some metal oxides acting as electron transport materials (ETMs) can accelerate the oxidation of Sn^{2+}, and the energy-level mismatch between the charge transport layer and perovskite limits favorable charge extraction, as shown in Figure 12d. The record PCE of Sn-based PSCs with

p-i-n architecture (14.81%) is superior to that with n-i-p architecture (9.06%).[185] In the p–i–n architecture, PEDOT:PSS and fullerene derivatives (C60, PCBM, and ICBA) are generally used as hole transport materials (HTMs) and ETMs, respectively. The (PEA, FA)SnI_3 PSCs with a high PCE of 12.4%, NH_4SCN as an additive, and ICBA as ETM show excellent shelf stability by maintaining 90% of the initial efficiency for over 3800 h.[193] The $FASnI_3$ PSCs with a p-i-n device architecture (PCE ≈ 10.61%) remained unchanged upon 5 h in air (60% RH) at maximum-power point (MPP) and 96% of the initial PCE was kept after 1300 h at MPP in N_2, by incorporating Dipropylammonium iodide (DipI) together with a well-known reducing agent, sodium borohydride ($NaBH_4$).[217] These are the highest reported values of operational stability for Sn-based solar cells.

Outstanding Challenges: Additives play a key role in affecting the efficiency and stability of Sn-based and Ge-based perovskite solar cells. Although researchers have explored many types of additives, there is a lack of systematic research on the structure-property-performance relationship, which is necessary to get a better understanding of the underlying mechanisms. To optimize the performance of Sn-based solar cells toward commercialization, complementary characterization techniques to understand the mechanism of additives on crystal structure, defect passivation, and optimizing carrier transport in the perovskites are needed. Further discovery of efficient additives that passivate the surface and prevent the oxidation of Sn^{2+} is necessary. The main challenges affecting the stability of the Sn-based PSCs are the oxidation of Sn^{2+} and degradation upon exposure to moisture, illumination, and (high) temperature. Nevertheless, precise control over the crystallization of Sn-based thin films and fine interfacial contact between different layers of the devices are essential to achieve high-performance PSCs. In addition, efficient encapsulation strategies are required to enhance the long-term stability of PSCs.

Future Prospects: Sn-based perovskites are the most promising lead-free ones for lead-free PSC applications despite the record PCE is still far behind that of the Pb-based analogs, which limits its potential commercial deployment. The current optimization of Sn-based thin films and PSCs is mostly done via a trial-and-error experimental approach, which is very time-consuming and inefficient. Combining high-throughput computation and machine learning to accelerate the discovery of various functional additives, Sn-based absorbers, and charge transport materials for potential solar cell applications is one desirable direction. Developing in-situ characterization techniques to observe microstructures, and investigate crystallization dynamic, defects, and charge transport properties is highly demanded. It is also of great interest to develop highly efficient and stable Sn-based PSCs with novel functions like semitransparent and flexible devices to integrate with buildings, wearable electronics, and the Internet of Things.

4.1.2. Double Perovskite-Based Solar Cells

Double perovskites (DPs), with the general formula $A_2B^IB^{III}X_6$ or $A_2B^{IV}X_6$ (vacancy-ordered), have emerged as promising alternatives to LHPs owing to their higher stability over Sn- and Ge-based perovskites.[17,218–223,52] DPs have been preferred for solar cells due to their three-dimensional crystal structure and long carrier lifetimes (≈660 ns).[224] DPs consist of A-site monovalent cations (Cs^+ or MA^+), B^I-site monovalent metal cations (e.g., Li, Na, Ag, or Au), B^{III}-site trivalent metal cations (e.g., Bi, Sb, In, Fe, Tl, or Au), and halide anions (**Figure 14**). As discussed in the previous sections, the combinations of different A, B^I, B^{III}, and X^- ions results in a library of a large number of DPs with tunability over bandgap and stability. Among all, Bi-based DPs, especially Cs_2AgBiX_6 (X = Br or Cl), have been significantly exploited because Bi^{3+} possesses the $6s^26p^0$ electronic configuration similar to Pb^{2+}.[224–228] In 2016, Slavney et al. reported the synthesis of $Cs_2AgBiBr_6$ with an indirect bandgap of 1.95 eV, a long PL lifetime of ca. 660 ns, and significant stability against light and humidity.[224] More in-depth discussion on the optical and electronic structure of DPs is found in the previous sections. Since 2016, $Cs_2AgBiBr_6$ has been greatly investigated for solar cells because its properties are considered promising for photovoltaics. The other Bi-based DPs explored for solar cells are $Cs_2LiBiCl_6$ (2.597-3.15 eV),[229] $Cs_2NaBiCl_6$ (2.9-3.72 eV),[230] Cs_2NaBiI_6 (1.66 eV),[231] $(CH_3NH_3)_2AgBiBr_6$ (2.02 eV),[232] and $(CH_3NH_3)_2TlBiBr_6$ (2.06 eV).[233] Sb-based DPs such as Cs_2SbBiX_6 (X = Cl[234,235] or Br[228,236]) have also been investigated and it was found that the indirect band gaps are contributed by Sb-5s/Ag-4d (valence band maximum) and Sb-5p orbitals (conduction band minimum).[236] However, the reported PCEs of these materials are far behind those of LHPs, suggesting that they are relatively less promising for solar cells because of their indirect bandgap and worse absorption of the solar spectrum.

In addition, In-,[237–240] Fe-,[241,242] Tl-,[243] and Au-based direct bandgap DPs[244–247] have been synthesized, and they have lower band gaps than the Bi and Sb- based DPs. However, there are very few reports on the exploration of these DP systems for solar cells. On the other hand, vacancy-ordered DPs ($A_2B^{IV}X_6$) have been promising candidates for solar cells, and they exhibit an antifluorite crystal structure with isolated BX_6 octahedra bridged by A-site cations.[254] Among all, Cs_2SnI_6 is one of the most investigated vacancy-ordered DPs for solar cells. Cs_2SnI_6 is stable in air as it results from the degradation and reconstruction of $CsSnI_3$ through the reaction $CsSnI_3 \rightarrow CsI + SnI_2 \rightarrow CsI + SnI_4 \rightarrow Cs_2SnI_6$.[255] Dye-sensitized solar cells fabricated using Cs_2SnI_6 as a hole transport layer (HTL) have recorded a PCE of 7.8%.[256] This has motivated the community to explore vacancy-ordered DPs such as Cs_2SnI_6[248–252] and Cs_2TiBr_6[253] as active layers. Figure 14 summarizes the bandgap values of different DPs synthesized experimentally. It is noted that the broad distribution of bandgaps for DPs is due to the differences in size, synthesis methods, and calculation models. Despite the existence of many DPs with suitable direct bandgaps for solar cells, $Cs_2AgBiBr_6$ has been the most promising and exploited system to date.

The device architecture of DP-based solar cells generally consists of substrate/transparent electrode/ ETL/DP/HTL/electrode. A tin-doped indium oxide (ITO) or fluorine-doped tin oxide (FTO) film coated on glass is used as the transparent electrode (cathode). The typical ETL materials are compacted TiO_2 (c-TiO_2), mesoporous TiO_2 (m-TiO_2), or SnO_2. The HTL materials are 2,2,'7,7′-tetrakis-(*N*,*N*-di-4-methoxyphenylamino)−9,9′-spirobifuorene (spiro-OMeTAD), poly(3-hexylthiophene) (P3HT), and poly[bis(4-phenyl)(2,4,6-trimethylphenyl)-amine] (PTAA). The

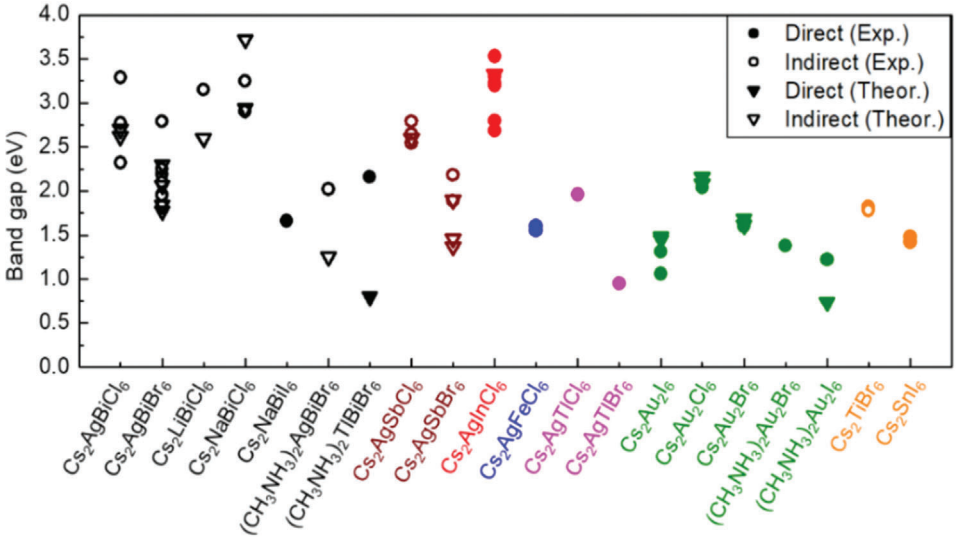

Figure 14. Bandgap values of DPs and vacancy-ordered DPs (orange). The values are obtained from refs. [229,231,224–233,235–251].

typical anode layers are Au, Ag, or Cu. Although various DPs have been predicted and synthesized, $Cs_2AgBiBr_6$-based solar cells have been the most investigated ones. Although the synthesis of $Cs_2AgBiBr_6$-bulk crystals was already reported in 2016,[224] the solubility of $Cs_2AgBiBr_6$ is too low in standard solvents to prepare the film for solar cells. Bein et al. first reported $Cs_2AgBiBr_6$-based solar cells in 2017.[257] They applied dimethyl sulfoxide as the solvent for spin-coating (**Figure 15**a). Then, the sample was heated twice during film preparation for preheating and annealing. Figure 15b,c shows the PCE as a function of preheating and annealing temperatures, respectively. Preheating a precursor solution at a suitable temperature (75 °C) improves the film quality and surface coverage. Annealing the coated film at a higher temperature than 250 °C is required for the formation of phase-pure $Cs_2AgBiBr_6$. Thus, the first $Cs_2AgBiBr_6$-based solar cell exhibited a PCE of 2.43% with V_{OC} of 0.98 V, J_{OC} of 3.93 mA cm^{-2}, and FF of 69% (Figure 15d), and showed significant stability under ambient conditions for 25 days. After Bein's report, various $Cs_2AgBiBr_6$ film deposition methods have been proposed, such as low-pressure-assisted spin-coating (PCE of 1.32%),[258] sequential evaporation (PCE of 1.03%),[259] sequential vapor deposition (PCE of 1.52%),[260] precursor engineering using an additive (PCE of 0.73%),[261] and spray coating (PCE of 2.3%).[262] The reason for the use of different methods is to optimize the quality of DP films in terms of crystallinity, grain size, thickness, phase purity, and crystal orientation to improve the PCE of solar cells. However, the PCE of DPs is significantly lower than that of LHPs.

Inverted planar heterojunction solar cells were also fabricated, but their PCEs were even lower (2.23%).[263] Since 2020, the PCE performance of $Cs_2AgBiBr_6$-based solar cells has been effectively improved by bandgap modifications through photosensitizing dyes or MXenes.[264–267] For instance, Yang

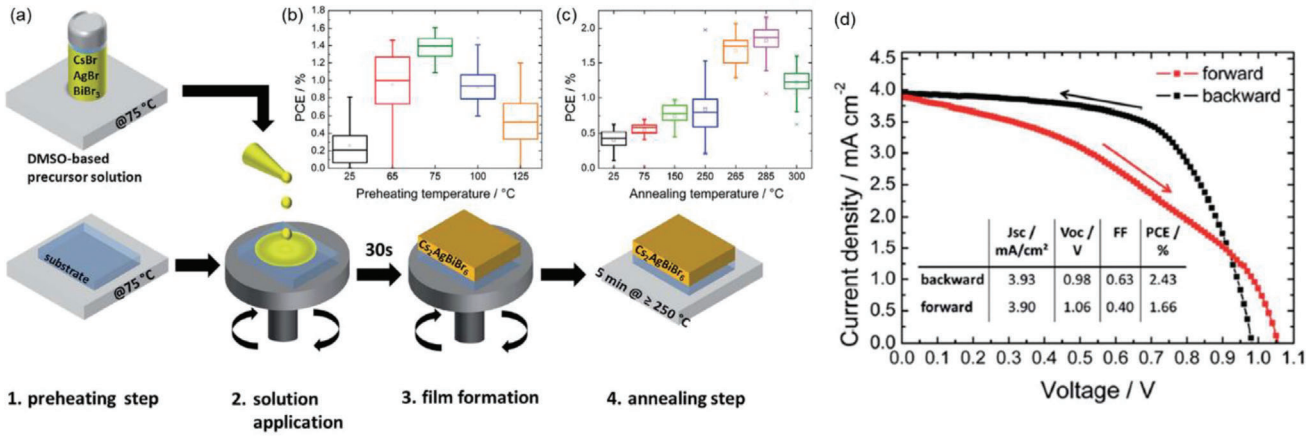

Figure 15. a) A scheme of the $Cs_2AgBiBr_6$ film preparation. b,c) PCE values as a function of b) the preheating temperature (annealed at 250 °C) and c) the annealing temperature (preheated at 75 °C). d) *J–V* curve of the champion device. Reproduced with permission.[257] Copyright 2017, Royal Society of Chemistry.

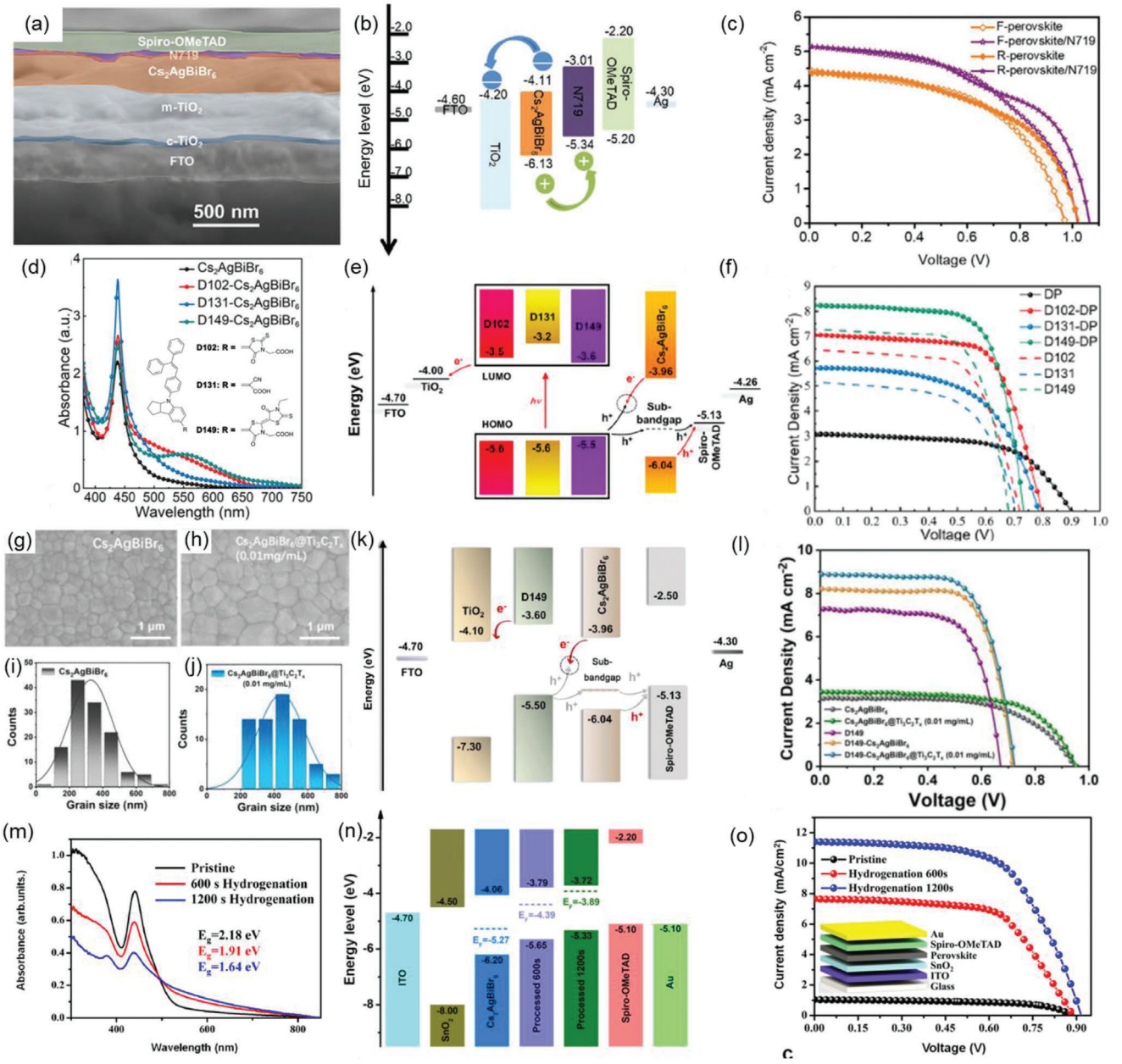

Figure 16. a–c) A cross-section SEM image, b,e,k,n) energy levels, and c,f,l,o) *J–V* curves of $Cs_2AgBiBr_6$-based solar cells. d–f) Absorption spectra of $Cs_2AgBiBr_6$ coated on TiO_2 and D102, D131, and D149-sensitized TiO_2 and molecular structures of the dyes, energy levels, and c,f,l,o) *J–V* curves of corresponding solar cells. g,h) SEM images and i,j) grain size distributions of $Cs_2AgBiBr_6$ film surface without and with $Ti_3C_2T_x$. m) Absorption spectra of pristine and hydrogenated $Cs_2AgBiBr_6$ film. a–c) Reproduced with permission.[264] Copyright 2020, Wiley-VCH; d–f) Reproduced with permission.[265] Copyright 2021, American Chemical Society; g–l) Reproduced with permission.[266] Copyright 2022, Elsevier B.V.; m–o) Reproduced with permission.[267] Copyright 2022, Springer Nature.

et al. reported $Cs_2AgBiBr_6$-based solar cells with N719 (di-tetrabutylammonium cis-bis(isothiocyanato) bis (2,2′-bipyridyl-4,4′ dicarboxylato)ruthenium (II)) dye interlayer (Figures 16a-c).[264] The N719 dye broadens the absorption spectrum, suppresses the charge carrier recombination, and accelerates the hole extraction while passivating surface defects. Therefore, the PCE performance is improved by up to 2.84%. Wang et al. introduced indoline dyes into the solar cell to sensitize the TiO_2 ETL.[265] They compared three types of dyes, D102, D131, and D149, which exhibit strong absorbance beyond 500 nm (**Figure 16**d) and help to crystallize the DP film. They proposed two mechanisms of hole transport from the dyes to spiro-OMeTAD: carrier recombination of the holes generated in the dyes and the electrons generated in the DP and hole transport via the DPs sub-bandgap states (Figure 16e). The D149 dye-based $Cs_2AgBiBr_6$ solar cell recorded an improved PCE of 4.23% due to the broadened and enhanced optical absorbance (Figure 16f). The PCE was further improved to 4.47%

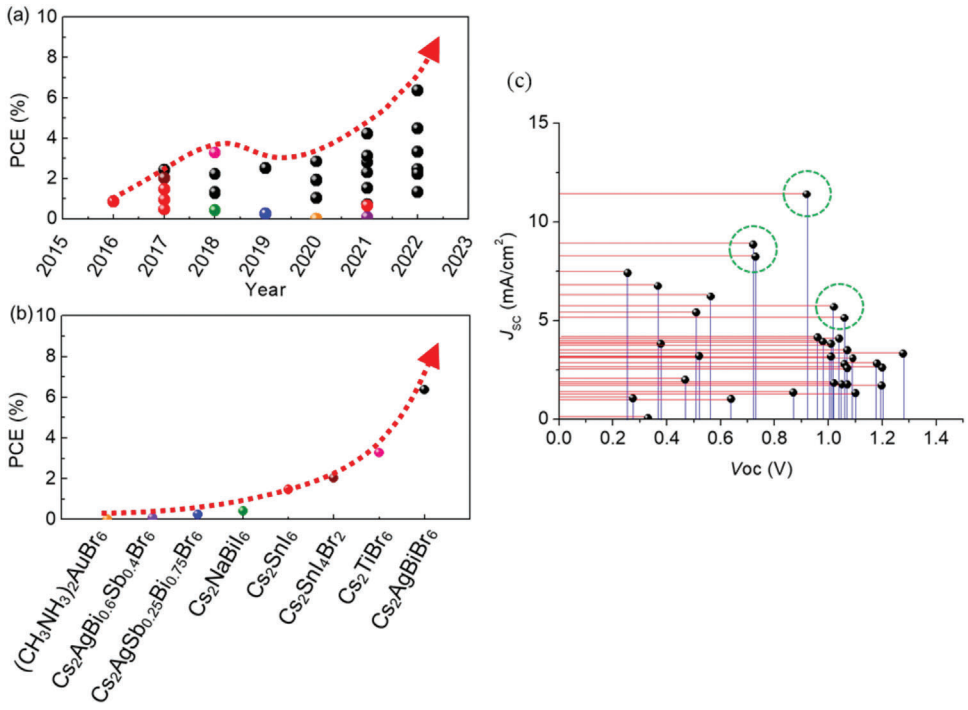

Figure 17. a) PCE trend and b) champion PCE values of DP-based solar cells. The arrows show the trends in the field. c) A graphical presentation of the current-voltage-efficiency relationships for DP solar cells.

by introducing D149 dye and $Ti_3C_2T_x$ MXene nanosheets into the $Cs_2AgBiBr_6$-based solar cell.[266] Here, the $Ti_3C_2T_x$ controls the grain size of the $Cs_2AgBiBr_6$. Figure 16g–j compares the grain sizes of $Cs_2AgBiBr_6$ without and with $Ti_3C_2T_x$. The mean size of the grain is increased from 326 to 440 nm by doping $Ti_3C_2T_x$. Improved crystallinity of the DP resulted in enhanced electron extraction, reducing defect density, and suppressing carrier recombination. $Ti_3C_2T_x$ does not modify the energy levels of the solar cell (Figure 16k). First-principles calculations suggest that the high work function of $Ti_3C_2T_x$ improves the carrier mobility of $Cs_2AgBiBr_6$ by adjusting its valence band. Both the D149 dye and Ti_3C_2Tx contribute to the photocurrent in the $Cs_2AgBiBr_6$-based solar cell (Figure 16l). Recently, Zhang et al. achieved 6.37% PCE in $Cs_2AgBiBr_6$-based solar cells using a hydrogenation method. Doping atomic hydrogen into the interstitial sites of the $Cs_2AgBiBr_6$ lattice modified the bandgap from 2.18 to 1.64 eV (Figures 16m-o).[267] The resulting solar cells showed excellent photo- and thermo-stabilities in a nitrogen environment for 1440 h.

In addition, bandgap engineering of DPs has been carried out to improve the PCE of solar cells. The bandgap of $Cs_2AgBiBr_6$ (≈2 eV) is larger than the ideal band gap (1.34 eV for 33.7%) for a single-junction solar cell.[268] Interestingly, hetero-atom doping into $Cs_2AgBiBr_6$,[269,270] other DPs,[231,247] and vacancy-ordered DPs[248–253] help to lower the bandgap. For example, the bandgap of $Cs_2AgBiBr_6$ was decreased by partial substitution of Bi^{3+} with Sb^{3+}.[269] As a result, the bandgap of $Cs_2AgSb_xBi_{1-x}Br_6$ could be decreased from 2.22 eV (x = 0) to 1.97 eV (x = 0.75). Although the PCE of $Cs_2AgSb_xBi_{1-x}Br_6$ solar cells has been improved from 0.2% to 0.25% by increasing the Sb^{3+}:Bi^{3+} ratio up to 1:3, it was decreased to 0.075% with a further increase in the Sb^{3+}:Bi^{3+} ratio to 1:1 due to formation of large pinholes, and possibly also the formation of defect states. Although Kumar et al. prepared smooth, compact, and pinhole-free $Cs_2AgBi_{0.6}Sb_{0.4}Br_6$ NC films, the PCE value of the corresponding solar cell was only 0.09%.[270] Zhang et al. designed Cs_2NaBiI_6 as a narrow bandgap DP (1.66 eV) for solar cells,[231] and it showed excellent stability (five months in relative humidity of 70%). Ghosh et al. synthesized $MA_2Au_2X_6$ (X = Br, I) with a narrow bandgap of ≈1.0 eV.[247] However, the PCE of these DP-based solar cells was below 1%. Vacancy-ordered DPs have also been considered and exploited for solar cells. Especially, Cs_2SnI_6 has attracted attention due to its narrow bandgap (1.2–1.6 eV), interesting optoelectronic properties, and air stability. Since the 2016's first report on Cs_2SnI_6-based solar cells,[248] optimization of the films in terms of thickness,[249] powder synthesis method,[250] halide mixing,[251] and A-site alloying[252] have been proposed for improving the photovoltaic performance. Although the PCE of solar cells from modified Cs_2SnI_6 samples was higher than unmodified ones, the overall efficiency remains low (<2%), leaving space for further research. In contrast, Chen et al. prepared Cs_2TiBr_6 films with a band gap of 1.8 eV using a low- temperature vapor-based method,[253] which helped improve the PCE to 2.15% without C_{60} and 3.22% with C_{60}, which is only comparable to $Cs_2AgBiBr_6$-based solar cells.

Despite the relatively low PCE, DP-based solar cells overcome the concerns of LHP solar cells, such as lead toxicity and instability in the air. Figure 17a,b summarizes the trend and champion data of DP-based solar cells. The corresponding current-voltage characteristics are presented in **Figure 17**c, showing the significance of improving the J_{SC} values of DP solar cells. The

Table 3. Device configuration and photovoltaic parameter of DP solar cells.

Device configuration	DP film deposition method	Voc [V]	Jsc [mA cm^{-2}]	FF [%]	PCE [%]	Reference
FTO/dense TiO_2/m–TiO_2/$Cs_2AgBiBr_6$/spiro-OMeTAD/Au	One-step spin coating	0.98	3.93	63	2.43	[257]
FTO/c-TiO_2/$Cs_2AgBiBr_6$/PTAA/Au	One-step spin coating	1.02	1.84	67	1.26	[273]
ITO/SnO_2/$Cs_2AgBiBr_6$/P3HT/Au	Low pressure assisted spin coating and annealing	1.07	1.78	69	1.32	[258]
ITO/Cu-NiO/$Cs_2AgBiBr_6$/C_{60}/BCP/Ag <Inverted>	Anti-solvent assisted spin coating and annealing	1.01	3.19	69.2	2.23	[263]
FTO/TiO_2/ $Cs_2AgBiBr_6$/spiro-OMeTAD/MoO_3/Ag	One-step spin coating	1.01	3.82	65	2.51	[274]
ITO/SnO_2/$Cs_2AgBiBr_6$/P3HT/MoO_3/PTAA/Au	One-step spin coating	1.06	2.80	65	1.94	[275]
ITO/SnO_2/$Cs_2AgBiBr_6$/Spiro-OMeTAD/Au	Sequential evaporation	1.10	1.33	70	1.03	[259]
FTO/c-TiO_2/$Cs_2AgBiBr_6$/P3HT/Cu	One-step spin coating	1.07	2.58	69	1.91	[276]
FTO/c-TiO_2/m-TiO_2/$Cs_2AgBiBr_6$/N719/spiro-OMeTAD/Ag	One-step spin coating	1.06	5.13	52.4	2.84	[264]
FTO/SnO_2/$Cs_2AgBiBr_6$/Cu_2O/Au	Sequential vapor deposition	1.198	1.72	73.8	1.52	[260]
ITO/SnO_2/$Cs_2AgBiBr_6$/Spiro-OMeTAD/Ag	Precursor engineering using $BiBr_3(DMSO)_2$, spin coating and annealing	0.87	1.36	61	0.73	[261]
FTO/$Ti_3C_2T_x$-TiO_2/$Cs_2AgBiBr_6$/Spiro-OMeTAD/MoO_3/Ag	One-step spin coating	0.96	4.14	70	2.81	[180]
FTO/c-TiO_2/m-TiO_2/C-ChI/$Cs_2AgBiBr_6$/Spiro-OMeTAD/Ag	One-step spin coating	1.04	4.09	73.12	3.11	[277]
FTO/$Cs_2AgBiBr_6$-D149-TiO_2/$Cs_2AgBiBr_6$/Spiro-OMeTAD/Ag	One-step spin coating	0.73	8.24	70.32	4.23	[265]
FTO/c-TiO_2/m-TiO_2/$Cs_2AgBiBr_6$/Spiro-OMeTAD/Au	Spray coating	1.091	3.1	70	2.3	[262]
FTO/c-TiO_2/m-TiO_2/D149-$Cs_2AgBiBr_6$@$Ti_3C_2T_x$/Ag	One-step spin coating	0.722	8.85	70.1	4.47	[266]
FTO/TiO_2/ $Cs_2AgBiBr_6$/Y6/PBDB-T/MoO_x/Ag	One-step spin coating with antisolvent	1.278	3.34	77.5	3.31	[278]
FTO/TiO_2/BMPyr/$Cs_2AgBiBr_6$/carbon	One-step spin coating	1.20	2.61	71.02	2.22	[279]
FTO/c-TiO_2/m-TiO_2/$Cs_2AgBiBr_6$(3D)/$(PEA)_4AgBiBr_8$(2D)/Spiro-OMeTAD/Au	One-step spin coating	1.07	3.5	66	2.47	[220]
ITO/c-TiO_2/m-TiO_2/$Cs_2AgBiBr_6$/Spiro-OMeTAD/Au	One-step spin coating	1.05	1.77	71.67	1.33	[280]
ITO/SnO_2/ $Cs_2AgBiBr_6$/Spiro-OMeTAD/Au	One-step spin coating with antisolvent	0.92	11.40	60.93	6.37	[267]
FTO/TiO_2/$Cs_2AgBiBr_6$/PMMA/carbon	One-step spin coating	1.18	2.82	67.6	2.25	[281]
	Other than Cs2AgBiBr6					
FTO/c-TiO_2/m-TiO_2/$Cs_2AgSb_{0.25}Bi_{0.75}Br_6$/Spiro-OMeTAD/Au	One-step spin coating	0.64	1.03	–	0.25	[269]
ITO/NiO_x/$Cs_2AgBi_{0.6}Sb_{0.4}Br_6$/PCBM/Ag	One-step spin coating	0.275	1.07	31	0.09	[270]
FTO/c-TiO_2/m-TiO_2/Cs_2NaBiI_6/Spiro-OMeTAD/Au	One-step spin coating	0.47	1.99	44	0.42	[231]
FTO/m-TiO_2/MA_2AuBr_6/PTAA/Au	Reactive polyiodide melt	0.33	0.052	41.04	0.007	[247]
FTO/ZnO seed layer/ZnO nanowires/Cs_2SnI_6/P3HT/Ag	One-step spin coating	0.52	3.2	51.5	0.857	[248]
FTO/TiO_2/Cs_2SnI_6/P3HT/Ag	Two-step vapor deposition	0.51	5.41	35	0.96	[249]
FTO/c-TiO_2/Cs_2SnI_6/P3HT/Ag	Chemical bath deposition	0.256	7.41	24.5	0.47	[250]
FTO/TiO_2/Sn-TiO_2/$Cs_2SnI_4Br_2$/solid-state Cs_2SnI_6/LPAH /FTO	Two-step solution process	0.563	6.225	57.7	2.025	[251]
FTO/TiO_2/Sn-TiO_2/Cs_2SnI_6/LPAH/FTO	Two-step solution process	0.367	6.752	59.5	1.47	[251]
ITO/CuI/Ag-alloyed Cs_2SnI_6/PCBM/AZO/Ag	Spray coating	0.378	3.821	45.6	0.659	[252]
FTO/TiO_2/C_{60}/Cs_2TiBr_6/P3HT/Au	Two-step vapor deposition	1.02	5.69	56.4	3.28	[253]

current and voltage values are summarized in **Table 3**. Among all, $Cs_2AgBiBr_6$-based solar cells recorded higher PCE values than that of other DPs. The PCE values have been improved from 2.43% in 2017 to 6.37% in 2022. The DP-based solar cell with the champion PCE value exhibits excellent photo- and thermostabilities in a nitrogen environment for two months. However, the efficiencies of reported DP-based solar cells are still lower than those of LHP solar cells. The main issues of DP-based solar cells are the large band gaps, technical challenges with device engineering, and the large gap between experimental and simulated PCE values. Among various DP samples, $Cs_2AgBiBr_6$ is not ideal for industrial solar cells mainly due to its large and indirect bandgaps.[271] Other chemical compositions, vacancy-ordered DPs, and hetero-atom doping have been tried to overcome the bandgap issue. There is still a large room for improving perovskite layer quality, for example, by adopting inverted or multijunction solar cells or by integrating with other absorbers. Furthermore, machine learning could help to find suitable DP for efficient solar cells.[272] Although various high-efficiency DP solar cells are predicted by density functional theory and first principle calculations, most of them are still unexplored experimentally. The gap between the theoretical and experimentally demonstrated PCE values needs to be filled by further collaboration between experimental and theoretical groups.

Table 4. The performance of electroluminescent LEDs fabricated based on Sn perovskites. ν_{EL}, FWHM, EQE, L_{max}, and R_{max} refer to the photon energy of electroluminescence (EL) peak, full-width of half-maximum, external quantum efficiency, the maximum luminescence (in cd m^{-2}), and the maximum radiance (in W sr^{-1} m^{-2}), respectively.

Composition	Device structure (PK refers to Sn-based perovskites)	ν_{EL} [eV]	FWHM [eV]	EQE [%]	L_{max} [cd m^{-2}] or R_{max} [W sr^{-1} m^{-2}]	Reference
$MASn(Br_xI_{1-x})_3$ thin film	ITO/PEDOT:PSS/PK/F8/Ca/Ag	1.3-1.86	≈0.2	0.007-0.72	0.087 – 1.8 W sr^{-1} m^{-2}	[283]
$FASnI_3$ thin film	ITO/PEDOT:PSS/PK/TPBi/LiF/Al	1.38	≈0.15	1.5	145 W sr^{-1} m^{-2}	[285]
$CsSnI_3$ thin film	ITO/PEDOT:PSS/PK/PBD/LiF/Al	1.31	≈0.2	3.8	40 W sr^{-1} m^{-2}	[284]
$CsSnI_3$ thin film	ITO/PEDOT:PSS/PK/B3PYMPM/LiF/Al	1.3	≈0.15	5.4	162 W sr^{-1} m^{-2}	[319]
$CsSnI_3$ NCs	ITO/PEDOT:PSS/PK/LiF/Al	1.31	≈0.15	0.007	0.05 W sr^{-1} m^{-2}	[324]
$CsSnBr_3$ thin film	FTO/PFI + PEDOT:PSS/PK/TPBI/LiF/Al	1.84	≈0.29	N/A	160 cd m^{-2}	[316]
$CsSn(Br_xI_{1-x})_3$ Thin films	ITO/PEDOT:PSS/PK/PBD/LiF/Al	1.83-1.31	≈0.15	0.002-0.013	0.01 – 0.13 W sr^{-1} m^{-2}	[315]
PEA_2SnI_4 thin film	ITO/PEDOT:PSS/PK/F8/LiF/Al	2.01	0.12	N/A	0.15 cd m^{-2}	[58]
PEA_2SnI_4 thin film	ITO/PEDOT:PSS/PK/TPBi/LiF/Al	1.96	0.07	0.3	70 cd m^{-2}	[317]
PEA_2SnI_4 thin film	ITO/TPBi/LiF/PK/TPBi/LiF/Al	1.97	0.09	0.16	58 cd m^{-2}	[57]
TEA_2SnI_4 thin film	ITO/TPBi/LiF/PK/TPBi/LiF/Al	1.94	0.09	0.62	322 cd m^{-2}	[57]
PEA_2SnI_4 thin film	ITO/PEDOT:PSS/PK/TPBi/LiF/Al	1.97	0.09	0.52	355 cd m^{-2}	[299]
$(OAm)_2SnBr_4$ microplates	ITO/PEI-ZnO/PK/TCTA/ MoO_3/Au	1.98	0.52	0.1	350 cd m^{-2}	[300]

4.2. Light-Emitting Diodes (LEDs)

4.2.1. Sn and Ge-based Perovskite LEDs

Current Status: Apart from photovoltaics, Sn/Ge-based perovskites have also been employed as light emitters, either in the form of thin films or colloidal NCs (**Tables 4** and **5**).[2,282,54] In this part of the review, we will first discuss the emission properties of several Sn and Ge-based perovskites, followed by a discussion of the current progress of LED performance based on these. Because several low-dimensional perovskites have recently drawn more attention in the field of light emission, we will focus the discussion in the first section on materials with different dimensionalities. In the second section, we will separately discuss electroluminescence LEDs (EL LEDs) and phosphor-converted LEDs (PC LEDs), which are the two common LEDs reported thus far.

3D $MASnI_3$, $FASnI_3$, and $CsSnI_3$ films have been heavily investigated since their direct bandgaps, between 1.3 to 1.4 eV, could lead to intense PL emissions with minimal Stokes shifts.[283–285] On the other hand, some of these Sn-based perovskites have been synthesized as NCs, where the stronger quantum confinement tends to widen bandgaps and create more discrete energy levels. As a result, Sn-based perovskite NCs have PL peaks with narrower full width at half maxima (FWHM), which is advantageous for achieving higher color saturation and important for ultrahigh-definition displays. Indeed, both $CsSnI_3$ and $FASnI_3$ NCs showed a 0.1 eV blueshift in their bandgaps with a PL FWHM between 70 and 100 meV,[54,67,286] which was smaller than their thin film counterparts. Additionally, by changing the A-site or halide site component (**Figure 18**a), the PL position of Sn-based perovskites can be tuned over a wide range, from visible to NIR (2.95–1.3 eV).[283,287,288] Figure 18b displays the energy levels and bandgaps of several Sn-based perovskites with different compositions, where we can see a wide tuneable range of bandgaps from 3.55 to 1.24 eV.[203] However, in contrast to LHP NCs with extremely high PLQYs, the highest PLQY reported for Sn-based perovskite NCs ($CsSnI_3$ NCs) so far is only 18.4%,[55] which is far below the PLQYs of LHP NCs (approaching 100%).[29,289] On the other hand, 3D Ge-based perovskites have slightly larger bandgaps than Sn-based perovskites. For example, $MAGeI_3$, $FAGeI_3$, and $CsGeI_3$ thin films have shown a direct bandgap of around 1.6, 1.9, and 2.2 eV, respectively.[198] Similar to Sn-based perovskites, alloying of A-site cations and halide ions could also tune the bandgaps of Ge-based perovskites, which were limited from the UV to the visible region (1.6–3.67 eV).[290,291] Although $MA_{1-x}FA_xGeI_3$ thin films have exhibited tuneable PL from 1.97 to 2.25 eV,[292] very few studies on the

Table 5. Phosphor-converted LEDs fabricated based on Sn perovskites. CCT, CIE, and CRI refers to correlated color temperature, color coordinates in the CIE 1931 graph, and color rendering index, respectively.

Composition	Device structure (PK refers to Sn-based perovskites)	CCT [K]	CIE	CRI	Reference
Cs_2SnBr_6 NCs	Cs_2SnBr_6 + $(Sr_5(PO_4)_3Cl:Eu^{2+})$/ (mixed in PDMS)/ 365 nm chip	2006	(0.52, 0.41)	84	[318]
$(C_4N_2H_{14}Br)_4SnBr_6$ single crystals	$(C_4N_2H_{14}Br)_4SnBr_6$ + $BaMgAl_{10}O_{17}:Eu^{2+}$ (mixed in PDMS)/ 340 nm chip	4946	(0.35, 0.39)	70	[308]
$(OCTAm)_2SnBr_4$ crystals	$(OCTAm)SnBr_4$ + $BaMgAl_{10}O_{17}:Eu^{2+}$ + G2762 (mixed in PS)/ 365 nm chip	2500/ 5635/ 6530	(0.49, 0.42)/ (0.33, 0.26)/ (0.33, 0.31)	69/ 81/ 89	[75]
Cs_2SnCl_6:0.59% Sb^{3+} crystals	Cs_2SnCl_6:0.59% Sb^{3+} + Cs_2SnCl_6:2.75% Bi^{3+} + 6815 $Ba_2Sr_2SiO_4:Eu^{2+}$ (mixed in silicone)/ 380 nm chip	6815	(0.30, 0.37)	81	[311]
Cs_2SnCl_6:2.75% Bi^{3+} crystals	Cs_2SnCl_6:2.75% Bi^{3+} + $Ba_2Sr_2SiO_4:Eu^{2+}$ + $GaAlSiN_3:Eu^{2+}$ (mixed in curable resin)/ 365 nm chip	2087/ 4486	(0.55,0.45)/ (0.36, 0.37)	N/A	[312]

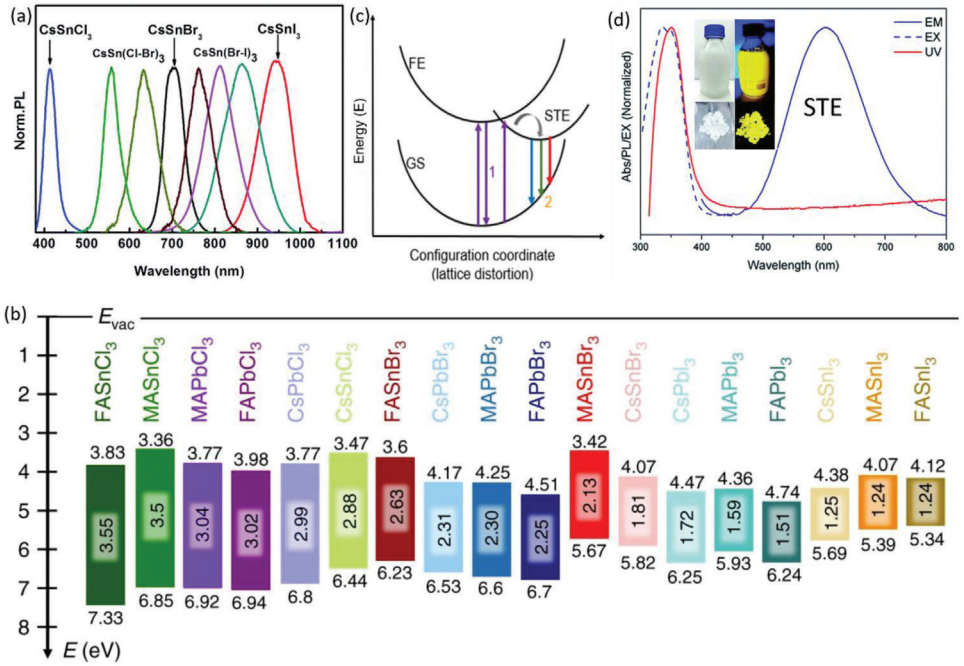

Figure 18. a) PL spectra of 3D $CsSnX_3$ (X = Cl, Br, I) thin films with different halide compositions. Reproduced with permission.[288] Coypright 2016, Royal Society of Chemistry. b) Schematic illustration of energy levels of ABX_3 perovskites with different A (MA, FA, and Cs), B (Sn and Pb), and X (Cl, Br, and I). The bandgaps are obtained from the UV–vis absorption measurements, whereas the ionization energy (IE) and electron affinity (EA) are obtained from the inverse photoelectron spectroscopy. Reprinted with permission.[203] Copyright 2019, Springer Nature. c) Configuration coordinate diagram depicting two possible emission mechanisms of Sn- and Ge-based perovskites. GS, FE, and STE represent the ground state, free exciton, and self-trapped exciton, respectively. 3D perovskites usually exhibit FE emission while low-dimensional perovskites tend to show STE emission, d) UV–vis absorption (UV), PL excitation (EX) and emission (PL) spectra of 2D $(OCTAm)_2SnBr_4$ colloidal solution. The inset shows the photographs of the samples in solution and powder form. Reproduced under the terms of the CC BY-NC license.[75] Copyright 2019, The Authors, published by Royal Society of Chemistry.

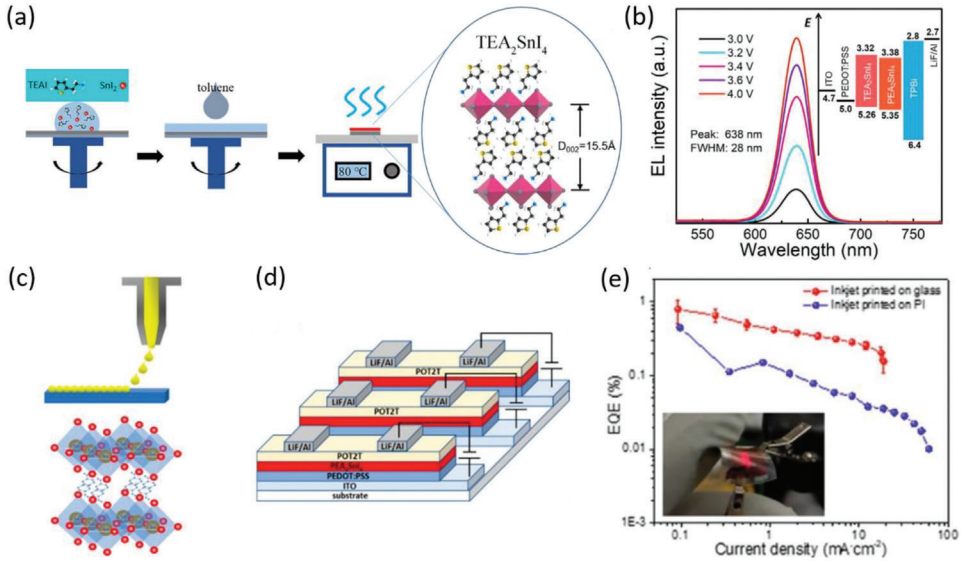

Figure 19. Schematic illustration of the preparation of 2D Sn-based perovskite films for LEDs (TEA: 2-thiopheneethyllammonium). (b) The electroluminescence (EL) spectra of TEA_2SnI_4-based device at different voltages. Figures (a) and (b) are reproduced with permission.[57] Copyright 2020, American Chemical Society. (c) Inkjet printing of PEA_2SnI_4 films for LEDs fabrication. (d) LED device structure made of inkjet-printed PEA_2SnI_4 films. (e) EQE versus current density for the PEA_2SnI_4 LEDs fabricated on glass and polyimide (PI) flexible substrates (inset: photograph of a red-emitting flexible LED operating at 5 V). Panels (c)–(e) are reproduced with permission.[303] Copyright 2022, American Chemical Society.

emission properties of other 3D Ge-based perovskites have been reported thus far.

Compared to their 3D counterparts, 2D Sn- and Ge-based perovskites usually have larger bandgaps (≈2 eV or above), larger exciton binding energies (hundreds of meV,[293] c.f., 20–30 meV for 3D counterparts[294]), and higher environmental stability due to the presence of long-chain organic layers acting as barriers to moisture ingress.[295] Interestingly, two different emission mechanisms have been identified in 2D Sn- and Ge-based perovskites and can be interpreted by a configuration coordinate diagram, as illustrated in Figure 18c.[296,93] The curves in a configuration coordinate diagram describe the total energy of the lattice in the dark or under illumination at different lattice distortions, which is represented by the configuration coordinate. Following photoexcitation, the lattice changes from the ground state to the free exciton state. Afterward, excitons can relax directly from the free exciton to the ground state without lattice distortion (path 1 in Figure 18c), and this would normally lead to a narrow PL with minimal Stokes shifts.[297,93] On the other hand, if the coupling between the excitons (or free charge-carriers) with phonons is strong enough, lattice distortion occurs, and the free exciton can enter into the STE state, leading to the localization of the exciton wavefunction, with a radial distance on the order of a unit cell or smaller. A broadband white light emission with a large Stokes shift often occurs when STEs relax to the GS (path 2 in Figure 18c).[298,93] Such a phenomenon is undesirable for ultrahigh definition displays but offers opportunities to achieve solid-state white light emitters.

The emission of 2D Sn-based perovskites is highly associated with the types of A-site organic cations used, which could lead to either extremely narrow PL (free exciton emission) or broadband white light (STE emission). In terms of free exciton emission, $(PEA)_2SnI_4$ (PEA = phenylethylammonium) films have demonstrated a PL at 2 eV with a small FWHM of 100 meV and Stokes shift of 40 meV.[299] A PLQY of 9.7% was reached in $(PEA)_2SnI_4$ films after surface passivation. In the STE emission case, the $(OCTAm)_2SnBr_4$ (OCTAm = octylammonium) colloidal solution has shown a PL at 2.07 eV with a large FWHM and Stokes shift of 470 meV and 1010 meV, respectively (Figure 18d).[75] A near-unity PLQY and microsecond PL lifetime were also observed in both $(OCTAm)_2SnBr_4$ and $(OAm)_2SnBr_4$ (OCT = octylammonium; OAm = oleylammonium),[300,75] suggesting that photoexcited charge-carriers could relax more efficiently through STE relaxation. Furthermore, the high PLQY could be maintained in 2D Sn-based perovskites stored in an ambient environment for up to 240 days, which verifies their high air stability.[75] The PL peaks of 2D Sn-based perovskites could be also tuned by using various halide compositions or A-site organic cations with different chain lengths.[301,75] On the other hand, 2D Ge-based perovskites show poorer emission properties compared to Sn-based counterparts. For instance, although the $(Bmpip)_2GeBr_4$ (Bmpip = 1-butyl-1-methylpiperidinium) single crystal has displayed a broadband STE emission at 1.85 eV with a large Stokes shift up to 600 meV, its PLQY was found to be less than 1%.[302] LEDs made of 2D Sn-based perovskites are often solution-processed by using solutions containing tin halides and organic cation molecules, as illustrated in **Figure 19**a.[57] Among various organic cations, PEA and TEA (thiopheneethyllammonium) molecules have been extensively explored to prepare relatively stable 2D Sn-based perovskites with a reasonable PLQY for LEDs. Particularly, TEA_2SnI_4-based LEDs exhibit electroluminescence (EL) spectra peaking at ≈1.94 eV (638 nm), and an EQE of 0.62% (Figure 19b).[57] EL spectra of 2D Sn-based perovskites slightly vary depending on the composed organic cations and are generally consistent with corresponding PL spectra. In addition, 2D Sn-based perovskite LEDs could be also fabricated on flexible

substrates by inkjet printing, and have reached an EQE of 1% in PEA_2SnI_4-based LEDs (Figure 19c–e).[303]

Surprisingly, no PL emission has been reported in any 1D Sn and Ge-based perovskites thus far, which might be associated with their facile transformation into 0D structures under photoexcitation.[304] 0D Sn-based perovskites have also exhibited larger bandgaps (≈3 eV or above) and enhanced air stability compared to their 2D counterparts.[305] The significant dimensionality reduction further facilitates STE formation, owing to the removal of the energy barrier for self-trapping.[298] A broadband STE emission is hence more commonly observed in 0D Sn-based perovskites. For example, $(C_4N_2H_{14}Br)_4Sn(Br_{0.5}I_{0.5})_6$ could emit a broadband PL at 2.13 eV (FWHM ≈470 meV) with a large Stokes shift of 1000 meV.[306] The center of the broadband emission peak could be also tuned by changing the composition of halides or A-site cations.[307] Several 0D Sn-based perovskites have shown microsecond PL lifetimes and near-unity PLQYs, possibly due to their significantly enhanced exciton binding energies (e.g., >1 eV in Cs_4SnBr_6).[306,308,309] It is also worth mentioning that the PL intensity from 0D Sn-based perovskites could not be saturated at higher excited power,[308] which evidenced the intrinsic feature of STE emission and excluded the possibility of defect emission.

Vacancy-ordered Sn-based double perovskites, with the general formula $A_2Sn^{IV}X_6$, are also promising emitters, especially since the Sn cations are in the more stable 4+ oxidation state. Vacancy-ordered Sn-based perovskites exhibit a wide range of bandgaps (1.3–4.9 eV) depending on the halide composition.[310] While different from 2D and 0D Sn-based perovskites, carrier-phonon coupling in vacancy-ordered Sn-based double perovskites tends to be weaker, in part due to their dispersed band edges.[256] As a result, a narrow free exciton emission has been commonly seen in these materials. For instance, a PL at 2 eV with a small FWHM of 160 meV has been reported in Cs_2SnI_6 NCs.[78] Nevertheless, the potentially weaker excitonic binding strength and higher defect density could lead to low PLQYs (<1%) and shorter PL lifetimes, of the order of only a few nanoseconds.[78] Interestingly, a broader PL at 2.73 eV (FWHM = 400 meV) and 2.06 eV (FWHM = 350 meV) could be individually achieved in Sb- and Bi-doped Cs_2SnCl_6 crystals.[311,312] Although the former was from defect emission, the latter was attributed to the transition from the triplet state to the ground state in Sb^{3+} octahedrally coordinated by chlorides. Owing to the local minima in the excited-state potential energy surface for triplets caused by Jahn–Teller distortions[313,314], two PL peaks could be seen at lower temperatures. A higher PLQY of ≈37% and 80% could be also reached in Sb- and Bi-doped Cs_2SnCl_6 crystals, respectively.

So far, no emitters made from Ge-based perovskites have been reported, while some EL LEDs and phosphor-converted (PC) LEDs fabricated with Sn-based perovskites have been reported (Tables 4 and 5). EL LEDs emit light via free exciton recombination when charge-carriers are injected through the injection layers from the electrode, and the energy diagram of a typical $CsSnI_3$ EL LED is illustrated in **Figure 20**a. On the other hand, PC LEDs integrated phosphors mixed in a polymer with commercial UV LED chips, which can pump the phosphors to generate broadband white light.

As shown in Table 4, EL LEDs fabricated with 3D Sn-based perovskites have shown potential for NIR to red light emission, and the emission energy can be tuned by changing their halide compositions. Nevertheless, they could also easily degrade with air exposure, leading to a blue shift in the EL (Figure 20c) and a decrease in EQE.[283,315] It has been shown that by controlling the crystallization process through the inclusion of additives such as phenethylamine iodide (PEAI) or SnF_2, the operational lifetimes (time for the initial peak radiance of the LED to decrease by 50% under continuous operation) of $FASnI_3$ and $CsSnBr_3$ LEDs in an inert environment could exceed 10 and 30 hours (Figure 20b), respectively.[285,316] Recently, LEDs fabricated with 2D Sn-based perovskites have also gained more attention owing to their higher intrinsic stability in the air. Particularly, a pure-red EL with rather small FWHMs (less than 0.1 eV) have been demonstrated in $(PEA)_2SnI_4$ as well as $(TEA)_2SnI_4$ LEDs, and this EL was stable in a wide voltage range[299,317,57] (Figure 20b). These LEDs also displayed a low turn-on voltage of 2.2–2.3 V and a maximum luminescence L_{max} over 300 cd m^{-2}. Nevertheless, they still encounter the issues of low EQEs (<1%)[57] and poor operational stability (degraded within a few seconds or minutes),[57,299] which has been attributed to the rapid film decomposition caused by Joule heating rather than oxidation. Interestingly, a broadband orange light with a FWHM of 0.52 eV could be also reached in EL LEDs based on $(OAm)_2SnBr_4$ microplates.[300] This EL resulted from the STE emission with a FWHM that could be broadened when more charge-carriers were thermally activated into the trapped state at higher temperatures. Similarly, $(OAm)_2SnBr_4$ LEDs also showed a high L_{max} of 350 cd m^{-2} but a low EQE of only 0.1%.

In terms of PC LEDs, several 0D, 2D, and vacancy-ordered Sn-based double perovskites with strong STE emission have been employed as phosphors. Due to the high air stability of these materials, the emission spectra from these LEDs could be usually maintained for over a few months,[75,308] as displayed in Figure 20e. By tuning the ratio of the mixed phosphors, white light emission with different color coordinates in the Commission Internationale de l'Éclairage (CIE) 1931 graph could be achieved in $(OCTAm)_2SnBr_4$ and Bi-doped Cs_2SnCl_6 LEDs.[75,312] The emission light spectra from these LEDs could range from "very warm white light" to "day white light", which corresponds to a correlated color temperature (CCT) ranging from around 2000 K to over 6000 K, as shown in Figure 20f. Moreover, high color rendering index (CRI) values over 80,[75,311,318] which reached the requirement of commercial white light LEDs, have also been demonstrated in $(OCTAm)_2SnBr_4$ and Sb-doped Cs_2SnCl_6 LEDs. At present, Sn-based perovskites are more promising in PC LED applications compared to EL LEDs.

Outstanding Challenges: LHP LEDs have exhibited EQEs approaching 30% with peak luminance exceeding 10^5 cd m^{-2},[98] which substantially outperforms all Sn-based perovskite LEDs reported so far. The greatest challenge for Sn- and Ge-based perovskites remains the facile oxidation of Sn^{2+} and Ge^{2+} to the +4 oxidation state,[305,320] which could lead to their ambient instability, high defect densities, and metallic-like conductivity feature due to self-doping.[321] For Sn-based perovskites, it has been claimed that self-doping could lead to very high hole concentration, which further caused unbalanced charge-injection in their LEDs, hence reducing the EQEs.[319] Additionally, poor film morphology resulting from a fast crystallization process[293] or low precursor solubilities in common organic solvents[322] is another factor limiting the device performance of Sn- and Ge-based perovskites. Although NCs could usually show better emission

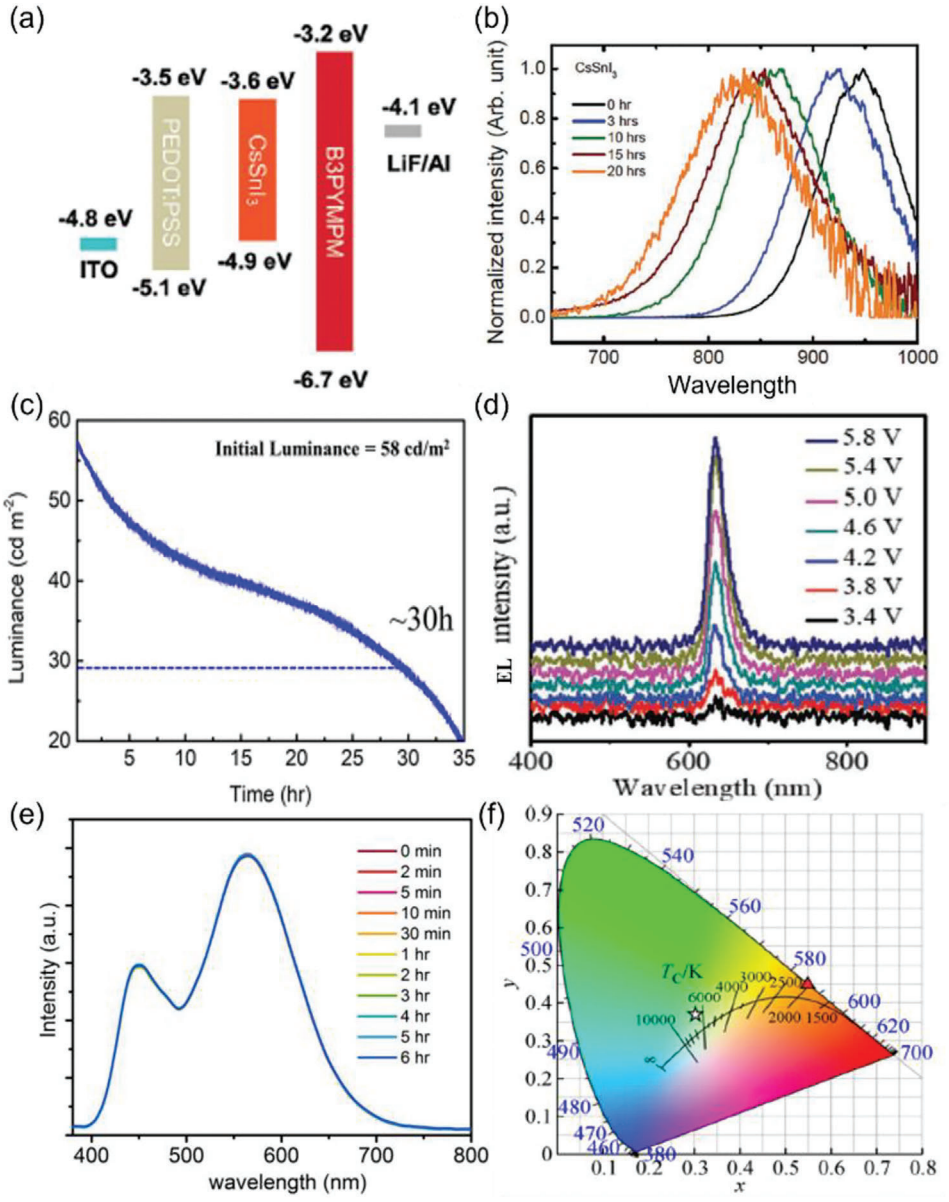

Figure 20. a) A typical energy level diagram of a $CsSnI_3$ LED. PEDOT:PSS and B3PYMPM is poly(3,4-ethylenedioxythiophene):poly(styrenesulfonate) and 4,6-Bis(3,5-di(pyridin-3-yl)phenyl)−2-methylpyrimidine, which acts as the hole and electron injection layer, respectively. Reproduced with permission.[319] Coypright 2021, John Wiley and Sons. b) EL spectra of a 3D $CsSnI_3$ LED exposed to air at various times. Reproduced with permission.[315] Coypright 2021, John Wiley and Sons. c) The time evolution of the luminance of a $CsSnBr_3$ LED under continuous operation. Reproduced with permission.[316] Coypright 2022, American Chemical Society. d) The EL spectra of a 2D PEA_2SnI_4 LED operated at different voltages. Reproduced under the terms of CC BY 4.0.[317] Copyright 2020, The Authors, published by Wiley-VCH. e) The emission spectra of a 0D $(C_4N_2H_{14}Br)_4SnBr_6$ LED pumped by a 340 nm UV LED under air for more than six hours. Reproduced under the terms of CC BY 3.0.[308] Copyright 2018, The Authors, published by the Royal Society of Chemistry. f) The Commission Internationale de l'Éclairage (CIE) 1931 graph and correlated color temperatures (CCTs) of white light. The red triangle and white star are the color coordinate of a PC LED based on Sb-doped Cs_2SnCl_6 only and Sb-doped Cs_2SnCl_6 with other phosphors, respectively. Reproduced with permission.[311] Coypright 2019, Springer Nature.

properties than thin films, there are few reports of Sn- and Ge-based perovskite NC LEDs. This could be attributed to several reasons: first, it is still challenging to synthesize stable Ge-based perovskite NCs through hot injection;[320] second, the insulating nature of long-chain ligands surrounding NCs would highly impede charge-injection;[323] thirdly, during LED operation, ligands could be also detached, which potentially facilitated unwanted NC aggregation or increased defect densities;[323] eventually, currents might leak easily through NC films since they are less compact compared to bulk films.[324]

Future Prospects: Although SnX_2 (X = halides) additives,[321,325] metallic Sn powders,[326] organic antioxidants,[107] and perfluorooctanoic acid[78] are effective in suppressing the oxidation of Sn^{2+}, we believe that it is more important to identify

Table 6. Performance summary of the NCs and thin film WLEDs.

EML	Device structure	EL Peak [nm]	EQE_{max} [%]	L_{max} [cd m^{-2}]	Lifetime [min]	Reference
$Cs_2Ag_{0.6}Na_{0.4}InCl_6$	ZnO/PEIE/EML(VTE)/TAPC/MoO_3/Al	552	N/A	≈50	10@50 mA cm^{-2}	[92]
$Cs_2AgIn_{0.9}Bi_{0.1}Cl_6$	PVK/EML/TPBi/LiF/Al	≈410 and 610	0.08	158	48.5@15 mA cm^{-2}	[328]
$Cs_2AgIn_xBi_{1-x}Cl_6$	ITO/PEDOT:PSS/TFB/PVK:NPLs/ZnO/Al	557 nm	≈ 0.01%	58	N/A	[329]

the controversial degradation mechanism of Sn-based perovskites in order to fundamentally resolve their instability issue. Similar studies on Ge-based perovskites are even more crucial since they have not yet been realized in working LEDs. In addition, to achieve higher EQEs in Sn-based perovskite LEDs, more balanced charge-injection should be aimed for, possibly by modifying the film morphology or injection layers. It is also worth mentioning that LEDs fabricated with low-dimensional and vacancy-ordered Sn-based double perovskites have exhibited not only higher color purity or CRI values but also enhanced ambient stability compared to their 3D counterparts. We hence expect that these materials along with analogous Ge-based derivatives, will gain more attention in future studies. Finally, considering the outstanding emission properties in Sn-based perovskite NCs, we also encourage more investigations into relevant ligand engineering, which plays an important role in both charge-carrier transport and defect passivation.

4.2.2. Double Perovskite LEDs

With consideration of environmental friendliness, lead-free luminescent double perovskite (DP) materials with superior stability and high PLQY have emerged as promising candidates for LEDs. The flexibility of compositional engineering and the diversity of the band structure of DPs enables the achievement of multicolor luminescence covering the full visible–NIR gamut. This section summarizes recent progress in lead-free DP-based LEDs.

Double Perovskite Thin Film/NCs LEDs: In 2018, Tang's group reported stable white emission from Bi^{3+}-doped $Cs_2Ag_{0.6}Na_{0.4}InCl_6$ DPs and demonstrated highly efficient white emission based on the thin film LEDs driven by an electric field.[92] They claim that the alloying of $Cs_2AgInCl_6$ with Na+ catios results in transition of a parity forbidden transition to an allowed transition (**Figure 21**a). Thus, the alloying of sodium and bismuth cations with $Cs_2AgInCl_6$ leads to a dramatic increase in PLQY from <0.1% to 86%. The LEDs fabricated via thermally evaporated $Cs_2Ag_{0.6}Na_{0.4}InCl_6$ films exhibit bias-insensitive broadband emission with a peak current efficiency of 0.11 cd A^{-1}. Although the samples showed excellent stability under ambient conditions (Figure 21b), the corresponding LEDs exhibited yellowish electroluminescence, indicating the change of phase under the electric field. This may be attributed to poor film quality and uncontrollable composition segregation. After this early work, several other groups have reported the synthesis and luminescence properties of the doped-DP thin films and NCs and demonstrated the fabrication of LEDs. **Table 6** summarizes some of the representative work on DP (thin films and power)-based LEDs.

For instance, Zhang et al. synthesized Tb^{3+}, Sb^{3+} co-doped $Cs_2NaInCl_6$ NCs with high PLQY blue-green emission (74%), which then transformed into white emission with Mn^{2+}-doping.[327] The corresponding light down-conversion-based LEDs emit warm white light with a color rendering index (CRI) is 89.2 and a correlated color temperature (CCT) is 3371 K, meeting the standard of warm white lighting (2500–3500 K). After the early reports on strongly emissive bulk DPs, researchers have demonstrated the synthesis of colloidal doped-DP NCs by wet chemical approaches that were used for LHPs.[292] For instance, $Cs_2AgIn_{1-x}Bi_xCl_6$ DPs have been synthesized in the form of colloidal NCs with controlled size distribution and emit white light.[102] The NCs can be used in light down-conversion-based LEDs by incorporating them into a poly methyl methylacrylate (PMMA) matrix followed by coating on 380 nm LED chips. The down-converting LEDs exhibit white light emission with CIE coordinates of (0.36, 0.35), CRI values of ≈91, and correlated color temperature (CCT) of 4443 K. However, the progress on DP NC-based LEDs is much slower as compared to that of LHPs. There are only a few reports demonstrating the electroluminescence from DP LEDs. Recently, Qu et al. synthesized $Cs_2AgIn_{0.9}Bi_{0.1}Cl_6$ NCs with a PLQY of 31.4% and they demonstrated the fabrication of electrically excited white LEDs (WLEDs). Although the films showed bright and uniform warm white emission under UV excitation, the NC-WLED exhibited weak electroluminescence (158 cd m^{-2}) with an EQE of 0.08%, as shown in Figure 21c,d.[328] Very recently, DP-based LEDs using two-dimensional (2D) $Cs_2AgIn_xBi_{1-x}Cl_6$ ($0 \leq x \leq 1$) NPls were reported, showing a luminance maximum of 58 cd/m^2 with a peak current efficiency of 0.013 cd/A (Figure 21e,f).[329] However, the resulting EQE and T_{50} values are significantly lower than the benchmark LEDs made of LHP NCs. This is probably due to the wide band gap (>3.6 eV) and poor charge carrier mobility in double perovskites. The efficiency of DP-LEDs needs to be significantly improved for practical applications. We believe that a better understanding of the charge transport properties in DP systems would help to improve the efficiency of the corresponding LEDs. Meanwhile, researchers have turned their attention to DP polycrystalline and single crystals to achieve white light from single-component systems.

Double Perovskite Powder-Based LEDs: Despite slow progress in DP-based electroluminescent devices, a feasible application of double perovskites is the down-conversion LEDs based on covering GaN-based blue LED chips with highly luminescent DP powders (phosphors). As shown in **Figure 22**a, Nie et al. synthesized $Cs_2NaInCl_6$:Sb^{3+} DPs by the hydrothermal method, emitting blue PL (PLQY≈ 90%). The corresponding down-conversion LEDs exhibit color coordinates of (0.147, 0.078).[330] In such

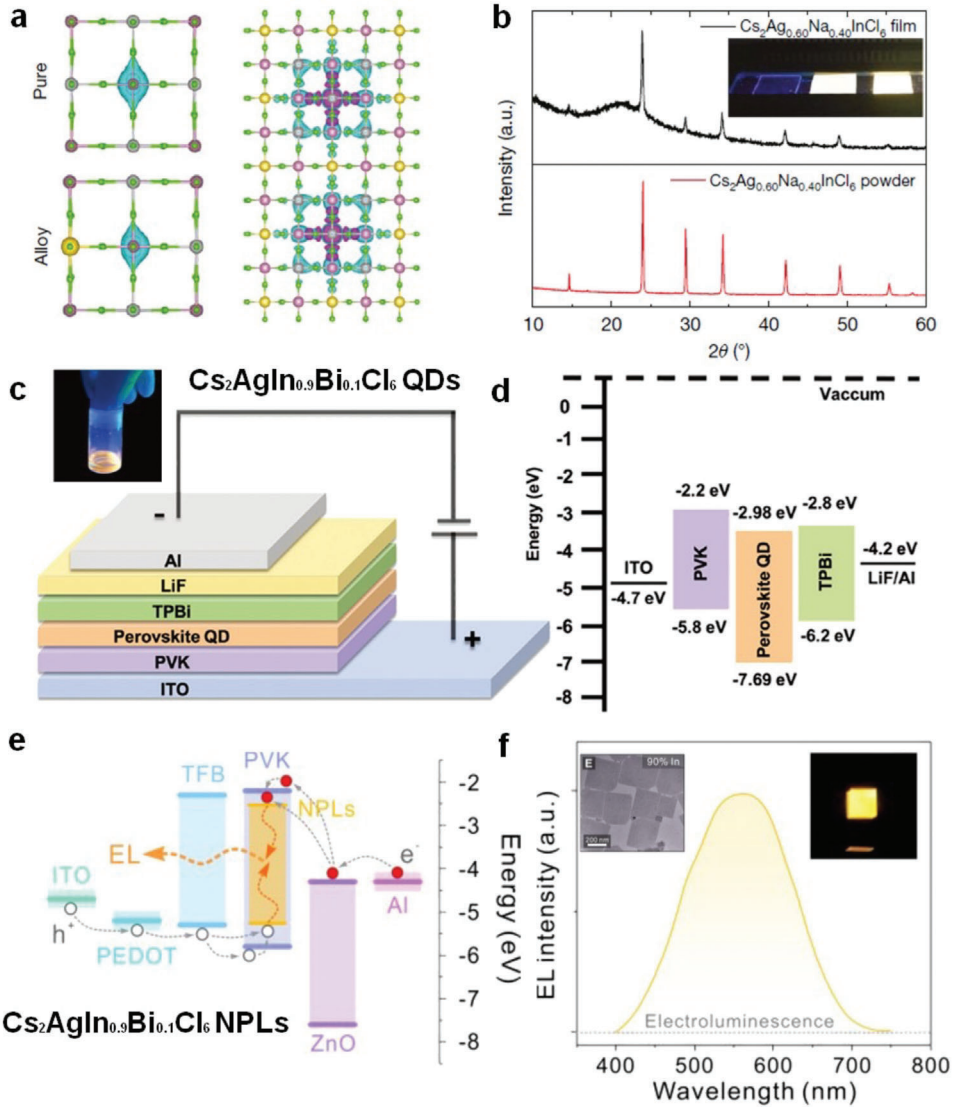

Figure 21. a) Strengthened STE confinement by the surrounding $AgCl_6^{5-}$ octahedra. Reproduced with permission.[92] Copyright 2018, Springer Nature. b) XRD patterns of a $Cs_2Ag_{0.60}Na_{0.40}InCl_6$ film (black line) and powder (red line). The inset shows a 300-nm thick quartz substrate and 500-nm-thick $Cs_2Ag_{0.60}Na_{0.40}InCl_6$ films under 254 nm ultraviolet illumination. c,d) $Cs_2AgIn_{0.9}Bi_{0.1}Cl_6$ QDs based electroluminescence device, including the device structure, energy band diagram of the $Cs_2AgIn_{0.9}Bi_{0.1}Cl_6$ QDs based WLED device. Reproduced under the terms of CC BY 4.0.[328] Copyright 2022, The Authors, published by Wiley-VCH. e) Band alignments and proposed charge carrier transfer processes of the NPL-LED; f) Electroluminescence (EL) spectrum of the LED. Reprinted with permission.[329] Copyright 2023, Wiley-VCH.

systems, it is most likely that the emission comes from isolated $SbCl_6$ octahedra.[95] Furthermore, doping with manganese ions can alter the spectrum toward the red emission. The dopants can also alter the emission color. Zhang et al. fabricated down-conversion LEDs based on 3% Mn^{2+}-doped $Cs_2NaTbCl_6$, the orange color spectra showed excellent spectral stability at different voltages and currents applied to the blue LED chip. (Figure 22b).[331] The orange LED exhibited bright PL with CIE of (0.579, 0.352) and CCT of 2547 K. In many DP systems, Mn^{2+}-doping can result in white light emission as discussed above. For example, Mn^{2+}-doped $Cs_2Na_{0.4}Ag_{0.6}In_{0.95}Bi_{0.05}Cl_6$ emits white PL with a maximum PLQY of 31.8% and two emission maxima that are at 550 and 610 nm.[332] The corresponding Commission International de L'Eclairage (CIE) coordinates, emission color temperature, and CRI are (0.3784, 0.4216), 4323.4 K, and 82.6, respectively (Figure 22c). To obtain low CCT and high CRI WLEDs, $Cs_2AgIn_{1-x}Bi_xCl_6$ was used as an emitter by combining it with a 400 nm UV LED chip (Figure 22d).[333] This resulted in efficient, broad, yellow-white PL (CRI = 85, CCT = 3119 K). These metrics meet the standard for warm white lighting with high color rendering abilities.

The emission from most DP materials originates from the radiative recombination of STE species. Thus, they exhibit broad emission with large Stokes shift, making them suitable for WLEDs. Another strategy to tune the emission of the DPs is by

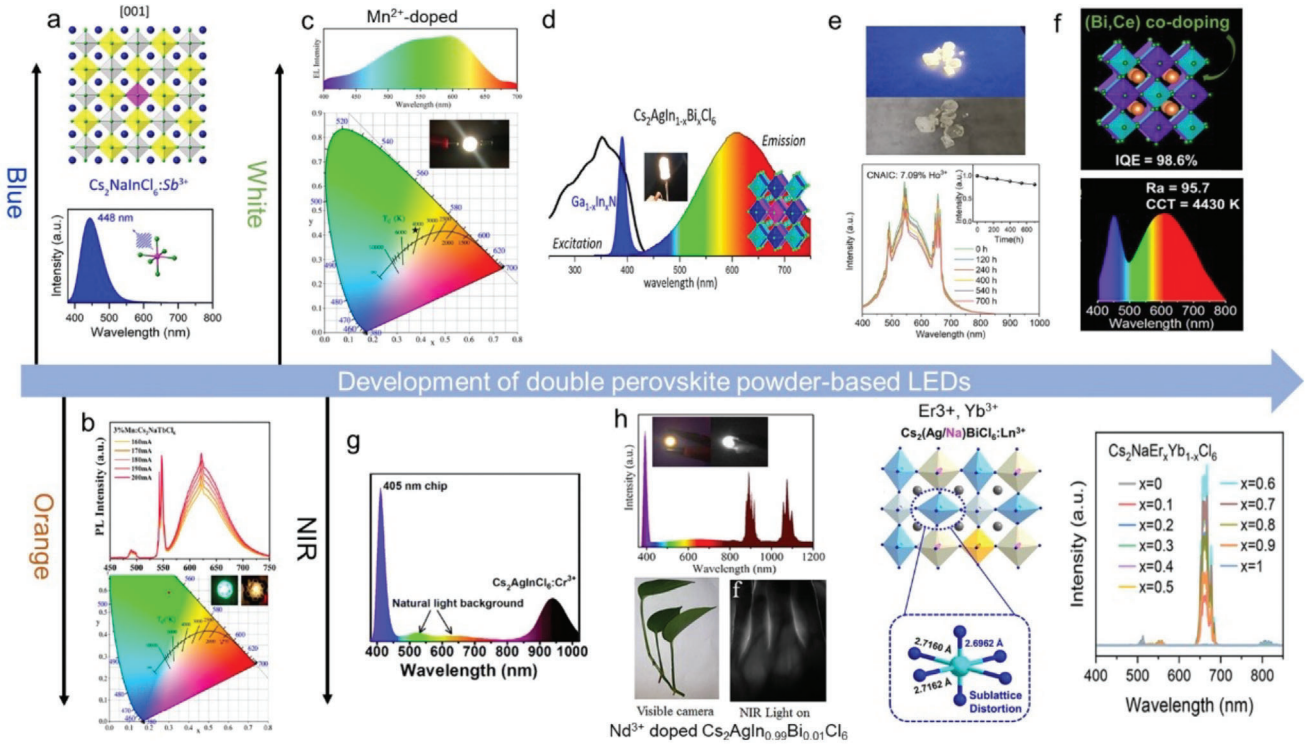

Figure 22. Different DP phosphors that were coated on an ultraviolet chip for the fabrication of down-conversion LED that emits blue, red, and broad white light emission and narrow infrared radiation. a) $Cs_2NaInCl_6:Sb^{3+}$ DPs. Reproduced with permission.[330] Copyright 2022, American Chemical Society. b) 3% Mn^{2+}-doped $Cs_2NaTbCl_6$. Reprroducedd with permission.[331] Copyright 2022, American Chemical Society. c) Mn^{2+}-doped $Cs_2Na_{0.4}Ag_{0.6}In_{0.95}Bi_{0.05}Cl_6$. Reproduced with permission.[332] Copyright 2019, Optical Society of America. d) Broadband White Emission in $Cs_2AgIn_{1-x}Bi_xCl_6$ Phosphors. Reprroduced with permission.[333] Copyright 2019, American Chemical Society. e) Ho^{3+}-doped $Cs_2(Ag,Na)InCl_6$ DPs. Reproduced with permission.[335] Copyright 2019, Wiley-VCH. f) (Bi,Ce)-codoped $Cs_2Ag_{0.4}Na_{0.6}InCl_6$. Reprroduced with permission.[338] Copyright 2020, American Chemical Society. g) $Cs_2AgIn_{0.9}Cl_6{:}_{0.1}Cr^{3+}$.Reproduced.[343] Copyright 2022 American Chemical Society. h) Nd^{3+} doped $Cs_2AgIn_{0.99}Bi_{0.01}Cl_6$, $Cs_2NaEr_{0.4}Yb_{0.6}Cl_6$, and Yb^{3+} and Er^{3+} doped $Cs_2Ag_{0.2}Na_{0.8}BiCl_6$.The panel h is adapted with permission.[344–346] Copyright 2022, American Chemical Society; Copyright 2022, Wiley-VCH.

doping with lanthanides.[334] For example, Ho^{3+}-doped $Cs_2(Ag,Na)InCl_6$ DPs exhibit bright warm-white emission with peaks at 490, 450, and 650 nm (Figure 22e).[335] The doped sample exhibited an improvement of CRI from 70.3 to 75.4 as compared to pristine $Cs_2(Ag,Na)InCl_6$. On the other hand, the emission color is also tunable by doping different metal ions with a controllable ratio. For instance, by controlling Tb^{3+} co-dopant concentration, the emission color of Bi-doped $Cs_2Ag(In_{1-x}Tb_x)Cl_6$ NCs could be continuously tuned from green to orange, through the efficient energy-transfer channel from STE to Tb^{3+} ions.[336] Similarly, co-doping Dy^{3+}, Sm^{3+}, and Tb^{3+} ions into $Cs_2AgInCl_6$ NCs results in tunable emission from green to yellow-orange by varying the relative dopant concentration. The concept of change in emission color by co-doping can be used to obtain fluorescent patterns by spray coating the DP NC inks for anti-counterfeiting technology.[337] In addition, Wei et al. proposed a codoping (Bi, Ce) strategy to enhance the quantum efficiency of orange-emitting $Cs_2Ag_{0.4}Na_{0.6}InCl_6$:Bi.[338] As shown in Figure 22f, by combining the (Bi,Ce)-codoped sample with a blue $BaMgAl_{10}O_{17}:Eu^{2+}$ phosphor, a white light-emitting diode with an excellent color rendering index of 95.7 and a correlated color temperature of 4430 K can be achieved. Deng and coworkers demonstrated that (Bi,Gd)-codoped $Cs_2Ag_{0.4}Na_{0.6}InCl_6$ phosphors are efficient for white LEDs when combined with blue phosphor $BaMgAl_{10}O_{17}:Eu^{2+}$.[339] The corresponding warm white LEDs showed color coordinates of (0.3464, 0.3224), a colour rendering index of 93.9 and colour temperature of 4818 K. However, there are no single-matrix phosphors that rely on commercial blue phosphors. Although the CRI of DPs is relatively high, their color temperature is also very high, which is not conducive for daily lighting applications.

For practical applications, it is necessary to further improve the operational stability of DPs. A few attempts have been made towards improving the operational stability of DP-LEDs. For instance, Li *et. al* constructed WLED devices by combining $Cs_2Ag_{0.7}Na_{0.3}InCl_6$:Bi with a commercial UV-emissive LED chip (370 nm).[340] The resulting WLED showed CIE color coordinates of (0.38, 0.44), a CCT of 4347 K, and a high CRI of 87.8 with excellent working stability and a record lifetime above 1000 h. Similarly, Zeng et al. synthesized $Cs_2AgScCl_6$:0.05Bi emitting white light and with high stability against thermal and UV radiation.[341] Furthermore, a series of $Cs_2Na_xAg_{1-x}InCl_6$: Bi (x = 0, 0.2, 0.4, 0.6, 0.8, and 1) DP microcrystals were synthesized by a solvent-free melting-crystallization technique.[342] The optimized $Cs_2Na_{0.4}Ag_{0.6}InCl_6$: Bi microcrystal phosphors were combined with commercial blue and green phosphors and coated on

Table 7. Performance summary of the powder-based WLEDs.

Device structure	PLQY [%]	CIE (*x*, *y*)	CCT [K]	CRI	Reference
UV LED/$Cs_2AgIn_{0.7}Bi_{0.3}Cl_6$ NCs/PMMA	4	(0.36, 0.35)	4443	91	[102]
UV LED/$Cs_2NaInCl_6$:2.5%Sb,45%Tb,3%Mn NCs	74	(0.41, 0.39)	3371	89.2	[279]
UV LED/Cs_2(Na, Ag)$InCl_6$:7.09%Ho^{3+}	57.09	(0.39, 0.46)	N/A	75.4	[335]
UV LED/$Cs_2Na_{0.4}Ag_{0.6}In_{0.95}Bi_{0.05}Cl_6$:$Mn^{2+}$	31.8	(0.3784, 0.4216)	4323.4	82.6	[332]
UV LED/$Cs_2AgIn_{1-x}Bi_xCl_6$	39	(0.417, 0.391)	3119	85	[333]
UV LED/$Cs_2Ag_{0.4}Na_{0.6}InCl_6$:1% Bi,1%/ $BaMgAl_{10}O_{17}$:Eu^{2+}	98.6	(0.4, 0.38)	4430	95.7	[339]
UV LED/$Cs_2Ag_{0.4}Na_{0.6}InCl_6$: Bi,Gd/ $BaMgAl_{10}O_{17}$:Eu^{2+}	87.57	(0.3464, 0.3224)	4818	93.9	[339]
UV LED/$Cs_2Ag_{0.7}Na_{0.3}InCl_6$:Bi	87.2	(0.38, 0.44)	4347	87.8	[340]
UV LED/$Cs_2AgScCl_6$:0.05Bi	60	(0.366, 0.367)	4100	96	[331]
UV LED/$Cs_2Na_{0.4}Ag_{0.6}InCl_6$: Bi	73.3	(0.461, 0.443)	2930- 6957	84.8-97.1	[342]

ultraviolet chips (365 nm) to fabricate WLEDs. The emission was tunable from warm white (2930 K) to cold white (6957 K). **Table 7** provides a summary of the performance of selected DP powder-based WLEDs.

NIR light sources with broad coverage have drawn a special interest in optical communication, night vision technology, food analysis, health monitoring, and bio-imaging/bio-sensing. In early studies, rare earth ions were used as activators in LHPs to obtain the NIR luminescence, and later they were extended to DP systems. In 2019, Liu et al. reported $Cs_2AgInCl_6$:Cr^{3+} via the traditional high-temperature solid-state reaction.[347] The sample ($Cs_2AgIn_{0.9}Cl_6$:$_{0.1}Cr^{3+}$) emits broad NIR emission with a PLQY of ~22.03% upon 760 nm excitation (Figure 22g). Inspired by this, Cr^{3+}-doped $Cs_2AgInCl_6$ NCs were synthesized via hot-injection synthesis, and the sample exhibited tunable emission from 998 to 958 nm by gradually substituting Ag^+ with Na^+.[343] The excellent chemical and moisture stability of the sample enabled the fabrication of $Cs_2NaInCl_6$:Cr^{3+} NC films by screen printing and thus showcases its potential application in high-resolution images and NIR fluorescent signs. Recently, several reports have been published on lanthanide ion-doped NIR LEDs, such as Nd^{3+} doped $Cs_2AgIn_{0.99}Bi_{0.01}Cl_6$, $Cs_2NaEr_{0.4}Yb_{0.6}Cl_6$, and Yb^{3+} and Er^{3+} doped $Cs_2Ag_{0.2}Na_{0.8}BiCl_6$ (Figure 22h).[344–346] These NIR LEDs have demonstrated good night vision and human tissue penetration. Most notably, Wang et al. reported Na^+-doped bismuth halide perovskite $Cs_2AgBiCl_6$ crystals to replace the traditional Cr^{3+}-doped systems.[348] It was proposed that the incorporation of Na ions weakens the coupling between $[AgCl_6]^{5-}$ octahedrons and confines the spatial distribution of the STE state around $[AgCl_6]^{5-}$ and $[BiCl_6]^{3-}$. This leads to enhanced overlap of electron and hole orbitals, leading to enhanced NIR emission from STE states.[110,86]

In summary, there has been certainly progress in the field of DP-LEDs, especially WLEDs based on doped DPs. However, there are several significant challenges that need to be overcome for the realization of electric-driven LEDs based on DPs. The quality of thin films could be improved by thermal evaporation methods, but precise control over the composition is critical. In the case of NC LEDs, colloidal DP NCs with high PLQY (both in solution and solid-state) need to be developed. The most critical factor that hinders efficiency is the large bandgap of double perovskites. Hence, the bandgap of DPs must be optimized by compositional engineering or by combining them with other material systems. As demonstrated above, metal ion doping is imperative to improve the properties of DPs by breaking off forbidden transitions, and increasing their radiative transition rates, and simultaneously boosting the energy transfer efficiency. Therefore, there are numerous lead-free perovskite compositions that emit light in the visible to short-wave infrared ranges. The early results demonstrate the potential of DP-based powders for down-conversion LEDs. A better understanding of charge-injection, transport, and recombination in DPs would help to improve the efficiency of electrically driven DP-LEDs.

4.3. Radiation Detectors using Pb-free Perovskites

Photodetectors (PDs) are devices that convert incoming photons into electrical signals. They find numerous applications in various fields, including research, security, industry, and medical imaging.[349] It is important to develop materials that can detect photons of low intensity, especially to detect X-ray radiation as it is being extensively used in medical imaging and diagnostics. This is because high X-ray doses can increase the risk of cancer due to DNA damage. Therefore, materials characterized by a lower detection limit (LoD) are crucial for safer medical imaging allowing for lower radiation doses.[350] All PDs involve three key processes: i) photon absorption, ii) charge carrier generation, and iii) collection. Furthermore, ease of synthesis and material stability are mandatory for industrial production (iv). HPs are a class of semiconductors possessing optimal properties to excel in these processes and the ease of production as well. i) They exhibit strong photon absorption coefficients, especially for high-energy radiation such as X-rays, where the heavier elements (e.g., Cs^+, Pb^{2+}, I^-) are the main ones responsible for the high attenuation coefficient. Moreover, by varying their composition, the HPs' bandgap (E_g), hence their absorption range, can be largely tuned. This tunability aids efficiency (ii). Especially for high-energy detection, charge carrier generation depends on E_g. Moreover, the charge carrier mobility can be substantially enhanced while reducing the charge trap density (iii). They can be produced using low-temperature solution methods and cheap constituents, making them cost-effective and easily scalable, in contrast to the commercially standard direct X-ray- PDs for which the

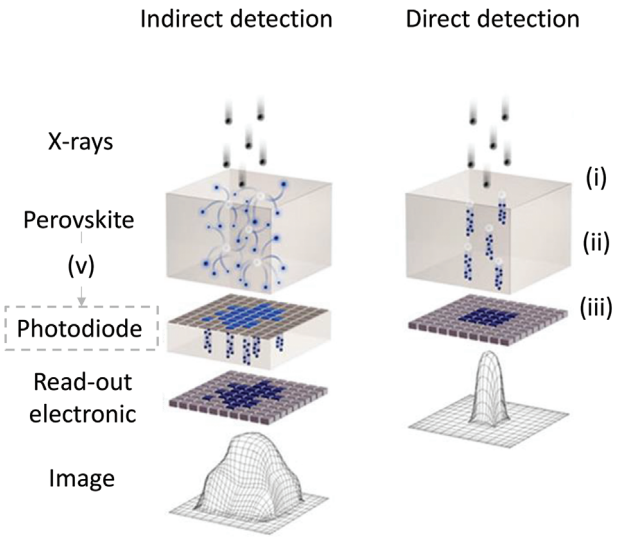

Figure 23. Schematic representation of indirect and direct X-ray detection. In the indirect modality, the absorbed X-rays are converted to lower energy photons (v), and their collection by a photodiode result in an electrical signal. The presence of (v) will eventually result in lower image resolution. Reproduced under the terms of CC-BY-3.0 and CC-BY-ND-3.0.[352] Copyright 2016, The Authors, published by NDT.net.

production of the photoactive material (e.g., CdZnTe and CdTe) is cumbersome and expensive. HPs can be used to detect X-rays via direct or indirect methods (the latter mainly by means of elpasolite halide single crystals),[351] as illustrated in **Figure 23**. Yet, the most popular LHPs contain toxic lead and exhibit relatively low stability (as compared with commercial materials) under ambient conditions. Consequently, research interest has moved towards the development of Pb-free perovskites, such as Sn-based HPs and DPs. In this section, we will focus on these two groups of HP materials, highlighting their properties, performance, and potential application as PDs. For a summary including the materials' figures of merit (together with operating wavelengths) in the PD field, we refer our readers to **Figures 24–26**. It must be noted that the measurements and calculations of noise equivalent power (NEP), are necessary to assess the specific detectivity (D), depending on different types of noises affecting the PD. Therefore, different reports may consider different noise sources, leading to over- or under-estimation of D.

Waleed et al. were the first to report the use of an THP ($MASnI_3$) as active material in a PD. They fabricated perovskite NWs arrays inside a porous alumina template. The corresponding PD exhibited a responsivity (R) and specific detectivity of 0.47 A/W and 8.80×10^{10} Jones, respectively, and rise and decay times (τ_r and τ_d) of 1500 and 400 ms.[353] However, the NW-based PD showed a photocurrent decrease after only one week at 70% relative humidity, although its stability was almost three orders of magnitude higher than the plain thin film (TF) counterpart.[353] The same concept, NWs-based photodetection, was replicated by Han et al. who prepared the all-inorganic equivalents $CsSnX_3$ (X = Cl, Br, and I). Among the different compositions, $CsSnI_3$ showed the best results in the NIR range, as expected from its E_g. The $CsSnI_3$ device exhibited an R and D of 54 mA/W and 3.85×10^5 Jones, respectively (940 nm), with a rather fast τ_r (83.8 ms) and τ_d (243.4 ms). However, also in this case, the sample degraded after six days even with a protective layer.[82] To overcome this instability issue related to THPs, Liu et al. developed an air-stable $FASnI_3$ using hydroxybenzene sulfonic acid and an excess of $SnCl_2$ as an additive. By applying this approach, they produced a very thin THP film (120 nm), which showed a high R of 1.1×10^5 A W^{-1} (@ 685 nm), which was attributed to the high hole density and mobility (p-type semiconductor). The device also demonstrated a response to 420 and 850 nm light illumination and high bending stability when $FASnI_3$ was deposited on a flexible substrate. However, relatively low values of τ_r and τ_d (31 and 120 s, respectively) were recorded.[354] With a similar approach, Cao et al. tried to address the THPs instability issue by using SnF_2 and ascorbic acid as additives to reduce the Sn^{2+} to Sn^{4+} oxidation. The resulting device showed a broad (350–1000 nm) and relatively fast (τ_r/τ_d of 0.35/1.6 ms) response. Moreover, the device remained stable in the air with approximately 80% humidity for more than one day.[355] Together with increasing the ambient stability, scientific attention has been given to device optimization as well. Liu et al. reported a PD based on a vertical heterojunction consisting of $FASnI_3$ and PEDOT:PSS. Because of the resulting photogate effect, the device exhibited a maximum R of 2.6×10^6 A W^{-1} (the highest reported for THPs) and D of 3.2×10^{12} Jones with a broadband photoresponse from UV to NIR. Moreover, a flexible device made of a polyimide layer showed a high photoresponse as well.[356] Lastly, Howlader et al. improved the performance by morphology engineering via chlorobenzene-treated $CsSnI_3$ TFs and coupling with carbon nanotubes. The resulting device exhibited an R of 10^{-2} A W^{-1}.[357] It must be noted that by slightly modifying the $ASnX_3$ unit formula toward lower-dimensional perovskites, the THPs stability can be further enhanced, while still maintaining a good photoresponse.[358–360]

Considering THPs, it is interesting to observe that the performances offered by these materials closely approach, and sometimes surpass, the ones of commercially available Si-PDs characterized by an $R(\lambda) \approx 0.5$ A W^{-1} and $D \approx 3 \times 10^{12}$ Jones.[361] However, even though the THPs have emerged as a promising alternative to the traditional LHPs, the use of Sn^{2+} comes with a challenge as it is prone to oxidation to Sn^{4+}, making it challenging to fabricate THPs with long-term stability using easy solution processes. Nonetheless, despite their slightly inferior optoelectronic properties and indirect bandgap, DPs can provide a more stable alternative to both LHPs and THPs, while still demonstrating a competitive photoresponse over a broad wavelength range.

Lei et al. were the first to report a PD based on a $Cs_2AgBiBr_6$ TF.[362] Their film, made from an easy one-step spin-coating procedure, showed an R of 7.01 A W^{-1} (520 nm), an on/off ratio of 2.16×10^4, D of 5.66×10^{11} Jones and τ_r/τ_d of 956/995 µs. Although these values are comparable to those of Sn-based PDs, the most significant difference is that a $Cs_2AgBiBr_6$ -based PD, even without encapsulation, demonstrated remarkable stability during aging tests (36 hours of continuous operation and exposure to ambient conditions) with almost no loss in photodetection performance. Ever since, various research groups have investigated the possible use of $Cs_2AgBiBr_6$ TFs as PDs and their long-term stability. For instance, Xiu et al. used a capillary-assisted dip-coating method to obtain a "large-area" coverage with $Cs_2AgBiBr_6$ achieving an on/off ratio of 7.[363] Wu et al. demonstrated the possibility of self-powered photodetection through a heterojunction made of

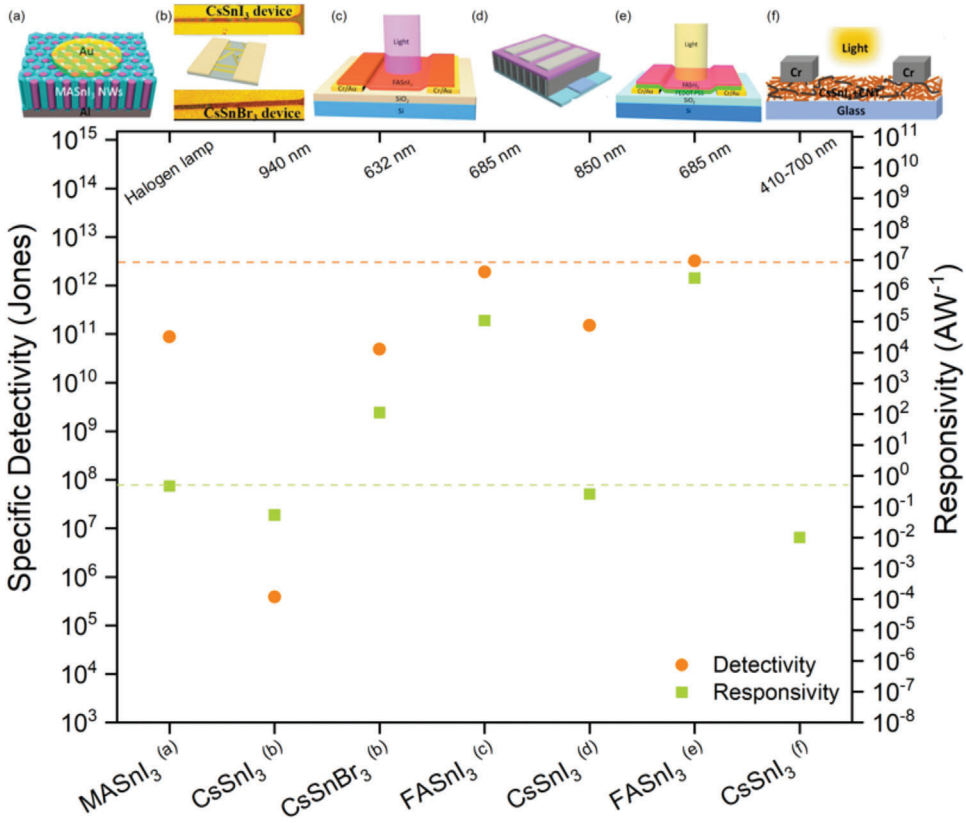

Figure 24. Figures of merit (D in orange and R in green) for different THP PD compositions and typical device structures (top insets). The THP PD values have been compared to Si-PDs' average performances (dotted lines).[361] a) Reproduced with permission.[353] Copyright 2017, American Chemical Society. b) Reproduced with permission.[82] Copyright 2019, American Chemical Society. c) Reproduced with permission.[354] Copyright 2019, WILEY-VCH Verlag GmbH & Co. KGaA, Weinheim. d) Reproduced with permission.[355] Copyright 2020, John Wiley & Sons Australia, Ltd on behalf of UESTC. e) Reproduced with permission.[356] Copyright 2020, American Chemical Society. f) Reproduced with permission.[357] Copyright 2022, Springer Nature.

$Cs_2AgBiBr_6$ /SnO_2. Their planar device worked as a blue or UV-A light detector without requiring any external bias.[364] On the same note, Li et al. created a self-powered PD relying on a favorable band alignment between $Cs_2AgBiBr_6$ and GaN.[365] Shifting to TF morphology engineering, Yang et al. achieved large grain sizes of ≈1 µm by adding a small amount of DMF to the DMSO precursor solution,[366] while Yan et al. suppressed the formation of pinholes and optimized the CABB layer grain size using ultrathin atomic layer deposition of a metal-oxide layer (e.g., NiO_x) on an FTO substrate.[367] The resulting photodetector showed improved performance compared to the non-optimized substrate device, with a promising weak-light detection capability with a limit of detection as low as 1.9×10^{-9} W cm^{-2}, a high D of 1.2×10^{13} Jones (surpassing previous reports), and an increased linear-detection-range (LDR) of 165.2 dB. Moreover, in a later report, they demonstrated that interfacial engineering with the HTL material CuSCN enhances the photoresponse as well.[368] Lastly, Fang et al. further reduced the thickness of the $Cs_2AgBiBr_6$ layer. The resulting nanoflakes- (around 5 nm thick) based PD achieved an R of 54.6 A W^{-1}, on/off ratio of 7.4×10^4, D of 7.4×10^{14} Jones, and response times of 1.7 ms.[369] Nevertheless, these very promising values are limited by the nanoflakes' lateral length (50 µm), which hampers the possibility to fabricate large-area ultrathin film devices.

Moving to a bigger scale, $Cs_2AgBiBr_6$ single crystals (SCs) were used for X-ray and visible light detection by Pan et al. Focusing on visible light, they achieved high values of R, reaching 15.0 A W^{-1}, and a D of 1.60×10^{13} Jones (530 nm).[370] These values were possible due to enhanced charge-carrier transport, i.e., low trap density, high mobility-lifetime product, and high resistivity resulting from thermal annealing and surface treatment steps. Later, by optimizing the process of controlled cooling of a super-saturated solution (SSCC), Yin et al. were able to improve $Cs_2AgBiBr_6$ (opto)electronic properties and obtained a high R of 113.29 A W^{-1} (530 nm).[371] In parallel, Dang et al. reported a modified seed-growth SSCC resulting in high-quality SCs.[372]

The possibility of producing NIR PDs from $Cs_2AgBiBr_6$ has been demonstrated by several studies. Ji et al. used Cu-doping to shift the absorption edges of $Cs_2AgBiBr_6$ to the NIR range (≈860 nm) due to the formation of sub-bandgap states.[375] Liu et al. further lowered the band-edge to 1350 nm by Fe-doping, and the PD exhibited an on/off ratio higher than 10 (808, 980 nm),[376] while Zhang et al. proved that Ru doping allows NIR photodetection as well.[377] These approaches extended the absorption range of the DPs close to the Sn-iodide-based ones while retaining a stable photoresponse over several months compared to the few days or weeks of the Sn-based counterparts.[364,365]

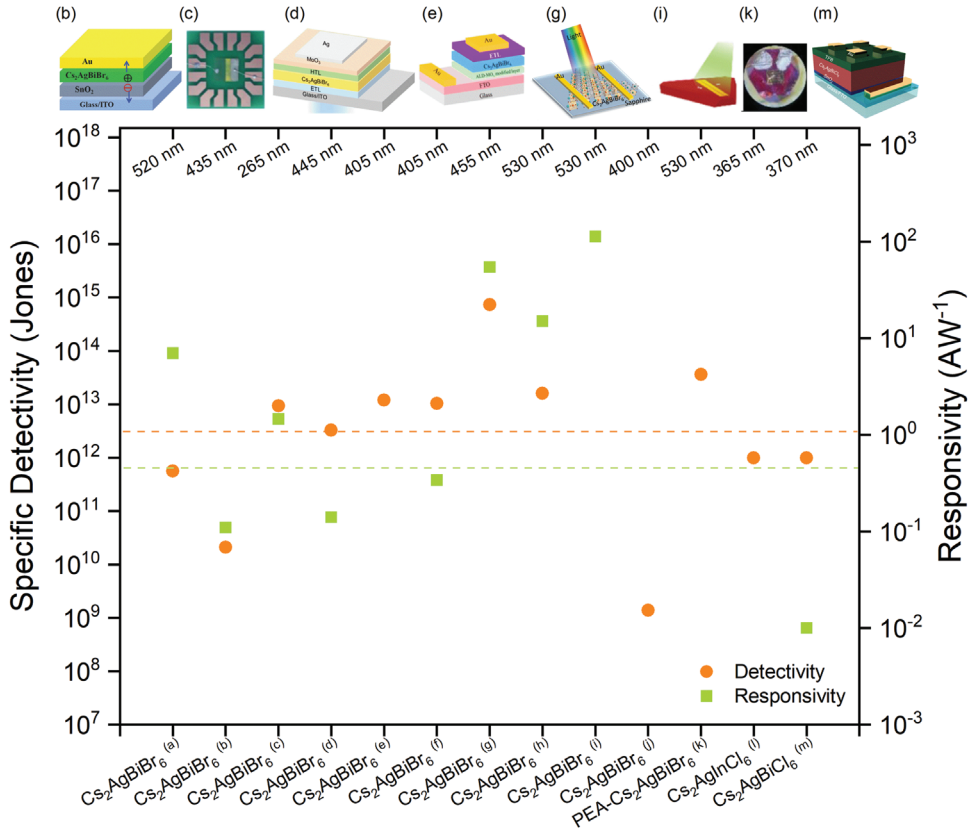

Figure 25. Figures of merit (D in orange and R in green) for different DP PD compositions and typical device structures (top insets) in the UV-Visible range. The DP PD values have been compared to Si-PDs' average performances (dotted lines). a) Data reported from ref. [362]. b) Reproduced with permission.[364] Copyright 2018, WILEY-VCH Verlag GmbH & Co. KGaA, Weinheim. c) Reproduced with permission.[365] Copyright 2019, WILEY-VCH Verlag GmbH & Co. KGaA, Weinheim. d) Reproduced with permission.[366] Copyright 2019, WILEY-VCH Verlag GmbH & Co. KGaA, Weinheim. e) Reproduced with permission.[367] Copyright 2020, American Chemical Society. f) Data reported from ref. [368]. g) Reproduced with permission.[369] Copyright 2021, Wiley-VCH GmbH. h) Data reported from ref. [370]. i) Reproduced with permission.[371] Copyright 2019, WILEY-VCH Verlag GmbH & Co. KGaA, Weinheim. j) Data reported from ref. [372]. k) Reproduced with permission.[373] Copyright 2019, WILEY-VCH Verlag GmbH & Co. KGaA, Weinheim. l) Data reported from ref. [240]. m) Reproduced with permission.[374] 2020, WILEY-VCH Verlag GmbH & Co. KGaA, Weinheim.

However, the efficiency of the DP-PD for the NIR range is still lagging.

It is important to mention that for X-ray PDs based on Pb-free HPs, most of the reports rely on a photoconductor device structure (i.e., Metal/HPs/Metal). In contrast, LHPs-based PDs are implemented in photodiode devices (e.g., p-i-n junction) resulting in self-powered PDs, offering a more efficient control of the device characteristics, and also reducing photoconductive gain. As previously mentioned, Pan et al. demonstrated the possible use of $Cs_2AgBiBr_6$ for X-ray detection and Murgulov et al. recently elaborated on this approach.[370,378] In their seminal paper, they reported for a vertical Au/ $Cs_2AgBiBr_6$/Au device a sensitivity (S) up to 105 μC $Gy_{air}^{-1}cm^{-2}$ with a LOD of 59.7 nGy_{air} s^{-1} and long-term operational stability. Similar post-treatment processes were also reported by Zhang et al.[379] Importantly, these treatment procedures suppress ion migration and reduce surface conduction channels, hence reducing noise in a device configuration. It is interesting to note that the sensitivity can be further improved by lowering the operating temperature as demonstrated by Steele et al. by cooling the SC CABB device from room temperature (316 μC $Gy_{air}^{-1}cm^{-2}$) to 100 K (988 μC $Gy_{air}^{-1}cm^{-2}$).[380] A reason for this behavior is that parasitic recombination pathways are reduced at low temperatures. Later, Yin et al. optimized the SSCC process to produce a PD with a very high S of 1974 μC Gy_{air}^{-1} cm^{-2}, which is the highest reported value for SC CABB devices up to now.[371] In addition, also the LoD reached the lowest value of 45.7 nGy_{air} s^{-1}. Another approach to improve the SC device performance is to impart ordering at the level of the $[AgX_6]^{5-}$ and $[BiX_6]^{3-}$ inorganic sublattice, which can be achieved by replacing a certain amount of Cs^+ with phenylethylammonium as demonstrated by Yuan et al.[373], while by means of partly substituting Cs^+ with alkali metals (Na^+, K^+, and Rb^+), the X-ray sensitivity of the Rb-doped device increased by 4.5 times.[381]

Proven the high efficiency of $Cs_2AgBiBr_6$ for X-ray detection, a straightforward method for implementing this material into a large-area device was still needed. Potential approaches include the realization of compact and uniform (composite) thick films. In this frame, Li et al. proposed a flexible poly(vinyl alcohol)/$Cs_2AgBiBr_6$ (100 μm-thick) heterostructure showing a sensitivity of 40 μC Gy_{air}^{-1} cm^{-2} at the rather high bias of 400 V.[382] To further improve large-area scalability, Yang et al. fabricated a wafer of CABB with suppressed ion migration thanks to heteroepitaxial passivation with BiOBr.[383] When used as

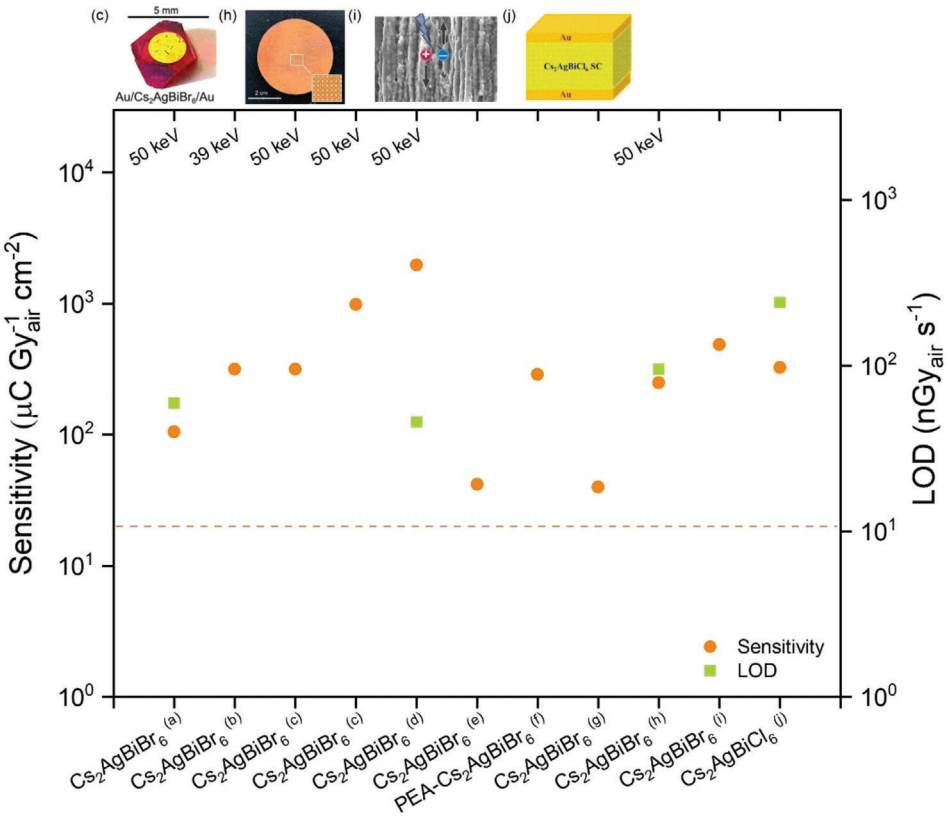

Figure 26. Figures of merit (S in orange and LOD in green) for different DP PD compositions and typical device structures (top insets) under X-ray irradiation. The DP PD S values have been compared to a-Se flat panel detectors, which represent the market gold standard X-ray direct conversion PDs. a,b) Data reported from ref. [370,379]. c) Reproduced with permission.[380] Copyright 2018, WILEY-VCH Verlag GmbH & Co. KGaA, Weinheim. h) Reproduced with permission.[383] Copyrigt 2019, Springer Nature. d–g) Data reported from ref. [371,373,378,382]. i) Reproduced with permission.[384] Copyright 2021, American Chemical Society. j) Reproduced with permission.[385] Copyright 2022, American Chemical Society.

X-ray PD, a high S of 250 μC Gy_{air}^{-1} cm^{-2} was reached, which is around ten times higher than that of a-Se X-ray detectors (20 μC Gy_{air}^{-1} cm^{-2}), operating at a much higher electric field of (10 $V\mu m^{-1}$), and even higher than the first $Cs_2AgBiBr_6$ SC-based device by Pan et al. However, the measured LoD (95.3 nGy_{air} s^{-1}) was slightly worse. A recent report from Haruta et al. introduced columnar grain grown- $Cs_2AgBiBr_6$ by means of mist deposition. The columnar grain structure offers easy integration with the readout electronics and a low density of grain boundaries across the direction of the charge-carrier collection.[384] The X-ray detector (92 μm-thick films) showed a high S of 487 μC Gy_{air}^{-1} cm^{-2}.

The detection range of $Cs_2AgBiBr_6$ can be further extended to gamma-rays. Zhang et al. have grown $Cs_2AgBiBr_6$ from Bi-poor precursor solutions to suppress deep electron trap formation. The resulting detector showed a response to 59.5 keV gamma-rays with an energy resolution of 13.91% (^{241}Am), while a $Cs_2AgBiBr_6$ SC grown following the regular procedure did not show any response.[386] Responses to higher energy gamma-photons (511 keV ^{22}Na and 662 keV ^{137}Cs sources) were also obtained.

The photodetection capabilities of DP materials are not limited to the $Cs_2AgBiBr_6$ composition. $Cs_2AgInCl_6$ can be used as a UV-PD[240] as reported by Luo et al. showing an on/off ratio of ≈500, D of 10^{12} Jones, and a low dark current of ≈10 pA. Furthermore, Wang et al. demonstrated the viability of $Cs_2AgBiCl_6$ TFs for UV-light detection as well. The device exhibited an R ≈10 mA/W and D of $\approx 10^{12}$ Jones.[374] In the X-ray range, Tailor et al. reached an X-ray sensitivity of 325.78 μC Gy^{-1} cm^{-2} and LoD of 241 nGy s^{-1} with the same composition. It must be noted that the device can also work self-powered, but with a way lower S.[385] As expected, all the mentioned compositions were highly stable.

In summary, Pb-free HPs have shown promising results for broad-range radiation detection, spanning from NIR to gamma-rays. Although long-term stability is still a concern for THPs, various strategies such as additive mixing[82], encapsulation[353], thin film engineering[357], amongst others, have been proposed.[358–360] Another potential solution is to apply DPs, which possess a higher inherent stability. However, DPs' best-performing composition, $Cs_2AgBiBr_6$, exhibits a higher bandgap than THPs, particularly iodide-based ones, which limits its detection range. Nonetheless, doping of $Cs_2AgBiBr_6$ can shift the band edge to the NIR region, making this material a preferred option for broad-range photodetection.[80,375–377] Additionally, various methods such as post-treatment,[370,379] doping,[381] synthesis,[371,387] and device engineering[364,368] have been reported to improve the DPs' properties as well and even allow sensing at low light intensities and X-ray doses. Of particular

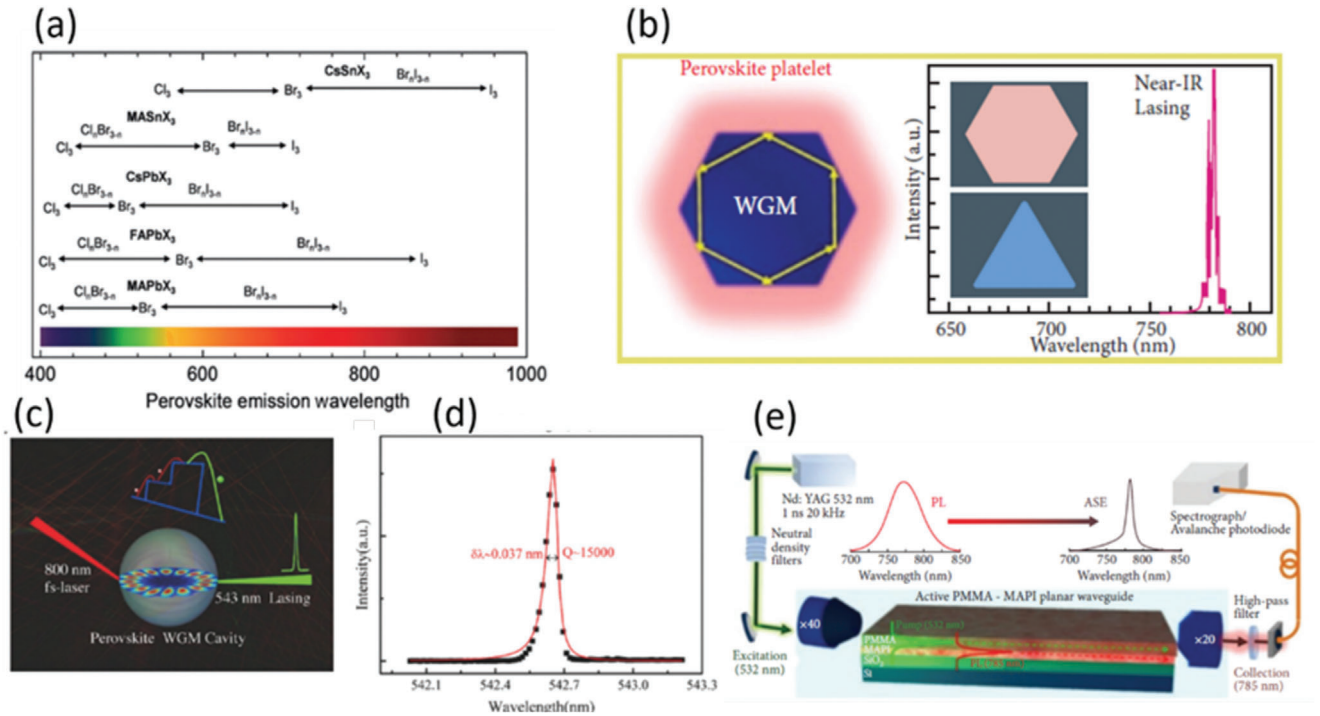

Figure 27. a) Schematics of the bandgaps of $MAPbX_3$, $FAPbX_3$, $CsPbX_3$, $MASnX_3$, and $CsSnX_3$. Reproduced with permission.[400] Copyright 2017, WILEY-VCH Verlag GmbH & Co. KGaA, Weinheim. b) Whispering gallery modes in a perovskite nanoplatelet. Reproduced with permission.[408] Copyright 2014, American Chemical Society. c) Schematic of an individual CsPbBr3 microsphere pumped by 800 nm laser excitation (≈40 fs, 10 kHz). d) Lorentz fitting of a lasing oscillation mode at 542.6 nm, giving an ultrasmall linewidth of ≈0.037 nm, corresponding to an ultrahigh Q factor ≈1.5×10^4. Reproduced with permission.[103] Copyright 2018, WILEY-VCH Verlag GmbH & Co. KGaA, Weinheim. e) Waveguide architecture where the pump beam is end-fire coupled from the input edge of the structure. Reproduced with permission.[409] Copyright 2020, American Physical Society.

interest, as the detection limit is lowered to a few tens of $nGy_{air}s^{-1}$ lower X-ray dose rates will be sufficient for imaging, thus reducing the risks of radiation damage. Potential innovations for future research activities are suggested to offer enhanced sensitivity at the low-energy spectral range, polarization-selective sensing, and scintillation radiation detectors. These aspects have already been demonstrated, but further investigation is still necessary.[351,388–393]

5. Pb-Free Perovskite Lasers

Halide perovskites (HPs) have emerged as excellent direct bandgap semiconductor materials due to their interesting properties such as sharp optical absorption edge, high absorption coefficient exceeding 10^4 cm^{-1} just above the band edge, defect tolerance, and high PLQY.[394–396] Since the first demonstration of low-threshold, stable, tunable amplified spontaneous emissions (ASE) and lasing from methylammonium lead halides in 2014,[397–399] 3D HPs of different compositions have been extensively investigated for lasing using a variety of resonators. As discussed in the introduction, one of the most interesting properties of HPs is the tuning of the PL emission in the whole visible range and beyond, which makes them unique for lasing and other light-emitting applications. **Figure 27**a compares the tunable range of PL emission for Pb and Sn perovskite of different A-cation and halide compositions.[400,401] By varying the compositional combinations of A (MA, FA, and Cs), B (Pb or Sn), and X (Cl, Br, and I), the bandgap energies and emission spectra of all-inorganic ABX_3 are readily tunable over the entire visible spectral region to NIR (410–900 nm) with narrow PL bands (with linewidth in the range 12–42 nm) and high PL quantum yield (PLQY) that are beneficial for developing photon sources, as light-emitting diodes (LEDs), optical amplifiers and lasers.[29] As shown in Figure 27a, the Sn-based 3D HPs (THPs) can produce lasing in practically the same wide spectral range as the well-studied 3D LHPs. Nevertheless, the exploration of THPs for lasing is at its early stages, and the number of investigated Sn-perovskite systems is only a few, likely due to their relatively low performance in optoelectronic devices and poor stability as compared to LHP-based devices. In this context, we first introduce the achievements made in LHP-based lasers and then discuss the research progress of Sn-perovskite lasers in comparison with LHP systems, and provide an outline for promising directions in the field of Sn-perovskite lasers.

The total number of publications on ASE in LHPs exceeds a hundred (see for example the review[402]). The observation of ASE is a necessary condition for the fabrication of LHP lasers, but a resonator is also needed to provide positive optical feedback. Due to the soft and flexible nature of HPs, their shapes and sizes can be conveniently manipulated to obtain single crystals with regular and smooth end faces, which can naturally serve as Fabry-Perot (FP) or Whispering Gallery Mode (WGM) resonant cavities.

The simplest cavity is the FP geometry, which consists of only two end mirrors. The first LHP NW lasing from hybrid organic-inorganic perovskites ($MAPbX_3$) was reported in 2015.[403] The

single-crystal NWs of 8.5 μm length exhibit low lasing thresholds (0.22 μJ cm^{-2}), high-quality factors (≈3600), and broad spectral tunability covering from visible to NIR (≈500–790 nm). The single crystalline NWs have an internal FP cavity due to their large dimensions. Various other shapes of LHP single crystals including micro/nanorods and cubes also possess natural FP cavities to achieve optical gain.[84,353,404–407] Such single crystals can also exhibit WGM-type lasing. The WGM lasers have another type of cavity in which the light propagates as a ring to form a traveling wave amplification. The interface between the gain medium and air can provide total internal reflection due to the large difference between their refractive indexes. The high quality of microcrystals leads to low optical losses, and thus LHP WGM lasers were demonstrated with record-breaking laser line parameters. The first HP WGM laser based on hybrid organic–inorganic $MAPbI_{3-a}X_a$ perovskite NPls of the triangular or hexagonal shapes with a thickness of ≈150 nm and an edge length of ≈32 μm was demonstrated in 2014 (Figure 27b).[408] Later on, LHP WGM laser parameters were essentially improved to the quality factor of 1.5×10^4 with an FWHM of 0.037 nm for the case of $CsPbBr_3$ spherical microcavity (Figure 27c,d).[103] Another prospective approach to achieve low-threshold ASE from planar films is presented in Figure 27e, where the excitation beam is end-fire coupled at the input edge of the optical waveguide determined by the perovskite/PMMA bilayer structure.[409] The waveguide is efficiently excited along 1–3 mm longitudes, which results in extremely low ASE thresholds of 20–100 nJ cm^{-2}. The first LHP laser with an external cavity was realized in 2014.[397] It was FP mode vertical laser based on a distributed Bragg reflector with a lasing threshold as low as 0.2 μJ per pulse. Further optimization of similar Vertical Cavity Surface Emitting LHP Lasers was carried out by using different active compositions for both hybrid organic-inorganic and all-inorganic HPs.[410–417] For more examples of these types of lasers, see ref. [402].

Despite the high lasing parameters achieved for LHPs, the presence of the hazardous Pb limits their exploitation on an industrial scale.[418,45] Therefore, currently, an important task is the development of semiconductor gain media for lasers based on Pb-free halide perovskites with relatively simple and straightforward fabrication methods and similar emission efficiencies as their LHP counterparts. Among all, Sn halide perovskites (THPs) are the most promising candidates to substitute LHPs. It has already been demonstrated that all-inorganic as well as organic-inorganic THPs are suitable absorber materials for solar cells.[294,419] Furthermore, tin iodide perovskites exhibit emission in the near-infrared region, which is rare among wet-cast materials and, thus, makes them an attractive candidate for near-infrared LEDs and lasers.[283,420] However, the most challenging issue with THPs is the instability of Sn^{2+} ions that are easily oxidized to the Sn^{4+} state leaving Sn^{2+} vacancies, which results in unintentional p-type doping up to 10^{19} cm^{-3}.[421,422] Such high unintentional doping is undesired for solar cells because it results in fast electrons-hole (e^--h^+) recombination with characteristic lifetimes of tens to hundreds of picoseconds[137,420] and, consequently, short diffusion lengths in tens of nanometers. This is likely one of the main reasons for the relatively low efficiencies of the THP solar cells. Although high unintentional p-doping is detrimental for photovoltaics, it might turn beneficial for light emitting applications because the additional monomolecular recombination pathway between photoexcited e^- and h^+ released from dopants should be radiative for a direct bandgap semiconductor.[179] Such enhancement of radiative recombination should be helpful for lasing because the ASE threshold is governed by the radiative efficiency of the material.[423] Such examples are available in the literature. For instance, doped GaAs nanowires exhibit improved radiative efficiency and therefore increase in PLQY by several orders of magnitude, resulting in an essential decrease in the ASE threshold.[424] Indeed, in the first work demonstrating ASE and lasing in inorganic $CsSnI_3$ perovskites, the addition of 20% SnF_2 gives rise to an extremely low ASE threshold of 6 μJ cm^{-2} at room temperature,[425] which is unattainable in LHPs.[426]

A relatively low ASE threshold (388 μJ cm^{-2}) was reported for $FASnI_3$.[179] Note that the use of THPs for light-emitting and lasing applications requires a mandatory decrease in the natural degree of doping that is often observed for pristine materials. The PL lifetime in pristine THPs is as short as tens of picoseconds, which limits the gain for ASE to occur. Interestingly, the addition of 10–20% SnF_2 sufficiently decreases the hole doping densities to increase PL lifetime up to ≈0.5 ns which improves the conditions for ASE and lasing to occur.[427] The dependence of the ASE threshold on the concentration of the added SnF_2 was studied experimentally for $CsSnI_3$ films.[425] It was found that the increase in the SnF_2 concentration from 5 to 20% leads to a decrease in the ASE threshold from 17 to 6 μJ cm^{-2} (**Figure 28**a). To achieve low ASE thresholds, the shortening of PL lifetime caused by efficient intrinsic non-radiative recombination processes is critical, as in the case of $MASnI_3$ ($MASnI_3$) films.[428] The ASE threshold strongly depends on the preparation conditions that determine the PL lifetime and level of unintentional doping.[429] In addition, it was also shown why it is so important to ensure low ASE threshold values for lasing because the Auger recombination would increase with the concentration of photogenerated carriers especially for values close and above the Mott transition.[429]

It is important to stress that only a few studies demonstrated NIR ASE or lasing using Sn iodide perovskite thin films.[179,425,429–432] Especially, single-mode lasing was observed only in one of the works, where SnF_2-treated $CsSnI_3$ drop-casted on a butterfly wing was used as a gain medium with external cavities (Figures 28b-d). In this case, a low lasing threshold of 15 μJ cm^{-2} with a quality factor Q ≈ 500 was obtained.[425] Very recently, random lasing (RL) with a threshold as high as 18 mJ/cm^2 and a Q-factor of ∼3000 was observed for $CsSnI_3$ films,[430] whereas, for $FASnI_3$, low-threshold ASE (2 μJ cm^{-1} at 20 K and 50 μJ cm^{-2} at room temperature) and RL with a Q ≈ 10^4 was observed.[431] Finally, ASE with a threshold as low as 1 μJ cm^{-2} at room temperature was observed for $FASnI_3$ film confined in a planar waveguide.[432]

An important distinguishing feature of the RL in $FASnI_3$ films is the spectral stability of the observed narrow laser lines ($\Delta\lambda \approx$ 0.1 nm) in the multimode spectrum.[431] The reproducibility of the laser modes in the multimode spectrum is demonstrated in Figure 28e, where a set of RL spectra under excitation fluence increasing from 125 to 1150 μJ cm^{-2} is presented. The authors attributed the unusual spectral stability of multimode RL emission to the inhomogeneous broadening of the PL spectrum of $FASnI_3$ films (Figure 28f). It has been shown that each spectral mode in the RL spectrum corresponds to one space mode, and

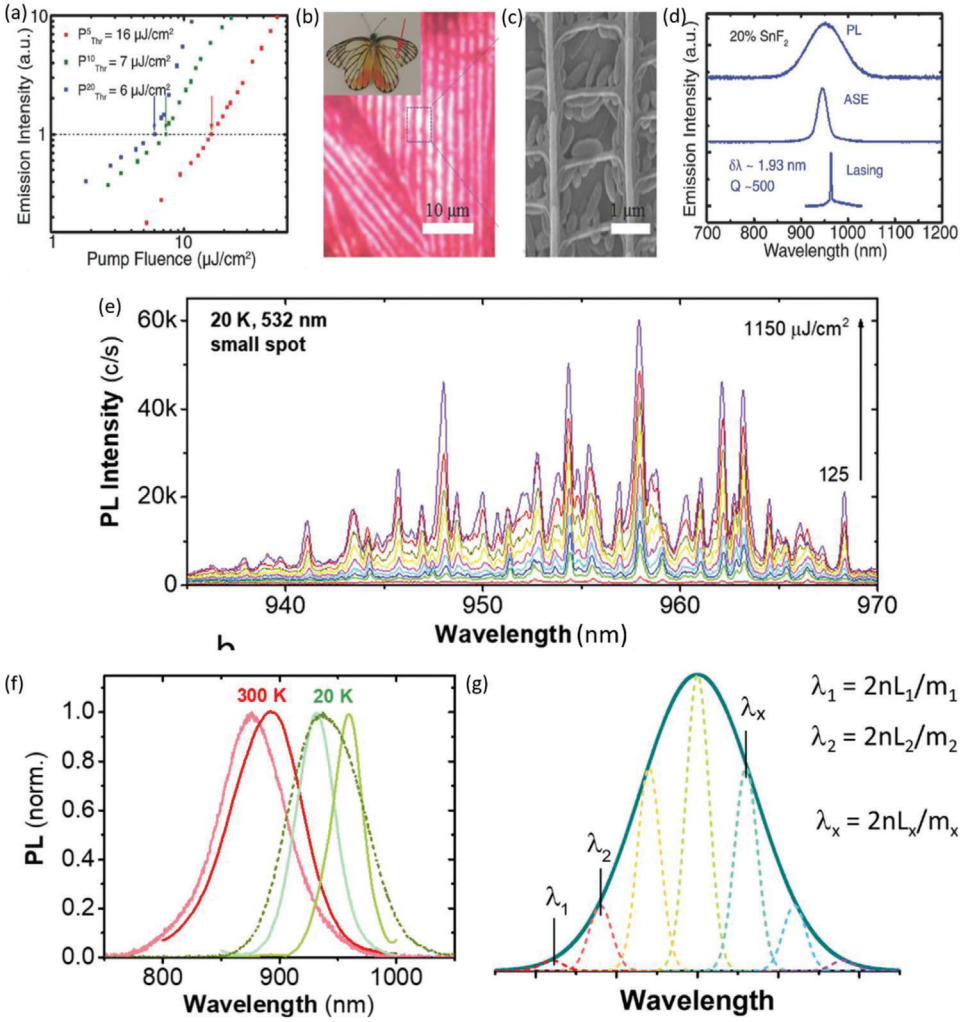

Figure 28. a) Variable fluence measurements of the ASE thresholds for three SnF_2-treated (5%, 10%, and 20% of SnF_2) samples of the butterfly wing. b) Optical image of a butterfly scale from the white part of the wing. Inset is a photograph of the butterfly. c) SEM image showing lamellae (vertical structures) in the scale. d) A comparison of the PL, ASE, and single mode lasing in $CsSnI_3$ (20% SnF_2); e) RL spectra of $FASnI_3$ thin film measured at 20 K under excitation by 532 nm pulses at different excitation fluences. f) Typical PL spectra of $FASnI_3$ films measured at 300 K (red colors) and 20 K (green colors) in different places of a sample under excitation spot size of about 400 μm that illustrates the sample inhomogeneity and PL spectra inhomogeneous broadening. g) The scheme explains the mechanism of generation of reproducible RL modes (narrow dashed contours) under conditions of inhomogeneously broadened amplification contour (solid line). a–d) Reproduced with permission.[425] Copyright 2016, WILEY-VCH Verlag GmbH & Co. KGaA, Weinheim. e–g) Reproduced with permission.[431] Copyright 2023, WILEY-VCH Verlag GmbH & Co. KGaA, Weinheim.

all the modes are localized in an excitation spot of ≈100 μm diameter. Such mode overlapping in standard RL systems having no inhomogeneous broadening inevitably results in their strong interaction and instability of the corresponding spectral modes. In systems with inhomogeneous broadening, the spatially overlapped modes do not interact as long as the spectral separation between the modes is larger than the homogeneous linewidth of the emitting centers.[433,434] The mechanism of the mode spectral stabilization is illustrated schematically in Figure 28g. Thus, as the previously proposed practical applications of HPs random lasing were mainly limited by speckle-free light sources,[435] the recently observed effect of spectral stabilization of multimode RL radiation in $FASnI_3$ thin films opens up prospects for their practical use as cheap sources for narrow laser lines. It is important to highlight that the samples of $MAPbI_3$ measured at the same experimental conditions as $FASnI_3$ do not exhibit random RL at room temperature, and the low-temperature RL is not spectrally stable as it was observed for $FASnI_3$.[431] Consequently, the THP laser is one of the few current systems that outperform LHP devices.

All these initial results have opened the doors for the development of NIR lasers based on THPs, where the aspects that are detrimental to the development of solar cells, such as self-doping or inhomogeneous broadening in the PL spectrum, are beneficial for the development of lasers. However, the development of lasers in the visible spectrum will undoubtedly require more research efforts to find ways to reduce non-radiative recombination.

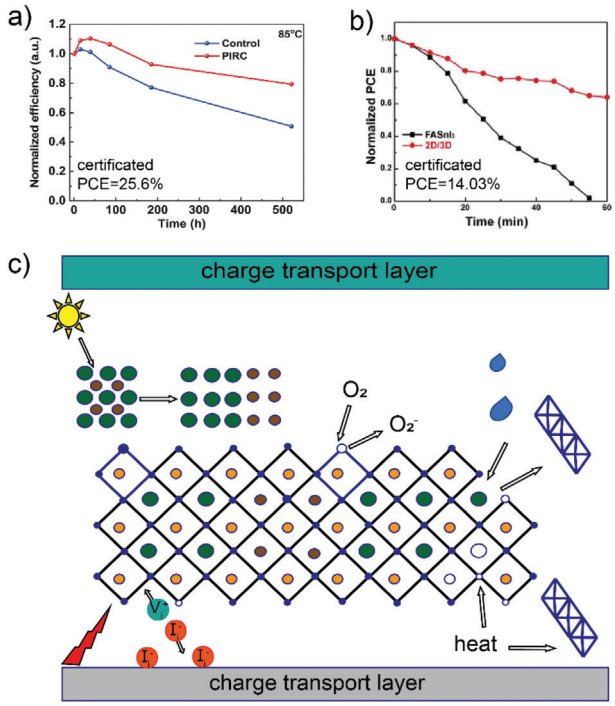

Figure 29. a) Thermal stability (at 85 °C) of the PSC with and without RbCl doping. Reproduced with permission.[438] Copyright 2022, The American Association for the Advancement of Science. b) Thermal stability analysis of the encapsulated Sn-based devices under continuous heating 80 °C in air. Reproduced with permission.[439] Copyright 2021, Wiley-VCH. c) Schematic illustration of the degradation pathways and mechanisms.

6. Degradation Mechanism of Pb- versus Pb-Free Perovskites

Despite the extraordinary increases in the PCE of PSCs, their operational stability is a major obstacle to their commercialization. In particular, the operation stability under external stress, such as light exposure, ambient air, bias, and elevated temperature (65-85°C, Figures 29a,b), is far behind that of Si-based solar cells.[436] Early-stage stability testing on laboratory-scale perovskite optoelectronic devices according to International Summit on Organic PV stability (ISOS)-L-3 standards is important for bringing the technology from lab to fab.[437] Therefore, understanding the degradation mechanism of perovskites (with and without encapsulation) under different stresses is required to find solutions for improving their stability (**Figure 29**c). This section summarizes the degradation mechanism of Pb- and Sn-based perovskite optoelectronic devices under light, oxygen, humidity, bias, and heat (Figure 29c). In addition, different in-situ characterization techniques that are being used to monitor the degradation process are also discussed along with an outlook of the methods to enhance the stability of Sn-based perovskite solar cells.

To study the degradation mechanism, several in situ probing techniques with high time resolution are utilized, which include XRD, electron microscopy, tip-based, and visible/infrared absorption.[440] Among all, synchrotron-based grazing-incidence X-ray scattering techniques feature good statistics and are non-destructive. These features make them indispensable tools to investigate the degradation mechanisms of PSCs through the perspectives of morphology and crystal structure and orientation.[389,441,442] Regarding electron microscopy techniques, SEM is often used to characterize perovskite morphology on the basis of electron backscattering diffraction (EBSD) and cathodoluminescence (CL), whereas TEM has been used to study the effect of external stress on the crystal structure at the atomic level.[443] Nevertheless, electron beam irradiation can result in local heating and even decomposition of perovskites, thus special care is required to avoid beam-induced damage. On the other hand, Kelvin probed forced microscopy (KPFM) has evolved as one of the non-destructive methods that can map the surface potential to obtain the work function of the sample. This provides the electrical changes of optoelectronic devices, which combined with other probing techniques.[444] Likewise, optical spectroscopic techniques have also been used to obtain direct information of the recombination kinetics and internal electrochemical potential of free charge-carriers in pure perovskite films, perovskite layer with charge transport layers, and full devices.[445] For example, by combing transient PL microscopy with confocal microscopy, one can track the charge carrier transport in the out-of-plane direction to visualize the heterogeneity of charge diffusivities in a 3D perovskite film, which can be correlated with their degradation.[446] For extensive details on the characterization techniques used for studying the degradation mechanisms, we refer the readers to the literature.[440,443,445,447]

6.1. Degradation Mechanisms of LHPs

6.1.1. Moisture-Induced Degradation

The humidity-induced degradation initiates at grain boundaries, and consists of an amorphous intergranular layer that facilitates fast moisture uptake,[448,449] and then further expands towards the interior grains along the in-plane direction. In addition, grain fracture is found during moisture invasion, which depends on the tensile strength of the top region of the perovskite film.[450] The tensile strength originates from the volume expansion caused by the faster cooling of the top region as compared with the bottom region of perovskite film during annealing. With further permeation of moisture, perovskites undergo hydration and even decomposition. Moisture-induced degradation of perovskites can be also understood from the perspective of defects, where point defects are identified as the degradation sites because of their affinity to water and oxygen molecules.[451] In addition, the absorption energy of water molecules at vacancy defects is much higher than that of pristine surfaces, indicating the accelerated degradation at the vacancy sites.[452] Notably, the formation of point vacancies, i.e., V_I and V_{MA}, are more favorable than the formation of V_{MAI}. Therefore, the formation of CH_3NH_2 or I_2, or HI is more likely than the formation of MAI under moisture-induced degradation.[453] It should be noted that the PbI_2-terminated surfaces are stable in the presence of water, whereas MAI-terminated surfaces are prone to solvation.[454] We further refer readers to the literature that summarized the moisture-induced degradation mechanisms, and methods to enhance the stability against moisture.[448,455,456]

Besides degradation, Iodide-based perovskites can also undergo a phase transformation at ambient conditions, i.e., from the photoactive black phase (α (or γ)-$CsPbI_3$ or α (or γ)-$FAPbI_3$) to the nonactive yellow phase (δ-$CsPbI_3$ or δ-$FAPbI_3$). Several factors such as pressure, humidity, and heat can accelerate this phase transition.[457–459] For instance, Yang et al. demonstrated the laser-induced transformation of the high-temperature phase (α) $CsPbI_3$ undergoes a phase into the thermodynamically stable low-temperature non-perovskite phase (δ) under ambient humidity.[460] Such phase transition was attributed to the formation of humidity-induced halide vacancy at the perovskite-water interface, which lowers the phase transformation barrier, leading to a faster nucleation rate.[461] Interestingly, the light illumination alone did not result in phase transformation except for PL quenching. Similarly, $FAPbI_3$ perovskites also suffer from a phase transformation to the yellow phase δ-$FAPbI_3$ when it exposed to moisture. Theoretical calculations and experiments indicate that a strong water adhesion after hydroxylation with an elongated Pb-I distance is responsible for the phase transition and particularly the (100) facet of $FAPbI_3$ perovskite is more susceptible to moisture-induced degradation compared to (111) facet.[462] The unwanted phase transformations could be avoided through the device encapsulation under inert conditions.[457]

6.1.2. Oxygen-induced degradation

Analogous to moisture-induced degradation, oxygen-induced degradation is also initiated at the surface layer and grain boundaries, at which the smaller and more irregular grains are more affected.[463] A previous study has demonstrated that photoexcitation leads to the formation of superoxide (O_2^-) through electron transfer to molecular oxygen. Such O_2^- facilitates the deprotonation of the MA^+, resulting in the formation of PbI_2, H_2O, I_2, and methylamine (Equation 1).[464] Thus, the device instability in the presence of O_2 can significantly affect the efficiency of electron extraction of the electron transport layer (ETL). For example, the devices utilizing compact-TiO_2/mesoporous Al_2O_3 or compact-TiO_2 as ETLS exhibit a significant decrease in PCE of PSCs in less than 1 h in the dry air, while the lifetime of devices with mesoporous TiO_2 layer is greatly enhanced because of the suppression of superoxide formation.[465,466] Moreover, oxygen-induced degradation can be accelerated by surface iodine vacancy and the absorption of water.[467] This is because the energy level of absorbed O_2 is significantly reduced, facilitating the photoexcited electron and therefore the formation of O_2^-.

$$CH_3NH_3PbI_3 + O_2 \rightarrow CH_3NH_2 + PbI_2 + 1/2I_2 + H_2O \quad (1)$$

6.1.3. Heat-Induced Degradation

The heat-induced degradation also initiates at the surface and then slowly propagates into bulk. Such degradation starts by breaking the relatively weak Pb-I bond, leading to the formation of PbI_2, CH_3NH_2, and HI or other decomposition products (Equations 2,3). In contrast to the moisture-induced degradation, no intermediate phases were observed during decomposition.[468] It is demonstrated that heat-induced degradation facilitates the formation of particles and dark voids.[456] In addition, iodine and lead migration are responsible for the degradation under heat, as evidenced by in-situ TEM measurements.[469]

$$CH_3NH_3PbI_3\ (s) \rightleftharpoons CH_3NH_2\ (g) + PbI_2\ (s) + HI\ (g) \quad (2)$$

$$CH_3NH_3PbI_3\ (s) \rightarrow CH_3I\ (g) + PbI_2\ (s) + NH_3\ (g) \quad (3)$$

6.2. Degradation Mechanisms of Pb-free Perovskites

6.2.1. Sn-Based Perovskites

Among all the elements that can replace the Pb of $APbX_3$ perovskites, Sn has attracted vast intention due to the suitable properties of $ASnX_3$ for optoelectronics (e.g., ideal bandgaps and broad absorption and direct-bandgap nature) as compared to other elements. Nevertheless, the propensity of oxidation of Sn^{2+} to Sn^{4+} and tin vacancy formation are by far the most notorious factors that cause the instability of Sn-based perovskites, and thus lead to poor device performance. Pb is most stable at the 2+ oxidation state, but this oxidation state is not stable for the elements above Pb in group 14. As such, tin tends to adopt the 4+ oxidation state, leading to the oxidation of +2 state of HPs.[422] In this regard, we particularly discuss the degradation mechanism of Sn-based perovskites in relation to tin oxidation and tin vacancy formation.

6.2.2. Oxygen-Induced Degradation

Theoretical calculations suggest that when $FASnI_3$ is exposed to O_2, the O-O distance of O_2 molecules is elongated, corroborating that they are likely to be dissociated on the Sn-I terminated surface and participate in the formation of SnO_2.[470,471] One of the possible chemical degradation processes of THPs is illustrated in Figure 2a. In detail, the oxidation of pure THPs undergoes a cooperative degradation process involving adjacent Sn^{2+} to form SnO_2 and SnI_4 (Equation 4).[472] In addition, the SnI_4 further evolves into iodine under oxygen and moisture via a two-step process: i) the formation of hydrogen iodide by the reaction of SnI_4 and water molecules, and ii) the formation of I_2 by oxidation of hydrogen iodide (**Figure 30**a).[470] Interestingly, the I_2 in turn intensify the oxygen-induced degradation of Sn-based perovskites, and therefore enables a cycling degradation mechanism (Figure 30a, process 5). More recently, Wei et al. found that the annealing process induces the disproportion decomposition of Sn^{2+} (Equation 5).[473] In addition to the iodine vacancies formation under light and oxygen, first-principle calculations disclosed the structural changes (e.g., weakened interaction of FA^+ with I^-) and other decomposition byproducts (i.e., H_2O, OOH^-, and H_2O_2) that can further lead to the final chemical decomposition of $FASnI_3$.[474] To sum up, degradation of both Pb and Sn-based perovskites upon exposure to O_2 initiates at the surface and causes structural change and at last chemical decomposition. Nevertheless, the main chemical degradation products of Sn-based perovskites are SnI_4 and SnO_2, while the degradation product in Pb-based perovskites is mainly PbI_2. The absorption of O_2 molecules in both cases facilitates the formation of iodine

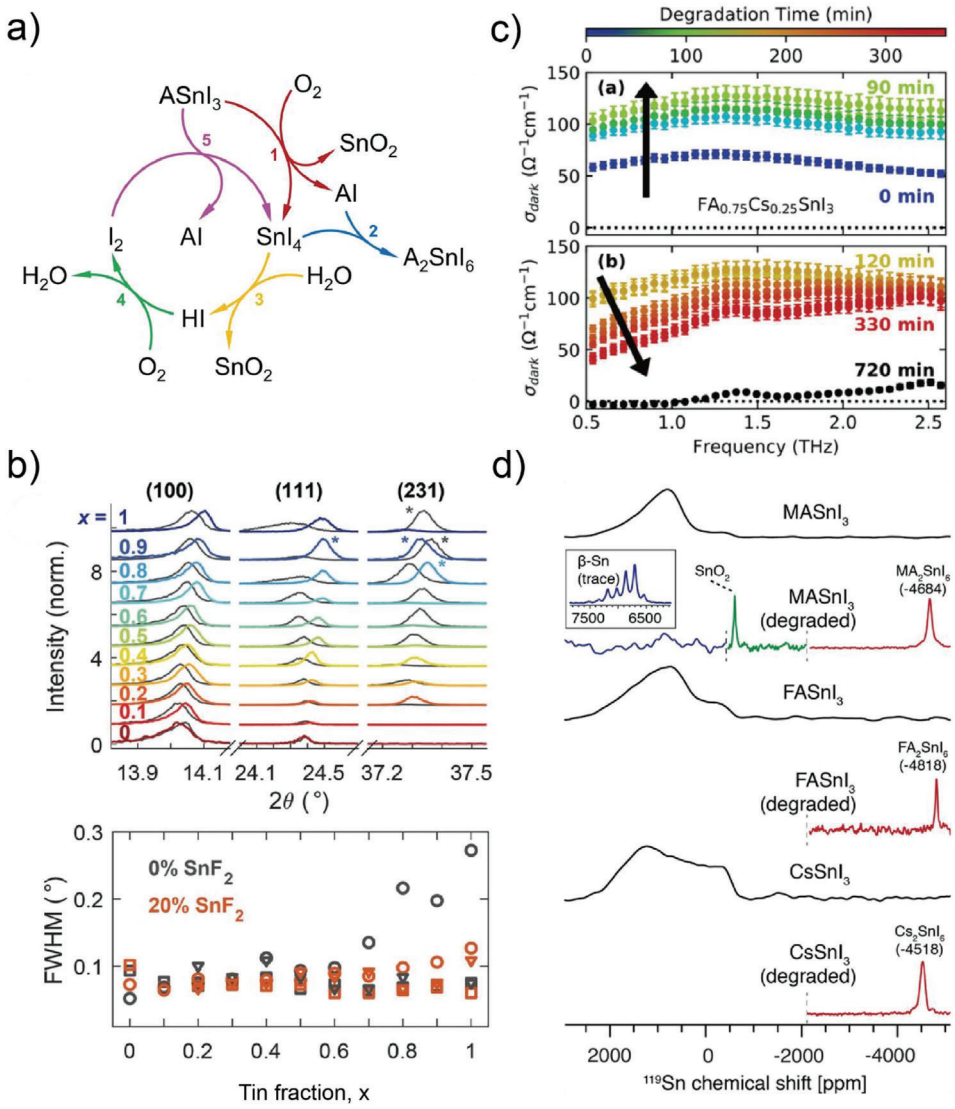

Figure 30. a) Proposed cycling degradation mechanism of Sn-only perovskites under ambient air exposure, where 5 reactions are disclosed, and A represents the organic cation. Reproduced under the terms of CC BY 4.0.[470] Copyright 2021, The Authors, published by Springer Nature. b) Upper image: XRD patterns of $FA_{0.83}Cs_{0.17}Sn_xPb_{1-x}I_3$, where x refers to the Sn fraction and pseudo cubic (100) and (111), and tetragonal (231) peaks are indicated. In each XRD pattern, data of the 0% SnF_2 condition and 20% SnF_2 condition are shown in gray and overlaid in color, respectively. Lower image: FWHM of the (111) peaks. Reproduced with permission.[478] Copyright 2020, Wiley-VCH. c) Dark conductivity spectra of a $FA_{0.75}Cs_{0.25}SnI_3$ thin film under different operation times in the air, where the timeline is demonstrated by the color legend. Reproduced with permission.[450] Copyright 2022, Wiley-VCH. d) ^{119}Sn solid-state MAS NMR spectra showing the degradation product of tin (II) halide perovskite, in which $MASnI_3$, $FASnI_3$, and $CsSnI_3$ are degraded under exposure to 150 °C in the air for 1 h, RT in the air for 1 h, and 100 °C in the air for 3 h, respectively. Reproduced under terms of the CC-BY license.[479] Copyright 2020, the Authors, published by American Chemical Society.

vacancies, whereas tin vacancies are easily formed as compared to that of Pb. Further details on the role of defects in the oxygen-induced degradation of Sn-based perovskite are discussed below.

$$2FASnI_3 + O_2 \rightarrow 2FAI + SnO_2 + SnI_4 \quad (4)$$

$$2Sn^{2+} = Sn^{4+} + Sn \quad (5)$$

The oxidation and thus the degradation of Sn-based perovskites can also be understood from the defect's perspective, i.e., the formation of tin vacancies and interstitial defects. Theoretical calculations suggest that the highly stable tin vacancies and interstitial defects originate from the inherent low ionization of $MASnI_3$ and can cause p-doping.[475] In other words, tin vacancies and interstitial defects are easily formed below the valence band edge, where the electrons are captured, effectively releasing free holes and resulting in hole enrichment.[476] For instance, a monotonic increase in the density of holes for $FA_{0.75}Cs_{0.25}SnI_3$ arising from tin vacancy formation was found after 90 min exposure to air, as evidenced by THz conductivity spectra (Figure 30c).[450] As a result, these tin vacancies in turn create a locally iodine-rich environment and then facilitate the

oxidation of Sn^{2+} to Sn^{4+} and further chemical decomposition. The THz dark conductivity spectrum shows two peaks (at 1.4 and 2.5 THz) after 12 h aging in the air (Figure 30c), corroborating the formation of vacancy-order DPs (i.e., Cs_2SnI_6).[450] Moreover, the deep traps associated with uncoordinated Sn defects are easily formed due to their high band edge energies, resulting in non-radiative recombination. On the other hand, it was reported that the oxidation of Sn^{2+} to Sn^{4+} is activated at the surface instead of bulk, whereas the electron traps (undercoordinated tin defects) catalyze the lattice degradation.[477] For example, the appearance of the tetragonal (231) peak along with the broadening of the (111) peak in the XRD of Sn-rich perovskites (Sn fraction greater than 0.5) manifests a tetragonal distortion induced by tin vacancies, which further leads to the enhanced background hole density and increased energy disorder (Figure 30b).[478] In addition to tin vacancies, it was reported that the absorption of O_2 can also greatly promote the formation of iodine vacancies under light illumination, resulting in the degradation of $FASnI_3$.[474]

6.2.3. Humidity-Induced Degradation

Analogous to the degradation of LHPs, Sn-based perovskites also decompose into MAI and HI in the presence of water. With further permeation of moisture, MAI undergoes deprotonation and subsequently decomposes to volatile sym-triazine and NH_4I.[213] In addition, water molecules are prone to form an H-I bond on the (011) surface of $MASnI_3$, leading to a weaker Sn-I bond and thus resulting in the instability of $MASnI_3$.[480] On the other hand, ab initio molecular dynamics simulations suggest that water molecules bind to the surface Sn atoms and induce the breaking of Sn-I bonds, resulting in the dissolution of the SnI_2-terminated $MASnI_3$ surface. By contrast, the PbI_2-terminated $MAPbI_3$ surface shows higher moisture stability, with the Pb-I bond remaining stable after increasing the absorption of water molecules.[481]

6.2.4. Heat-Induced Degradation

The heat-induced degradation products of $MASnI_3$ are MA_2SnI_6, SnO_2, and trace amounts of metallic β-Sn (Figure 30d), as evidenced by NMR.[479] The formation of SnO_2 and SnX_4 manifests that the organic component has been fully volatilized. In addition, the NMR signal related to SnO_2 (with FWHM 3.5 kHz) is broader in the degraded perovskite as compared with pure SnO_2 signal (0.2 kHz), indicating that the degradation product of SnO_2 is highly disordered. Such degradation is independent of the A-site cation and halide component (Figure 30d).

To sum up, a relatively low ionization energy is in favor of forming Sn vacancies along with p-doping, exacerbating the oxidation of Sn^{2+} and resulting in unstable Sn-based perovskites. In addition to the defects originating from the oxidation of Sn^{2+}, the fast crystallization of Sn-based perovskites would also cause morphological defects, e.g., pinholes, cracks, and irregular grain packing.[482] Thus, further endeavors should be particularly devoted to passivating the defects and inhibiting the hole doping as well as controlling the crystallization process. Four major methods for enhancing the stability of Sn-based perovskite including additive engineering, deoxidizers, partial substitution, and dimensional engineering are briefly discussed. Regarding the additives, SnF_2 is a widely used inorganic additive for inhibiting the oxidation of Sn^{2+} and reducing Sn-cation vacancy, thus enhancing the stability of Sn-based perovskite.[425] Likewise, the addition of organic additives such as Butylammonium iodide and ethylenediammonium diiodide to Sn-based perovskites gives rise to a better morphology, reduced defect states, and enhanced crystallinity.[483] In addition, reducing agents, e.g., ascorbic acid can also suppress the oxidation of Sn^{2+} and concomitantly modulate perovskite crystallization through intermediate complexes, forming a uniform and dense film with less trap densities. Thus, the PSCs based on $MA_{0.5}FA_{0.5}Sn_{0.5}Pb_{0.5}I_3$ demonstrated improved stability as well as PCE.[484] On the other hand, it was found that the stability of $FASnI_3$ can be improved by replacing some of the FA^+ ions with Cs^+. The enhancement was attributed to the improvement of geometric parameters and lowering of free energy caused by the contraction of SnI_6 octahedra upon the cation replacement. As a result, it leads to a reduced trap density and an enhanced thermodynamic stability of perovskites. The PCE of Cs-doped $FASnI_3$ PSCs remains at 90% of its initial value after 2000 h of storage in an N_2 atmosphere.[485]

Regarding the enhanced stability by dimensional engineering, 2D perovskite with bulky organic cations can inhibit the penetration of oxygen and humidity, thus enhancing the stability of LHPs as well as Sn-based perovskites. In addition, 2D perovskite can reduce the formation of defects and is in favor of lower self-doping levels.[486] For instance, a 2D passivation layer was utilized in Pb-Sn mixed perovskite, leading to a decrease in non-radiative recombination and an improvement in moisture stability. Likewise, reducing the dimensionality of the perovskite structure by adding 2D organic bulky cation (e.g., PEA^+) results in the improved thermodynamic stability of $(PEA)_2(FA)_{n-1}Sn_nI_{3n+1}$ as compared with $FASnI_3$.[487] For a comprehensive discussion of mitigation strategies, we refer the readers to the literature.[471,488,489]

6.3. Degradation Mechanisms of Sn–Pb Hybrid Perovskites

The incorporation of Pb into Sn-based perovskites leads to the suppression of the Sn^{2+}-Sn^{4+} transformation and thus results in a dramatic enhancement of their stability. However, Sn-Pb hybrid perovskites are also unstable and can undergo oxidation. Contrary to pure THPs, Sn-Pb mixed perovskites oxidize much more slowly and give rise to the degradation products I_2, SnO_2, and PbI_2 (Equation 3). The activation energy to initiate the oxidation of Sn-Pb mixed perovskites (Equation 6) and pure Sn-perovskites (Equation 4) is 731 meV and 573 meV, respectively, indicating that Sn-Pb mixed perovskite is more robust to oxidation compared to pure-perovskites.[472] In addition, the oxidation of Sn^{2+} is not an isolated process but is normally accompanied by the oxidation of I^- and the reduction of Pb^{2+} and Sn^{4+} under ambient conditions (**Figure 31**a).[490] The degradation was found to be predominantly initiated at the surface instead of the bulk and led by the local electrochemical potential, which is defined by the local chemical composition (i.e., defects, mobile ions, and decomposition products). On the other hand, the as-formed oxidation product (SnO_2) on all interfaces is detrimental to charge

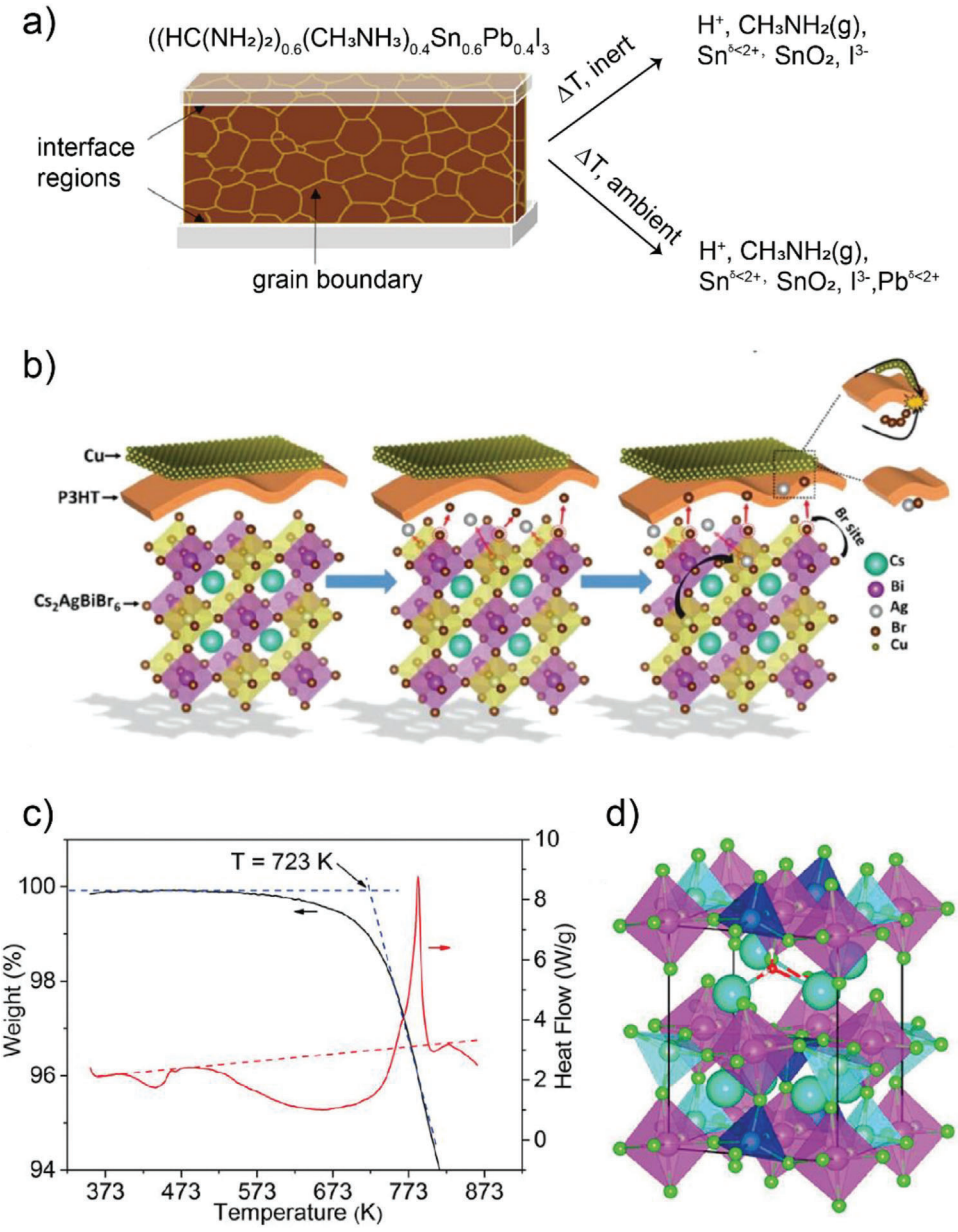

Figure 31. a) Schematic illustration of the degradation mechanism of mixed Sn-Pb perovskites. Reproduced with permission.[490] Copyright 2020, Americal Chemical Society. (b) Schematic of degradation mechanism of $Cs_2AgBiBr_6$ solar cell, where Ag and Br ions migrate through P3HT/Perovskite interface. Reproduced with permission.[276] Copyright 2020, Wiley-VCH. (c) TG (black) and DTA (red) data of $Cs_2LiBiCl_6$ perovskite from RT to 873 K, where the initial weight loss starts at 523 k. (d) Structural deformation of $Cs_2LiBiCl_6$ perovskite lattice, where green, cyan, purple, and large green sphere represent Cl, Cs, Bi, and Li, respectively. Purple and green octahedra, and cyan tetrahedra represent $BiCl_6$, $LiCl_6$, and $LiCl_4$, respectively. Reproduced with permission.[229] Copyright 2021, Americal Chemical Society.

extraction, and in turn, causes the J_{SC} loss and deterioration of the solar cell performance. In contrast to the shallow defects and p-doping-induced degradation in THPs, Herz et al.[450] unraveled that the degradation of mixed Sn-Pb perovskites can be correlated with the formation of deep trap states (i.e., tin interstitials and iodine vacancies), which trigger trap-mediated recombination. Surprisingly, unlike the tin vacancies in THPs, these deep trap states impact the charge carrier mobilities. Iodine vacancies likely play a dominant role in the degradation by facilitating the ion migration and serving as degradation sites, which cause the non-radiative recombination and corrosion of the electrode.[491]

$$2ASn_{0.5}Pb_{0.5}\,I_3 + O_2 \rightarrow 2AI + SnO_2 + PbI_2 + I_2 \quad (6)$$

In summary, the formation of deep trap states drives the degradation of mixed Sn-Pb perovskites and leads to enhanced trap-mediated recombination. In contrast to the degradation products of Sn-only perovskites, iodine, and PbI_2 are the main products

of mixed Sn-Pb perovskites. On the other hand, the oxidation of Sn^{2+} is accompanied by the oxidation of I^- and the formation of uncoordinated Sn and Pb surface sites, suggesting that surface chemistry dominates in the degradation of mixed Sn-Pb perovskites.

6.4. Degradation Mechanisms of Double Perovskites

DPs exhibit high charge carrier lifetime, long charge diffusion length, and superior stability under ambient conditions as compared to LHPs.[224,225] Nevertheless, the defective chemistry of DPs often dominates their degradation. For instance, in $Cs_2AgBiBr_6$ perovskites, Ag vacancies are shown to be shallow defects, whereas Bi vacancies and Ag_{Bi} antisemites are deep acceptors and dominant defects under Br-rich conditions.[225] Consequently, to maximize the device performance and suppress degradation, $Cs_2AgBiBr_6$ films should be grown under Br-poor conditions. Contrary to the above-mentioned defects, negatively charged Br vacancies in $Cs_2AgBiBr_6$ create detrimental donor-yield centers, facilitating non-radiative electron-hole recombination and deteriorating device performance.[492] On the other hand, Ghasemi et al. demonstrated that Ag and Br vacancies drive the dual-ion migration of $Cs_2AgBiBr_6$ perovskites and lead to subsequent device failure (Figure 31b).[276] The Ag and Br ion migration is intrinsically derived from the low formation energy of Ag and Br vacancies as well as the low diffusion energy barrier.

The degradation strongly depends on the chemical composition of the DPs. For instance, it was reported that $Cs_2In(I)M(III)X_6$ perovskites are intrinsically unstable and can oxidize into In(III) compounds under both thermodynamic equilibrium and non-equilibrium conditions, as driven by the reduction/oxidation potential for In(I) and Bi(III).[493] Moreover, $Cs_2LiBiCl_6$ perovskites started to decompose at 523 K due to the loss of $BiCl_3$, and complete decomposition occurred at 573 K (Figure 31c). This results in the formation of the Cs_3BiCl_6 phase and an amorphous phase.[229] More recently, by combining thermogravimetry analysis and temperature-dependent Raman study, Sudakar et al. demonstrated that high-power laser light (7.15 mW) induces the decomposition of $Cs_2AgBiBr_6$ into $Cs_3Bi_2Br_9$ at a temperature above 180 °C.[494] In addition, water molecules are found to easily diffuse into the perovskite lattice and lower the total binding energies of $Cs_2B'BiCl_6$ with the intercalation water molecules, resulting in structural deformation, i.e., the transformation from $LiCl_6$ octahedra to $LiCl_4$ tetrahedron (Figure 31d).[229] Likewise, a previous study revealed that $Cs_2AgBiBr_6$ perovskites degrade after several weeks under light and humidity, whereas they are stable upon exposure to light.[225] In contrast to the unstable $Cs_2LiBiCl_6$, Xu et al. disclosed that $Cs_2NaBiCl_6$-based photodetectors exhibit a steady photoresponsivity and response time under heat disturbance, which is ascribed to the superior structural rigidity.[495]

6.5. Effect of Charge Transport Layers on the Operational Stability

The operational instability of perovskite optoelectronic devices is not only linked to the degradation of the perovskite layer, but also highly related to the charge transport layers that are directly in contact with perovskite layers and electrodes.[496–498] As the photogenerated carriers transport through electron and hole transporting layers, the perovskite/charge transport layer interfaces play a crucial role in determining the overall operational stability of perovskite optoelectronic devices. The charge transport layers can trigger the degradation of perovskites through photocatalytic process or heat generation, however, they can also help to protect the perovskite layer from entering of water and oxygen.[496–498]] Here, we limit the discussion on the effect of charge transport layer only to inverted device configuration (p-i-n) since it is the most widely used configuration in lead-free PSCs. Among all HTL materials, PEDOT:PSS remains the most commonly used in inverted PSCs. However, the interface of PEDOT:PSS and Sn-Pb mixed perovskite suffers from thermal instability (85 °C), resulting in a significant drop in performance.[499] The intrinsic hygroscopic character of PEDOT:PSS renders PSCs vulnerable to humidity. In addition, a previous study found that PEDOT:PSS can chemically etch the ITO (indium tin oxide) due to its acidic nature, leading to the instability of organic LEDs.[500] For the ETL materials, C60 and PCBM are the leading choices in PSCs because of their suitable charge transport properties and electron affinity. Nevertheless, previous studies showed that fullerene is a limiting factor in the operational stability of lead-free PSCs, *e.g.*, exposure to UV light or high temperatures (85 °C) causes dimerization and agglomeration of fullerenes, which further leads to the deterioration of PSCs performance.[501,502] In addition, it has been demonstrated that V_{OC} losses is dominant at the interface of perovskite/fullerene in Pb-Sn mixed PSCs, suggesting the high interface trap densities.[503] Thus, further efforts should be particularly devoted to optimizing the charge transport layers (e.g., adding additives, ionic liquid), developing new materials for charge carrier transport (e.g., self-assembled monolayers, non-fullerene acceptors), and engineering the interface of charge transport layer/electrode to enhance the device performance and long-term stability of lead-free PSCs.

To wrap up, DPs exhibit relatively higher stability compared to LHPs as well as Sn-perovskites, but are still prone to defect formation, particularly deep-level defect formation. Thus, it is imperative to passivate defects, that is, to mitigate the possible antisite defects (Ag_{Bi} and Bi_{Ag}), Br, and Bi vacancies, to reduce non-radiative recombination and boost device performance and stability. DPs are found to be sensitive to external stimuli, however, stability-related studies are still rare, and diligent work in terms of enhancing intrinsic stability and stability under external stimuli is highly required and should be prioritized.

7. Summary and Outlook

Over the past decade, we have witnessed tremendous advances in the field of LHPs in terms of fundamental understanding, materials development, and efficiency in optoelectronic and photovoltaic devices. For instance, the certified PCE of perovskite solar cells has already exceeded 26%,[22] while the EQE of perovskite LEDs (green) has exceeded 30%.[504] Despite significant performance advances, the toxicity of Pb is of the major concerns for bringing the technology from the lab to the real world. Governments across the globe have restricted the use of Pb in consumer products goods. This has triggered the search for non-toxic metal ions that can replace Pb in LHPs while preserving their

properties. Various metal cations, including Sn, Ge, Sb, Bi, and In, used independently or in combination with other metal ions, have been found to be potential alternatives to replace Pb.[2,52] This review has discussed the preparation, properties, and potential applications of various Pb-free ABX_3 perovskites and $A_2B^IB^{III}X_6$ DPs. The review has covered both colloidal NCs and thin film perovskites. Whereas colloidal NCs have been mainly exploited in LEDs and X-ray detectors, thin films have been investigated in the fabrication of solar cells, LEDs, lasers, and radiation detectors. For each of these research lines, we have provided the current status in terms of fabrication and efficiency, and outstanding challenges that need to be addressed to drive the field of Pb-free perovskite optoelectronics toward real-world applications.

Among all, THPs turn out to be promising for achieving relatively high-efficiency solar cells as well as light-emitting devices because their properties are very similar to those of LHPs. In addition, the low bandgap of iodide-based THPs enables the tunability of their emission toward infrared, beyond the reach of LHPs. However, the stability of THPs is worse than that of LHPs due to the rapid oxidation of Sn^{2+} into Sn^{4+} under ambient conditions. Despite a few successful attempts to synthesize high-quality monodisperse THP NCs, they exhibit very low PLQYs (<1%) and poor stability as compared to LHP NCs because of the high density of structural and atomic defects caused by the oxidation of Sn^{2+}. The PLQY of LHP NCs could be improved to over 15% by controlling the chemistry of precursors. On the other hand, LHP NCs routinely exhibit over 80% PLQY even using technical grade precursors and ligands. Besides, the level of shape control achieved in the case of THP NCs is limited, mainly nanocubes and NPls have been reported. Therefore, future studies should focus on achieving better shape control, high PLQY, and high stability. The suppression of the oxidation of Sn^{2+} by surface ligands or through encapsulation should enable the preparation of highly luminescent THP NCs. The research on the synthesis of THP NCs is still in the early stages, and it is still extremely challenging to use them in the fabrication of LEDs. On the other hand, thin films of 2D and 3D THPs have been successfully used in the fabrication of LEDs with an EQE of over 5%.[319] Significant efforts are required to further improve the EQE of THP LEDs using organic molecules (additives) that strongly passivate the surfaces and prevent nonradiative recombination. To select suitable additives, an in-depth understanding of the degradation mechanism of THPs and the role of additives in the stabilization of the 2+ oxidation state of Sn is required. Another metal ion that has similar properties as Sn is Ge, but Ge-based perovskites exhibit very weak PL, and thus they have not been explored in LEDs. Interestingly, thin films of 3D THPs exhibit ASE/random lasing in the presence of SnF_2 additives. Generally, the excited state decay of pure THPs is in picoseconds (ps), however, upon SnF_2 addition, the decay gets slower (nanoseconds range) and facilitates the gain for ASE to occur at a low threshold (15 μJ cm^{-2}). The SnF_2-treated THPs ($FASnI_3$) exhibit random lasing in the NIR region at a threshold of 15 μJ cm^{-2} with a quality factor $Q \approx 500$. The THP laser is one of the few systems that outperform LHP-based devices. Future studies should focus on studying lasing in encapsulated THPs with tunable emission and achieving single-mode lasing. The THP thin films made of mixed 2D and 3D systems could be interesting to investigate lasing as they exhibit improved stability compared to 3D thin films.

Besides, the thin film THPs have shown promise for solar cells with a record efficiency approaching 15% PCE, and there is plenty of room to achieve over 20% by suppressing the loss in V_{OC} and FF. $FASnI_3$ PSCs generally exhibit higher efficiency and stability as compared to $CsSnI_3$ and $MASnI_3$ PSCs. Currently, research on improving lattice stability, crystallinity, and passivation are the main research directions of Sn-based perovskites.[187] A large number of organic and inorganic additives have been used for passivation. However, a systematic investigation of additives and their role in the stabilization of THPs is lacking in the literature. Moreover, a better understanding of the charge carrier transport properties of THPs is needed to optimize the performance of THP SCs. Recent developments in computation and machine learning could help to find out better additivities, the thickness of THP thin films, transport materials, and optimum device architecture to further improve the PCE of THP SCs. On the other hand, Ge-perovskites exhibit poor device performance with PCE <1%.[204] Interestingly, the efficiency can reach over 13% by combining Ge with Sn.[197]

Furthermore, $A_2B^IB^{III}X_6$ DPs have received special interest as Pb-free materials due to their superior stability over THPs (against light and humidity) and the interesting properties arising from their stoichiometry. DPs have been exploited for SCs, LEDs, and X-ray scintillators. Whereas DP thin films are promising for SCs, doped-DP powers, and colloidal NCs have emerged as promising materials for down-conversion LEDs. Among all, $Cs_2AgBiBr_6$ DPs have been extensively investigated for solar cells, with the PCE improved from 2.43% (reported in 2017) to 6.37% (reported in 2022). However, the record PCE of DP SCs is still much lower than that of LHP SCs (26.1% as of mid-2023). The main challenges associated with $Cs_2AgBiBr_6$ DPs are their large indirect bandgaps, non-ideal device structures, and the prominent role played by defects. Therefore, there is still room for improving the PCE of DPs by the stoichiometry engineering (metal ions as well as halides) of DPs and optimizing the device architecture.

Although DPs exhibit weak PL due to their indirect bandgap, they can be highly luminescent upon doping/alloying with other metal ions. Alloying of DPs could induce indirect-to-direct band gap transitions and boost their PL emission.[104,105] After the demonstration of strong white light emission from Bi^{3+}-doped $Cs_2Ag_{0.6}Na_{0.4}InCl_6$ DPs (PLQY increases from <0.1% to 86% upon doping),[92] a large number of doped/alloyed DPs have been exploited for down-conversion LEDs of different colors, especially to achieve white light emission. Doping/alloying of DPs breaks the parity-forbidden transition and modulates the density of states effectively to boost the PLQY, and dopants can alter the emission color from visible colors to white light emission. The PL of DPs originates from STE, thus, they exhibit broad emission with large Stokes shift, and therefore, they are suitable for single-component WLEDs. Despite significant progress in DP-based down-conversion LEDs, electric-driven DP LEDs currently lag behind with their low EQE. We believe that the EQE could be improved by optimizing the quality and composition of DP thin films. In addition, a better understanding of charge-injection, transport, and recombination in DP systems could help to improve the efficiency of corresponding LEDs.

The early work of Bi-doped luminescent DPs has triggered the development of synthesis methods for strongly emissive colloidal DP NCs with similar chemical composition as the luminescent bulk powders. A wide range of colloidal DP NCs with different stoichiometries has been repotted for tunable emission from visible to infrared either by doping or allowing. Among all, doped/allowed $Cs_2Ag(In_xBi_{1-x})Cl_6$ NCs have received special interest owing to their tunable bandgap by their composition. Various dopants including Mn^{2+} and lanthanides have been exploited to tune their emission wavelength through exciton to dopant emission. Recently, a few reports demonstrated the preparation of 2D DP NPls, however, the level of dimensionality control achieved in DPs is still far from that of LPH NCs. Moreover, the dimensionality-dependent properties are not well investigated in DP NCs. The doped-DP NCs often exhibit relatively low PLQY as compared to their bulk counterparts. This is likely due to incomplete surface passivation of NCs, which results in the formation of trap states. Unlike defect-tolerant LHPs, DPs are prone to surface traps (halide and A-cation vacancies, and ligand detachment) and can greatly influence the radiative recombination and thus PLQY. One needs to understand the surface chemistry of DPs to develop passivation strategies to remove the trap states for improving PLQY. In addition, there is room for the realization of various other DP systems based on co-doping/alloying with various other metal ions. Besides, the DPs, regardless of their PL, are promising for X-ray detectors. A wide range of DPs have been explored for X-ray detection to improve detection sensitivity. It is important to detect low-dose X-rays for biomedical applications and more work is needed in this direction. Furthermore, metal-free halide perovskites such as MDABCO-ammonium trihalide (MDABCO = *N*-methyl-*N*'-diazabicyclo[2.2.2]octonium) have been recently introduced into the perovskite family,[505] yet their potential for optoelectronics is underexplored.[506] Overall, Pb-free perovskites have already shown great promise for optoelectronic and photovoltaic applications, but there is significant room for improving their efficiency as high as that of LHPs.

Acknowledgements

I.L.-F., D.V., C.-Y.W., S.S., T.O., Y.-T.H., K.S., Y.L., V.S.C., J.Z., L.D.T., and D.G. contributed equally to this work. L.P. acknowledges the support from the Spanish Ministerio de Ciencia e Innovación through the Ramón y Cajal grant (RYC2018-026103-I) and the Spanish State Research Agency (Grant No. PID2020-117371RA-I00; TED2021-131628A-100), as well as the grant from the Xunta de Galicia (ED431F2021/05). C.-Y.W. acknowledges the financial support from Alexander von Humboldt Foundation. K.S. acknowledges the financial support from China Scholarship Council (CSC), and P.M.-B. acknowledges support from Deutsche Forschungsgemeinschaft (DFG, German Research Foundation) under Germany's Excellence Strategy – EXC 2089/1–390776260 (e-conversion). V.B. and T.O. acknowledge the MEXT JSPS Grants 20J00974, 21K14580, and 23H01781. H.Z acknowledges the financial supported by NSFC (62222405, 52131304), the Natural Science Foundation of Jiangsu Province (BK20220142), the Fundamental Research Funds for the Central Universities (30922010713), and NSFC-RGC (62261160392). H.-T.S. acknowledges the financial support from JSPS KAKENHI (21H01743). Y.-T.H and R.L.Z.H. would like to thank the Engineering and Physical Sciences Research Council (EPSRC) for funding (no. EP/V014498/2). R.L.Z.H. also thanks the Royal Academy of Engineering through the Research Fellowships scheme (no. RF\201718\17101). D.V. and E.D. acknowledge financial support from the Research Foundation – Flanders through an FWO doctoral fellowship to D.V. (FWO Grant Number 1S45223N) and the KU Leuven Internal Funds (Grant Numbers STG/21/010, C14/23/090, and CELSA/23/018). T.D. acknowledges the Department of Science and Technology (DST) and the Science and Engineering Research Board (SERB) for the Ramanujan Fellowship Award (RJF/2021/000125). I.M.-S. acknowledges Ministry of Science and Innovation of Spain under Step-Up (TED2021-131600B-C31) project and by Generalitat Valenciana under Print-P (MFA/2022/020) project. V.S.C., I.M.-S. and J.P.M.-P acknowledges the support of the Horizon 2020 research and innovation program through the DROP-IT project (grant agreement no. 862656).

Conflict of Interest

The authors declare no conflict of interest.

Keywords

LEDs, nanocrystals, Pb-free perovskites, radiation detectors, solar cells, synthesis, thin films

Received: July 10, 2023
Revised: September 8, 2023
Published online:

[1] A. Kojima, K. Teshima, Y. Shirai, T. Miyasaka, *J. Am. Chem. Soc.* **2009**, *131*, 6050.
[2] A. Dey, J. Ye, A. De, E. Debroye, S. K. Ha, E. Bladt, A S. Kshirsagar, Z. Wang, J. Yin, Y. Wang, Li Na Quan, F. Yan, M. Gao, X. Li, J. Shamsi, T. Debnath, M. Cao, M A. Scheel, S. Kumar, J A. Steele, M. Gerhard, L. Chouhan, Ke Xu, X.-G. Wu, Y. Li, Y. Zhang, A. Dutta, C. Han, I. Vincon, A L. Rogach, et al., *ACS Nano* **2021**, *15*, 10775.
[3] A. K. Jena, A. Kulkarni, T. Miyasaka, *Chem. Rev.* **2019**, *119*, 3036.
[4] J. Y. Kim, J.-W. Lee, H. S. Jung, H. Shin, N.-G. Park, *Chem. Rev.* **2020**, *120*, 7867.
[5] Z. Xiao, Z. Song, Y. Yan, *Adv. Mater.* **2019**, *31*, 1803792.
[6] H. L. Wells, *Zeitschrift für anorganische Chemie* **1893**, *3*, 195.
[7] H. Topsøe, A. Arzruni, G. v. Bath, *Z. Kristallogr.* **1884**, *8*, 246.
[8] A. Kojima, M. Ikegami, K. Teshima, T. Miyasaka, *Chem. Lett.* **2012**, *41*, 397.
[9] Z.-K. Tan, R. S. Moghaddam, M. L. Lai, P. Docampo, R. Higler, F. Deschler, M. Price, A. Sadhanala, L. M. Pazos, D. Credgington, F. Hanusch, T. Bein, H. J. Snaith, R. H. Friend, *Nat. Nanotech.* **2014**, *9*, 687.
[10] I. Chung, B. Lee, J. He, R. P. H. Chang, M. G. Kanatzidis, *Nature* **2012**, *485*, 486.
[11] H.-S. Kim, C.-R. Lee, J.-H. Im, K.-B. Lee, T. Moehl, A. Marchioro, S.-J. Moon, R. Humphry-Baker, J.-H. Yum, J. E. Moser, M. Grätzel, N.-G. Park, *Sci. Rep.* **2012**, *2*, 591.
[12] J. S. Manser, J. A. Christians, P. V. Kamat, *Chem. Rev.* **2016**, *116*, 12956.
[13] J. Fu, S. Ramesh, J. W. Melvin Lim, T. C. Sum, *Chem. Rev.* **2023**, *123*, 8154.
[14] G. Wu, R. Liang, M. Ge, G. Sun, Y. Zhang, G. Xing, *Adv. Mater.* **2022**, *34*, 2105635.
[15] D. B. Mitzi, *Chem. Rev.* **2019**, *119*, 3033.
[16] L. Chouhan, S. Ghimire, C. Subrahmanyam, T. Miyasaka, V. Biju, *Chem. Soc. Rev.* **2020**, *49*, 2869.
[17] H. Lei, D. Hardy, F. Gao, *Adv. Funct. Mater.* **2021**, *31*, 2105898.
[18] M. M. Byranvand, C. Otero-Martínez, J. Ye, W. Zuo, L. Manna, M. Saliba, R. L. Z. Hoye, L. Polavarapu, *Adv. Opt. Mater.* **2022**, *10*, 2200423.

[19] H. Huang, L. Polavarapu, J. A. Sichert, A. S. Susha, A. S. Urban, A. L. Rogach, *NPG Asia Mater.* **2016**, *8*, e328.
[20] Y. Zhao, K. Zhu, *Chem. Soc. Rev.* **2016**, *45*, 655.
[21] J. Park, J. Kim, H.-S. Yun, M. J. Paik, E. Noh, H. J. Mun, M. G. Kim, T. J. Shin, S. I. Seok, *Nature* **2023**, *616*, 724.
[22] S. Castelletto, F. De Angelis, A. Boretti, *Appl. Mater. Today* **2022**, *26*, 101401.
[23] D. Ma, K. Lin, Y. Dong, H. Choubisa, A. H. Proppe, D. Wu, Y.-K. Wang, B. Chen, P. Li, J. Z. Fan, F. Yuan, A. Johnston, Y. Liu, Y. Kang, Z.-H. Lu, Z. Wei, E. H. Sargent, *Nature* **2021**, *599*, 594.
[24] W. Bai, T. Xuan, H. Zhao, H. Dong, X. Cheng, L. Wang, R.-J. Xie, *Adv. Mater.* **2023**, 2302283.
[25] K. Wang, Z.-Y. Lin, Z. Zhang, L. Jin, K. Ma, A. H. Coffey, H. R. Atapattu, Y. Gao, J. Y. Park, Z. Wei, B. P. Finkenauer, C. Zhu, X. Meng, S. N. Chowdhury, Z. Chen, T. Terlier, T.-H. Do, Y. Yao, K. R. Graham, A. Boltasseva, T.-F. Guo, L. Huang, H. Gao, B. M. Savoie, L. Dou, *Nat. Commun.* **2023**, *14*, 397.
[26] R. K. Raman, S. A. Gurusamy Thangavelu, S. Venkataraj, A. Krishnamoorthy, *Renew. Sust. Energ. Rev.* **2021**, *151*, 111608.
[27] F. Gao, Y. Zhao, X. Zhang, J. You, *Adv. Energy Mater.* **2020**, *10*, 1902650.
[28] L. Polavarapu, B. Nickel, J. Feldmann, A. S. Urban, *Adv. Energy Mater.* **2017**, *7*, 1700267.
[29] L. Protesescu, S. Yakunin, M. I. Bodnarchuk, F. Krieg, R. Caputo, C. H. Hendon, R. X. Yang, A. Walsh, M. V. Kovalenko, *Nano Lett.* **2015**, *15*, 3692.
[30] J. Shamsi, A. S. Urban, M. Imran, L. De Trizio, L. Manna, *Chem. Rev.* **2019**, *119*, 3296.
[31] C. Otero-Martínez, D. García-Lojo, I. Pastoriza-Santos, J. Pérez-Juste, L. Polavarapu, *Angew. Chem., Int. Ed.* **2021**, *60*, 26677.
[32] M. Que, L. Zhu, Y. Guo, W. Que, S. Yun, *J. Mater. Chem. C* **2020**, *8*, 5321.
[33] A. Swarnkar, A. R. Marshall, E. M. Sanehira, B. D. Chernomordik, D. T. Moore, J. A. Christians, T. Chakrabarti, J. M. Luther, *Science* **2016**, *354*, 92.
[34] M. Hao, Y. Bai, S. Zeiske, L. Ren, J. Liu, Y. Yuan, N. Zarrabi, N. Cheng, M. Ghasemi, P. Chen, M. Lyu, D. He, J.-H. Yun, Y. Du, Y. Wang, S. Ding, A. Armin, P. Meredith, G. Liu, H.-M. Cheng, L. Wang, *Nat. Energy* **2020**, *5*, 79.
[35] L.-J. Xu, X. Lin, Q. He, M. Worku, B. Ma, *Nat. Commun.* **2020**, *11*, 4329.
[36] H. Wei, J. Huang, *Nat. Commun.* **2019**, *10*, 1066.
[37] Y. Zhou, J. Chen, O. M. Bakr, O. F. Mohammed, *ACS Energy Lett.* **2021**, *6*, 739.
[38] A. Babayigit, A. Ethirajan, M. Muller, B. Conings, *Nat. Mater.* **2016**, *15*, 247.
[39] M. Ren, X. Qian, Y. Chen, T. Wang, Y. Zhao, *J. Hazard. Mater.* **2022**, *426*, 127848.
[40] R. Wang, M. Mujahid, Y. Duan, Z.-K. Wang, J. Xue, Y. Yang, *Adv. Funct. Mater.* **2019**, *29*, 1808843.
[41] C. Otero-Martínez, J. Ye, J. Sung, I. Pastoriza-Santos, J. Pérez-Juste, Z. Xia, A. Rao, R. L. Z. Hoye, L. Polavarapu, *Adv. Mater.* **2022**, *34*, 2107105.
[42] F. Liu, T. Zhang, D. Mondal, S. Teng, Y. Zhang, K. Huang, D. Wang, W. Yang, P. Mahadevan, Y. S. Zhao, R. Xie, N. Pradhan, *Angew. Chem., Int. Ed.* **2021**, *60*, 13548.
[43] S.-J. Woo, J. S. Kim, T.-W. Lee, *Nat. Photonics* **2021**, *15*, 630.
[44] C. C. Boyd, R. Cheacharoen, T. Leijtens, M. D. McGehee, *Chem. Rev.* **2019**, *119*, 3418.
[45] G. Schileo, G. Grancini, *J. Mater. Chem. C* **2021**, *9*, 67.
[46] R. Guo, D. Han, W. Chen, L. Dai, K. Ji, Q. Xiong, S. Li, L. K. Reb, M. A. Scheel, S. Pratap, N. Li, S. Yin, T. Xiao, S. Liang, A. L. Oechsle, C. L. Weindl, M. Schwartzkopf, H. Ebert, P. Gao, K. Wang, M. Yuan, N. C. Greenham, S. D. Stranks, S. V. Roth, R. H. Friend, P. Müller-Buschbaum, *Nat. Energy* **2021**, *6*, 977.
[47] A. H. Slavney, R. W. Smaha, I. C. Smith, A. Jaffe, D. Umeyama, H. I. Karunadasa, *Inorg. Chem.* **2017**, *56*, 46.
[48] V. M. Goldschmidt, *Naturwissenschaften* **1926**, *14*, 477.
[49] C. Li, X. Lu, W. Ding, L. Feng, Y. Gao, Z. Guo, *Acta Crystallogr. B* **2008**, *64*, 702.
[50] G. Kieslich, S. Sun, A. K. Cheetham, *Chem. Sci.* **2015**, *6*, 3430.
[51] W. Travis, E. N. K. Glover, H. Bronstein, D. O. Scanlon, R. G. Palgrave, *Chem. Sci.* **2016**, *7*, 4548.
[52] W. Ke, M. G. Kanatzidis, *Nat. Commun.* **2019**, *10*, 965.
[53] Z. Shi, J. Guo, Y. Chen, Q. Li, Y. Pan, H. Zhang, Y. Xia, W. Huang, *Adv. Mater.* **2017**, *29*, 1605005.
[54] T. C. Jellicoe, J. M. Richter, H. F. J. Glass, M. Tabachnyk, R. Brady, S. E. Dutton, A. Rao, R. H. Friend, D. Credgington, N. C. Greenham, M. L. Böhm, *J. Am. Chem. Soc.* **2016**, *138*, 2941.
[55] Q. Liu, J. Yin, B.-B. Zhang, J.-K. Chen, Y. Zhou, L.-M. Zhang, L.-M. Wang, Q. Zhao, J. Hou, J. Shu, B. Song, N. Shirahata, O. M. Bakr, O. F. Mohammed, H.-T. Sun, *J. Am. Chem. Soc.* **2021**, *143*, 5470.
[56] K. Gahlot, S. de Graaf, H. Duim, G. Nedelcu, R. M. Koushki, M. Ahmadi, D. Gavhane, A. Lasorsa, O. De Luca, P. Rudolf, P. C. A. van der Wel, M. A. Loi, B. J. Kooi, G. Portale, J. Calbo, L. Protesescu, *Adv. Mater.* **2022**, *34*, 2201353.
[57] Z. Wang, F. Wang, B. Zhao, S. Qu, T. Hayat, A. Alsaedi, L. Sui, K. Yuan, J. Zhang, Z. Wei, Z. a. Tan, *J. Phys. Chem. Lett.* **2020**, *11*, 1120.
[58] L. Lanzetta, J. M. Marin-Beloqui, I. Sanchez-Molina, D. Ding, S. A. Haque, *ACS Energy Lett.* **2017**, *2*, 1662.
[59] I. Kopacic, B. Friesenbichler, S. F. Hoefler, B. Kunert, H. Plank, T. Rath, G. Trimmel, *ACS Appl. Energy Mater.* **2018**, *1*, 343.
[60] M. Delor, A. H. Slavney, N. R. Wolf, M. R. Filip, J. B. Neaton, H. I. Karunadasa, N. S. Ginsberg, *ACS Energy Lett.* **2020**, *5*, 1337.
[61] Z. Deng, F. Wei, F. Brivio, Y. Wu, S. Sun, P. D. Bristowe, A. K. Cheetham, *J. Phys. Chem. Lett.* **2017**, *8*, 5015.
[62] T. Tong, C. Liu, J. Xu, H. Min, S. Chen, Y. Lyu, C. Lyu, *J. Mater. Chem. C* **2023**, *11*, 4946.
[63] P. Bhumla, M. Jain, S. Sheoran, S. Bhattacharya, *J. Phys. Chem. Lett.* **2022**, *13*, 11655.
[64] M. Faizan, K. C. Bhamu, G. Murtaza, X. He, N. Kulhari, M. M. Al-Anazy, S. H. Khan, *Sci. Rep.* **2021**, *11*, 6965.
[65] B.-B. Zhang, J.-K. Chen, C. Zhang, N. Shirahata, H.-T. Sun, *ACS Mater. Lett.* **2023**, *5*, 1954.
[66] D. N. Dirin, A. Vivani, M. Zacharias, T. V. Sekh, I. Cherniukh, S. Yakunin, F. Bertolotti, M. Aebli, R. D. Schaller, A. Wieczorek, S. Siol, C. Cancellieri, L. P. H. Jeurgens, N. Masciocchi, A. Guagliardi, L. Pedesseau, J. Even, M. V. Kovalenko, M. I. Bodnarchuk, *Nano Lett.* **2023**, *23*, 1914.
[67] A. B. Wong, Y. Bekenstein, J. Kang, C. S. Kley, D. Kim, N. A. Gibson, D. Zhang, Y. Yu, S. R. Leone, L.-W. Wang, A. P. Alivisatos, P. Yang, *Nano Lett.* **2018**, *18*, 2060.
[68] R. Chiara, Y. O. Ciftci, V. I. E. Queloz, M. K. Nazeeruddin, G. Grancini, L. Malavasi, *J. Phys. Chem. Lett.* **2020**, *11*, 618.
[69] L. Dai, Z. Deng, F. Auras, H. Goodwin, Z. Zhang, J. C. Walmsley, P. D. Bristowe, F. Deschler, N. C. Greenham, *Nat. Photonics* **2021**, *15*, 696.
[70] C. Kang, H. Rao, Y. Fang, J. Zeng, Z. Pan, X. Zhong, *Angew. Chem., Int. Ed.* **2021**, *60*, 660.
[71] L.-M. Wang, J.-K. Chen, B.-B. Zhang, Q. Liu, Y. Zhou, J. Shu, Z. Wang, N. Shirahata, B. Song, O. F. Mohammed, O. M. Bakr, H.-T. Sun, *Nanoscale* **2021**, *13*, 16726.
[72] A. Wang, Y. Guo, F. Muhammad, Z. Deng, *Chem. Mater.* **2017**, *29*, 6493.
[73] W. Gao, C. Ran, J. Xi, B. Jiao, W. Zhang, M. Wu, X. Hou, Z. Wu, *ChemPlusChem* **2018**, *19*, 1696.

[74] M. C. Weidman, M. Seitz, S. D. Stranks, W. A. Tisdale, *ACS Nano* **2016**, *10*, 7830.
[75] A. Wang, Y. Guo, Z. Zhou, X. Niu, Y. Wang, F. Muhammad, H. Li, T. Zhang, J. Wang, S. Nie, Z. Deng, *Chem. Sci.* **2019**, *10*, 4573.
[76] M.-Y. Chen, J.-T. Lin, C.-S. Hsu, C.-K. Chang, C.-W. Chiu, H. M. Chen, P.-T. Chou, *Adv. Mater.* **2018**, *30*, 1706592.
[77] Y. Gao, Z. Wei, P. Yoo, E. Shi, M. Zeller, C. Zhu, P. Liao, L. Dou, *J. Am. Chem. Soc.* **2019**, *141*, 15577.
[78] A. Wang, X. Yan, M. Zhang, S. Sun, M. Yang, W. Shen, X. Pan, P. Wang, Z. Deng, *Chem. Mater.* **2016**, *28*, 8132.
[79] D. S. Dolzhnikov, C. Wang, Y. Xu, M. G. Kanatzidis, E. A. Weiss, *Chem. Mater.* **2017**, *29*, 7901.
[80] D. Shao, W. Zhu, G. Xin, X. Liu, T. Wang, S. Shi, J. Lian, S. Sawyer, *J. Mater. Chem. C* **2020**, *8*, 1819.
[81] J. Chen, Z. Luo, Y. Fu, X. Wang, K. J. Czech, S. Shen, L. Guo, J. C. Wright, A. Pan, S. Jin, *ACS Energy Lett.* **2019**, *4*, 1045.
[82] M. Han, J. Sun, M. Peng, N. Han, Z. Chen, D. Liu, Y. Guo, S. Zhao, C. Shan, T. Xu, X. Hao, W. Hu, Z.-x. Yang, *J. Phys. Chem. C* **2019**, *123*, 17566.
[83] L.-J. Chen, C.-R. Lee, Y.-J. Chuang, Z.-H. Wu, C. Chen, *J. Phys. Chem. Lett.* **2016**, *7*, 5028.
[84] X. Wang, H. Zhou, S. Yuan, W. Zheng, Y. Jiang, X. Zhuang, H. Liu, Q. Zhang, X. Zhu, X. Wang, A. Pan, *Nano Res.* **2017**, *10*, 3385.
[85] L. A. Muscarella, E. M. Hutter, *ACS Energy Lett.* **2022**, *7*, 2128.
[86] Z. Liu, J. Zito, M. Ghini, L. Goldoni, M. Prato, H. Bahmani Jalali, I. Infante, L. De Trizio, L. Manna, *Nano Lett.* **2022**, *22*, 8567.
[87] G. Almeida, L. Goldoni, Q. Akkerman, Z. Dang, A. H. Khan, S. Marras, I. Moreels, L. Manna, *ACS Nano* **2018**, *12*, 1704.
[88] G. Almeida, O. J. Ashton, L. Goldoni, D. Maggioni, U. Petralanda, N. Mishra, Q. A. Akkerman, I. Infante, H. J. Snaith, L. Manna, *J. Am. Chem. Soc.* **2018**, *140*, 14878.
[89] M. Imran, V. Caligiuri, M. Wang, L. Goldoni, M. Prato, R. Krahne, L. De Trizio, L. Manna, *J. Am. Chem. Soc.* **2018**, *140*, 2656.
[90] S. E. Creutz, E. N. Crites, M. C. De Siena, D. R. Gamelin, *Nano Lett.* **2018**, *18*, 1118.
[91] Y. Bekenstein, J. C. Dahl, J. Huang, W. T. Osowiecki, J. K. Swabeck, E. M. Chan, P. Yang, A. P. Alivisatos, *Nano Lett.* **2018**, *18*, 3502.
[92] J. Luo, X. Wang, S. Li, J. Liu, Y. Guo, G. Niu, L. Yao, Y. Fu, L. Gao, Q. Dong, C. Zhao, M. Leng, F. Ma, W. Liang, L. Wang, S. Jin, J. Han, L. Zhang, J. Etheridge, J. Wang, Y. Yan, E. H. Sargent, J. Tang, *Nature* **2018**, *563*, 541.
[93] S. Li, J. Luo, J. Liu, J. Tang, *J. Phys. Chem. Lett.* **2019**, *10*, 1999.
[94] S. Wang, J. Qi, S. V. Kershaw, A. L. Rogach, *ACS Nanosci Au* **2022**, *2*, 93.
[95] D. Zhu, M. L. Zaffalon, J. Zito, F. Cova, F. Meinardi, L. De Trizio, I. Infante, S. Brovelli, L. Manna, *ACS Energy Lett.* **2021**, *6*, 2283.
[96] N. Chen, T. Cai, W. Li, K. Hills-Kimball, H. Yang, M. Que, Y. Nagaoka, Z. Liu, D. Yang, A. Dong, C.-Y. Xu, R. Zia, O. Chen, *ACS Appl. Mater. Interfaces* **2019**, *11*, 16855.
[97] F. Locardi, M. Cirignano, D. Baranov, Z. Dang, M. Prato, F. Drago, M. Ferretti, V. Pinchetti, M. Fanciulli, S. Brovelli, L. De Trizio, L. Manna, *J. Am. Chem. Soc.* **2018**, *140*, 12989.
[98] H. Kim, J. S. Kim, J.-M. Heo, M. Pei, I.-H. Park, Z. Liu, H. J. Yun, M.-H. Park, S.-H. Jeong, Y.-H. Kim, J.-W. Park, E. Oveisi, S. Nagane, A. Sadhanala, L. Zhang, J. J. Kweon, S. K. Lee, H. Yang, H. M. Jang, R. H. Friend, K. P. Loh, M. K. Nazeeruddin, N.-G. Park, T.-W. Lee, *Nat. Commun.* **2020**, *11*, 3378.
[99] W. Lee, S. Hong, S. Kim, *J. Phys. Chem. C* **2019**, *123*, 2665.
[100] Y. Mahor, W. J. Mir, A. Nag, *J. Phys. Chem. C* **2019**, *123*, 15787.
[101] H. Arfin, J. Kaur, T. Sheikh, S. Chakraborty, A. Nag, *Angew. Chem., Int. Ed.* **2020**, *59*, 11307.
[102] D. Manna, T. K. Das, A. Yella, *Chem. Mater.* **2019**, *31*, 10063.
[103] B. Yang, X. Mao, F. Hong, W. Meng, Y. Tang, X. Xia, S. Yang, W. Deng, K. Han, *J. Am. Chem. Soc.* **2018**, *140*, 17001.
[104] B. Yang, F. Hong, J. Chen, Y. Tang, L. Yang, Y. Sang, X. Xia, J. Guo, H. He, S. Yang, W. Deng, K. Han, *Angew. Chem., Int. Ed.* **2019**, *58*, 2278.
[105] A. S. Kshirsagar, A. Nag, *J. Chem. Phys.* **2019**, *151*.
[106] R. S. Lamba, P. Basera, S. Bhattacharya, S. Sapra, *J. Phys. Chem. Lett.* **2019**, *10*, 5173.
[107] T. Wang, Q. Tai, X. Guo, J. Cao, C.-K. Liu, N. Wang, D. Shen, Y. Zhu, C.-S. Lee, F. Yan, *ACS Energy Lett.* **2020**, *5*, 1741.
[108] B. Zhang, M. Wang, M. Ghini, A. E. M. Melcherts, J. Zito, L. Goldoni, I. Infante, M. Guizzardi, F. Scotognella, I. Kriegel, L. De Trizio, L. Manna, *ACS Mater. Lett.* **2020**, *2*, 1442.
[109] P. Han, X. Zhang, C. Luo, W. Zhou, S. Yang, J. Zhao, W. Deng, K. Han, *ACS Cent. Sci.* **2020**, *6*, 566.
[110] F. Locardi, E. Sartori, J. Buha, J. Zito, M. Prato, V. Pinchetti, M. L. Zaffalon, M. Ferretti, S. Brovelli, I. Infante, L. De Trizio, L. Manna, *ACS Energy Lett.* **2019**, *4*, 1976.
[111] Z. Liu, H. Yang, J. Wang, Y. Yuan, K. Hills-Kimball, T. Cai, P. Wang, A. Tang, O. Chen, *Nano Lett.* **2021**, *21*, 1620.
[112] Z. Liu, Y. Sun, T. Cai, H. Yang, J. Zhao, T. Yin, C. Hao, M. Chen, W. Shi, X. Li, L. Guan, X. Li, X. Wang, A. Tang, O. Chen, *Adv. Mater.* **2023**, *35*, 2211235.
[113] B. A. Connor, L. Leppert, M. D. Smith, J. B. Neaton, H. I. Karunadasa, *J. Am. Chem. Soc.* **2018**, *140*, 5235.
[114] J. Huang, S. Zou, J. Lin, Z. Liu, M. Qi, *Nano Res.* **2021**, *14*, 4079.
[115] A. J. Houtepen, Z. Hens, J. S. Owen, I. Infante, *Chem. Mater.* **2017**, *29*, 752.
[116] C. Giansante, I. Infante, *J. Phys. Chem. Lett.* **2017**, *8*, 5209.
[117] N. Fiuza-Maneiro, K. Sun, I. López-Fernández, S. Gómez-Graña, P. Müller-Buschbaum, L. Polavarapu, *ACS Energy Lett.* **2023**, *8*, 1152.
[118] I. Infante, L. Manna, *Nano Lett.* **2021**, *21*, 6.
[119] X. Wang, T. Bai, B. Yang, R. Zhang, D. Zheng, J. Jiang, S. Tao, F. Liu, K.-l. Han, *Nano Lett.* **2022**, *22*, 636.
[120] W. Shockley, H. J. Queisser, *J. Appl. Phys.* **1961**, *32*, 510.
[121] V. I. Klimov, *Annu. Rev. Phys. Chem.* **2007**, *58*, 635.
[122] A. Pandey, P. Guyot-Sionnest, *Science* **2008**, *322*, 929.
[123] R. D. Schaller, V. I. Klimov, *Phys. Rev. Lett.* **2004**, *92*, 186601.
[124] T. R. Hopper, A. Gorodetsky, A. Jeong, F. Krieg, M. I. Bodnarchuk, M. Maimaris, M. Chaplain, T. J. Macdonald, X. Huang, R. Lovrincic, M. V. Kovalenko, A. A. Bakulin, *Nano Lett.* **2020**, *20*, 2271.
[125] H. Chung, S. I. Jung, H. J. Kim, W. Cha, E. Sim, D. Kim, W.-K. Koh, J. Kim, *Angew. Chem., Int. Ed.* **2017**, *56*, 4160.
[126] Y. Li, X. Luo, Y. Liu, X. Lu, K. Wu, *ACS Energy Lett.* **2020**, *5*, 1701.
[127] A. Mondal, J. Aneesh, V. K. Ravi, R. Sharma, W. J. Mir, M. C. Beard, A. Nag, K. V. Adarsh, *Phys. Rev. B* **2018**, *98*.
[128] A. K. Poonia, M. Shrivastava, W. J. Mir, J. Aneesh, A. Nag, K. V. Adarsh, *Phys. Rev. B* **2021**, *104*, L161407.
[129] T. Debnath, D. Sarker, H. Huang, Z. K. Han, A. Dey, L. Polavarapu, S. V. Levchenko, J. Feldmann, *Nat. Commun.* **2021**, *12*, 2629.
[130] G. Kaur, K. J Babu, N. Ghorai, T. Goswami, S. Maiti, H. N. Ghosh, *J. Phys. Chem. Lett.* **2019**, *10*, 5302.
[131] J. Chen, M. E. Messing, K. Zheng, T. Pullerits, *J. Am. Chem. Soc.* **2019**, *141*, 3532.
[132] A. Dey, A. F. Richter, T. Debnath, H. Huang, L. Polavarapu, J. Feldmann, *ACS Nano* **2020**, *14*, 5855.
[133] L. R. V. Buizza, A. D. Wright, G. Longo, H. C. Sansom, C. Q. Xia, M. J. Rosseinsky, M. B. Johnston, H. J. Snaith, L. M. Herz, *ACS Energy Lett.* **2021**, *6*, 1729.
[134] A. D. Wright, L. R. V. Buizza, K. J. Savill, G. Longo, H. J. Snaith, M. B. Johnston, L. M. Herz, *J. Phys. Chem. Lett.* **2021**, *12*, 3352.
[135] B. Wu, W. Ning, Q. Xu, M. Manjappa, M. Feng, S. Ye, J. Fu, S. Lie, T. Yin, F. Wang, T. W. Goh, P. C. Harikesh, Y. K. E. Tay, Z. X. Shen, F. Huang, R. Singh, G. Zhou, F. Gao, T. C. Sum, *Sci. Adv.* **2021**, *7*, eabd3160.

[136] G. W. P. Adhyaksa, L. W. Veldhuizen, Y. Kuang, S. Brittman, R. E. I. Schropp, E. C. Garnett, *Chem. Mater.* **2016**, *28*, 5259.
[137] L. M. Herz, *ACS Energy Lett.* **2017**, *2*, 1539.
[138] A. Barfüßer, S. Rieger, A. Dey, A. Tosun, Q. A. Akkerman, T. Debnath, J. Feldmann, *Nano Lett.* **2022**, *22*, 8810.
[139] R. Ahumada-Lazo, J. A. Alanis, P. Parkinson, D. J. Binks, S. J. O. Hardman, J. T. Griffiths, F. Wisnivesky Rocca Rivarola, C. J. Humphrey, C. Ducati, N. J. L. K. Davis, *J. Phys. Chem. C* **2019**, *123*, 2651.
[140] N. Mondal, A. Samanta, *Nanoscale* **2017**, *9*, 1878.
[141] N. S. Makarov, S. J. Guo, O. Isaienko, W. Y. Liu, I. Robel, V. I. Klimov, *Nano Lett.* **2016**, *16*, 2349.
[142] G. Xing, N. Mathews, S. Sun, S. S. Lim, Y. M. Lam, M. Grätzel, S. Mhaisalkar, T. C. Sum, *Science* **2013**, *342*, 344.
[143] V. I. Klimov, D. W. McBranch, *Phys. Rev. Lett.* **1998**, *80*, 4028.
[144] J. Yang, B.-R. Hyun, A. J. Basile, F. W. Wise, *ACS Nano* **2012**, *6*, 8120.
[145] P. Kambhampati, *Acc. Chem. Res.* **2011**, *44*, 1.
[146] P. Maity, T. Debnath, H. N. Ghosh, *J. Phys. Chem. C* **2015**, *119*, 10785.
[147] P. Maity, S. Maiti, T. Debnath, J. Dana, S. K. Guin, H. N. Ghosh, *J. Phys. Chem. C* **2016**, *120*, 21309.
[148] S. Narra, E. Jokar, O. Pearce, C.-Y. Lin, A. Fathi, E. W.-G. Diau, *J. Phys. Chem. Lett.* **2020**, *11*, 5699.
[149] W. Liang, Y. Li, D. Xiang, Y. Han, Q. Jiang, W. Zhang, K. Wu, *ACS Energy Lett.* **2021**, *6*, 1670.
[150] X.-D. Wang, Y.-H. Huang, J.-F. Liao, Y. Jiang, L. Zhou, X.-Y. Zhang, H.-Y. Chen, D.-B. Kuang, *J. Am. Chem. Soc.* **2019**, *141*, 13434.
[151] J. Almutlaq, W. J. Mir, L. Gutiérrez-Arzaluz, J. Yin, S. Vasylevskyi, P. Maity, J. Liu, R. Naphade, O. F. Mohammed, O. M. Bakr, *ACS Mater. Lett.* **2021**, *3*, 290.
[152] H. Bahmani Jalali, A. Pianetti, J. Zito, M. Imran, M. Campolucci, Y. P. Ivanov, F. Locardi, I. Infante, G. Divitini, S. Brovelli, L. Manna, F. Di Stasio, *ACS Energy Lett.* **2022**, *7*, 1850.
[153] Y. Xu, J. Li, F. Zhao, Y. Gao, R. Chen, T. He, *ACS Omega* **2022**, *7*, 29415.
[154] T. Debnath, S. Maiti, H. N. Ghosh, *J. Phys. Chem. Lett.* **2016**, *7*, 1359.
[155] N. K. Tailor, P. Maity, S. Satapathi, *J. Phys. Chem. Lett.* **2022**, *13*, 5260.
[156] S. Ghimire, C. Rehhagen, S. Fiedler, U. Parekh, R. Lesyuk, S. Lochbrunner, C. Klinke, *Nanoscale* **2023**, *15*, 2096.
[157] Y. He, C. C. Stoumpos, I. Hadar, Z. Luo, K. M. McCall, Z. Liu, D. Y. Chung, B. W. Wessels, M. G. Kanatzidis, *J. Am. Chem. Soc.* **2021**, *143*, 2068.
[158] R. L. Milot, G. E. Eperon, H. J. Snaith, M. B. Johnston, L. M. Herz, *Adv. Funct. Mater.* **2015**, *25*, 6218.
[159] D. H. Kim, J. Park, Z. Li, M. Yang, J.-S. Park, I. J. Park, J. Y. Kim, J. J. Berry, G. Rumbles, K. Zhu, *Adv. Mater.* **2017**, *29*, 1606831.
[160] E. M. Hutter, G. E. Eperon, S. D. Stranks, T. J. Savenije, *J. Phys. Chem. Lett.* **2015**, *6*, 3082.
[161] M. Zhou, J. S. Sarmiento, C. Fei, X. Zhang, H. Wang, *J. Phys. Chem. Lett.* **2020**, *11*, 1502.
[162] G. R. Yettapu, D. Talukdar, S. Sarkar, A. Swarnkar, A. Nag, P. Ghosh, P. Mandal, *Nano Lett.* **2016**, *16*, 4838.
[163] Y. Su, K.-K. Song, M. Zhong, L.-B. Shi, P. Qian, *J. Alloys Compd.* **2021**, *889*, 161723.
[164] Z. Yao, W. Zhao, S. Liu, *J. Mater. Chem. A* **2021**, *9*, 11124.
[165] J. Xing, Y. Zou, C. Zhao, Z. Yu, Y. Shan, W. Kong, X. Zheng, X. Li, W. Yu, C. Guo, *Mater. Today Phys.* **2020**, *14*, 100240.
[166] P. Ščajev, S. Miasojedovas, S. Juršėnas, *J. Mater. Chem. C* **2020**, *8*, 10290.
[167] D. Giovanni, H. Ma, J. Chua, M. Grätzel, R. Ramesh, S. Mhaisalkar, N. Mathews, T. C. Sum, *Nano Lett.* **2015**, *15*, 1553.
[168] W. Rehman, R. L. Milot, G. E. Eperon, C. Wehrenfennig, J. L. Boland, H. J. Snaith, M. B. Johnston, L. M. Herz, *Adv. Mater.* **2015**, *27*, 7938.
[169] R. Ferreira, M. Shaikh, S. K. Jakka, J. Deuermeier, P. Barquinha, S. Ghosh, E. Fortunato, R. Martins, S. Jana, *Nano Lett.* **2022**, *22*, 9020.
[170] Z. Liao, Z. Xiao, M. Yang, M. Zhang, Y. Zhang, H. Gu, X. Jiang, Q. Wang, J. Li, *Appl. Phys. Lett.* **2019**, *115*.
[171] J. Yin, P. Maity, R. Naphade, B. Cheng, J.-H. He, O. M. Bakr, J.-L. Brédas, O. F. Mohammed, *ACS Nano* **2019**, *13*, 12621.
[172] X. Chen, H. Lu, Z. Li, Y. Zhai, P. F. Ndione, J. J. Berry, K. Zhu, Y. Yang, M. C. Beard, *ACS Energy Lett.* **2018**, *3*, 2273.
[173] X. Li, X. Lian, J. Pang, B. Luo, Y. Xiao, M.-D. Li, X.-C. Huang, J. Z. Zhang, *J. Phys. Chem. Lett.* **2020**, *11*, 8157.
[174] R. L. Milot, R. J. Sutton, G. E. Eperon, A. A. Haghighirad, J. Martinez Hardigree, L. Miranda, H. J. Snaith, M. B. Johnston, L. M. Herz, *Nano Lett.* **2016**, *16*, 7001.
[175] W. Guo, Z. Yang, J. Dang, M. Wang, *Nano Energy* **2021**, *86*, 106129.
[176] B. Yang, J. Chen, S. Yang, F. Hong, L. Sun, P. Han, T. Pullerits, W. Deng, K. Han, *Angew. Chem., Int. Ed.* **2018**, *57*, 5359.
[177] W. Ning, F. Wang, B. Wu, J. Lu, Z. Yan, X. Liu, Y. Tao, J.-M. Liu, W. Huang, M. Fahlman, L. Hultman, T. C. Sum, F. Gao, *Adv. Mater.* **2018**, *30*, 1706246.
[178] M. Wang, P. Zeng, S. Bai, J. Gu, F. Li, Z. Yang, M. Liu, *Sol. RRL* **2018**, *2*, 1800217.
[179] R. L. Milot, G. E. Eperon, T. Green, H. J. Snaith, M. B. Johnston, L. M. Herz, *J. Phys. Chem. Lett.* **2016**, *7*, 4178.
[180] Z. Li, P. Wang, C. Ma, F. Igbari, Y. Kang, K.-L. Wang, W. Song, C. Dong, Y. Li, J. Yao, D. Meng, Z.-K. Wang, Y. Yang, *J. Am. Chem. Soc.* **2021**, *143*, 2593.
[181] Q. Sun, Y. Xu, H. Zhang, B. Xiao, X. Liu, J. Dong, Y. Cheng, B. Zhang, W. Jie, M. G. Kanatzidis, *J. Mater. Chem. A* **2018**, *6*, 23388.
[182] K. Yoshikawa, H. Kawasaki, W. Yoshida, T. Irie, K. Konishi, K. Nakano, T. Uto, D. Adachi, M. Kanematsu, H. Uzu, K. Yamamoto, *Nat. Energy* **2017**, *2*, 17032.
[183] X. Liu, T. Wu, X. Luo, H. Wang, M. Furue, T. Bessho, Y. Zhang, J. Nakazaki, H. Segawa, L. Han, *ACS Energy Lett.* **2022**, *7*, 425.
[184] F. Giustino, H. J. Snaith, *ACS Energy Lett.* **2016**, *1*, 1233.
[185] M. Wang, W. Wang, B. Ma, W. Shen, L. Liu, K. Cao, S. Chen, W. Huang, *Nano-Micro Lett.* **2021**, *13*, 62.
[186] T. J. Macdonald, L. Lanzetta, X. Liang, D. Ding, S. A. Haque, *Adv. Mater.* **2021**, *35*, 2206684.
[187] T. Wu, X. Liu, X. Luo, X. Lin, D. Cui, Y. Wang, H. Segawa, Y. Zhang, L. Han, *Joule* **2021**, *5*, 863.
[188] M. Li, F. Li, J. Gong, T. Zhang, F. Gao, W.-H. Zhang, M. Liu, *Small Struct.* **2022**, *3*, 2100102.
[189] D. Cui, X. Liu, T. Wu, X. Lin, X. Luo, Y. Wu, H. Segawa, X. Yang, Y. Zhang, Y. Wang, L. Han, *Adv. Funct. Mater.* **2021**, *31*, 2100931.
[190] B. B. Yu, Z. Chen, Y. Zhu, Y. Wang, B. Han, G. Chen, X. Zhang, Z. Du, Z. He, *Adv. Mater.* **2021**, *33*, 2102055.
[191] P. Wang, F. Li, K.-J. Jiang, Y. Zhang, H. Fan, Y. Zhang, Y. Miao, J.-H. Huang, C. Gao, X. Zhou, F. Wang, L.-M. Yang, C. Zhan, Y. Song, *Adv. Sci.* **2020**, *7*, 1903047.
[192] W. Zhang, Y. Cai, H. Liu, Y. Xia, J. Cui, Y. Shi, R. Chen, T. Shi, H.-L. Wang, *Adv. Energy Mater.* **2022**, *12*, 2202491.
[193] X. Jiang, F. Wang, Q. Wei, H. Li, Y. Shang, W. Zhou, C. Wang, P. Cheng, Q. Chen, L. Chen, Z. Ning, *Nat. Commun.* **2020**, *11*, 1245.
[194] T. Nakamura, S. Yakumaru, M. A. Truong, K. Kim, J. Liu, S. Hu, K. Otsuka, R. Hashimoto, R. Murdey, T. Sasamori, H. D. Kim, H. Ohkita, T. Handa, Y. Kanemitsu, A. Wakamiya, *Nat. Commun.* **2020**, *11*, 3008.
[195] C.-C. Shih, C.-G. Wu, *ACS Appl. Mater. Interfaces* **2022**, *14*, 16125.
[196] G. A. Tosado, E. Zheng, Q. Yu, *Mater. Adv.* **2020**, *1*, 3507.
[197] K. Nishimura, M. A. Kamarudin, D. Hirotani, K. Hamada, Q. Shen, S. Iikubo, T. Minemoto, K. Yoshino, S. Hayase, *Nano Energy* **2020**, *74*, 104858.
[198] T. Krishnamoorthy, H. Ding, C. Yan, W. L. Leong, T. Baikie, Z. Zhang, M. Sherburne, S. Li, M. Asta, N. Mathews, S. G. Mhaisalkar, *J. Mater. Chem. A* **2015**, *3*, 23829.

[199] M. Chen, Q. Dong, C. Xiao, X. Zheng, Z. Dai, Y. Shi, J. M. Luther, N. P. Padture, *ACS Energy Lett.* **2022**, *7*, 2256.
[200] C. H. Ng, K. Hamada, G. Kapil, M. A. Kamarudin, Z. Wang, S. Iikubo, Q. Shen, K. Yoshino, T. Minemoto, S. Hayase, *J. Mater. Chem. A* **2020**, *8*, 2962.
[201] T. Imran, S. Rauf, H. Raza, L. Aziz, R. Chen, S. Liu, J. Wang, M. A. Ahmad, S. Zhang, Y. Zhang, Z. Liu, W. Chen, *Adv. Energy Mater.* **2022**, *12*, 2200305.
[202] J. Cao, F. Yan, *Energy Environ. Mater.* **2021**, *14*, 1286.
[203] S. Tao, I. Schmidt, G. Brocks, J. Jiang, I. Tranca, K. Meerholz, S. Olthof, *Nat. Commun.* **2019**, *10*, 2560.
[204] J. Seo, T. Song, S. Rasool, S. Park, J. Y. Kim, *Adv. Energy Sustain. Res.* **2023**, *4*, 2200160.
[205] F. Hao, C. C. Stoumpos, D. H. Cao, R. P. H. Chang, M. G. Kanatzidis, *Nat. Photonics* **2014**, *8*, 489.
[206] B.-B. Yu, Z. Chen, Y. Zhu, Y. Wang, B. Han, G. Chen, X. Zhang, Z. Du, Z. He, **2021**, *33*, 2102055.
[207] S. J. Lee, S. S. Shin, Y. C. Kim, D. Kim, T. K. Ahn, J. H. Noh, J. Seo, S. I. Seok, *J. Am. Chem. Soc.* **2016**, *138*, 3974.
[208] J. Zillner, H.-G. Boyen, P. Schulz, J. Hanisch, N. Gauquelin, J. Verbeeck, J. Küffner, D. Desta, L. Eisele, E. Ahlswede, M. Powalla, *Adv. Funct. Mater.* **2022**, *32*, 2109649.
[209] B. Li, B. Chang, L. Pan, Z. Li, L. Fu, Z. He, L. Yin, *ACS Energy Lett.* **2020**, *5*, 3752.
[210] C. H. Ng, K. Nishimura, N. Ito, K. Hamada, D. Hirotani, Z. Wang, F. Yang, S. Iikubo, Q. Shen, K. Yoshino, T. Minemoto, S. Hayase, *Nano Energy* **2019**, *58*, 130.
[211] C. J. Bartel, C. Sutton, B. R. Goldsmith, R. Ouyang, C. B. Musgrave, L. M. Ghiringhelli, M. Scheffler, *Sci. Adv.* **2019**, *5*, eaav0693.
[212] A. Yadegarifard, H. Lee, H.-J. Seok, I. Kim, B.-K. Ju, H.-K. Kim, D.-K. Lee, *Nano Energy* **2023**, *112*, 108481.
[213] E. Aktas, N. Rajamanickam, J. Pascual, S. Hu, M. H. Aldamasy, D. Di Girolamo, W. Li, G. Nasti, E. Martínez-Ferrero, A. Wakamiya, E. Palomares, A. Abate, *Commun. Mater.* **2022**, *3*, 104.
[214] D. Wu, P. Jia, W. Bi, Y. Tang, J. Zhang, B. Song, L. Qin, Z. Lou, Y. Hu, F. Teng, Y. Hou, *Org. Electronics* **2020**, *82*, 105728.
[215] L. Zhang, C. Sun, T. He, Y. Jiang, J. Wei, Y. Huang, M. Yuan, *Light Sci Appl* **2021**, *10*, 61.
[216] T. Wang, H.-L. Loi, J. Cao, Z. Qin, Z. Guan, Y. Xu, H. Cheng, M. G. Li, C.-S. Lee, X. Lu, F. Yan, *Adv. Sci.* **2022**, *9*, 2200242.
[217] J. Sanchez-Diaz, R. S. Sánchez, S. Masi, M. Krecmarová, A. O. Alvarez, E. M. Barea, J. Rodriguez-Romero, V. S. Chirvony, J. F. Sánchez-Royo, J. P. Martinez-Pastor, I. Mora-Seró, *Joule* **2022**, *6*, 861.
[218] P. Cheng, T. Wu, J. Liu, W.-Q. Deng, K. Han, *J. Phys. Chem. Lett.* **2018**, *9*, 2518.
[219] X. Yang, W. Wang, R. Ran, W. Zhou, Z. Shao, *Energy Fuels* **2020**, *34*, 10513.
[220] M. T. Sirtl, R. Hooijer, M. Armer, F. G. Ebadi, M. Mohammadi, C. Maheu, A. Weis, B. T. van Gorkom, S. Häringer, R. A. J. Janssen, T. Mayer, V. Dyakonov, W. Tress, T. Bein, *Adv. Energy Mater.* **2022**, *12*, 2103215.
[221] F. Ji, G. Boschloo, F. Wang, F. Gao, *Sol. RRL* **2023**, *7*, 2201112.
[222] M. Zhai, C. Chen, M. Cheng, *Sol. Energy* **2023**, *253*, 563.
[223] Y. Gao, Y. Hu, C. Yao, S. Zhang, *Adv. Funct. Mater.* **2022**, *32*, 2208225.
[224] A. H. Slavney, T. Hu, A. M. Lindenberg, H. I. Karunadasa, *J. Am. Chem. Soc.* **2016**, *138*, 2138.
[225] E. T. McClure, M. R. Ball, W. Windl, P. M. Woodward, *Chem. Mater.* **2016**, *28*, 1348.
[226] G. Volonakis, M. R. Filip, A. A. Haghighirad, N. Sakai, B. Wenger, H. J. Snaith, F. Giustino, *J. Phys. Chem. Lett.* **2016**, *7*, 1254.
[227] A. H. Slavney, L. Leppert, D. Bartesaghi, A. Gold-Parker, M. F. Toney, T. J. Savenije, J. B. Neaton, H. I. Karunadasa, *J. Am. Chem. Soc.* **2017**, *139*, 5015.
[228] Z. Li, S. R. Kavanagh, M. Napari, R. G. Palgrave, M. Abdi-Jalebi, Z. Andaji-Garmaroudi, D. W. Davies, M. Laitinen, J. Julin, M. A. Isaacs, R. H. Friend, D. O. Scanlon, A. Walsh, R. L. Z. Hoye, *J. Mater. Chem. A* **2020**, *8*, 21780.
[229] Y. Sun, A. J. Fernández-Carrión, Y. Liu, C. Yin, X. Ming, B.-M. Liu, J. Wang, H. Fu, X. Kuang, X. Xing, *Chem. Mater.* **2021**, *33*, 5905.
[230] S. Wu, W. Li, J. Hu, P. Gao, *J. Mater. Chem. C* **2020**, *8*, 13603.
[231] C. Zhang, L. Gao, S. Teo, Z. Guo, Z. Xu, S. Zhao, T. Ma, *Sustain. Energy & Fuels* **2018**, *2*, 2419.
[232] F. Wei, Z. Deng, S. Sun, F. Zhang, D. M. Evans, G. Kieslich, S. Tominaka, M. A. Carpenter, J. Zhang, P. D. Bristowe, A. K. Cheetham, *Chem. Mater.* **2017**, *29*, 1089.
[233] Z. Deng, F. Wei, S. Sun, G. Kieslich, A. K. Cheetham, P. D. Bristowe, *J. Mater. Chem. A* **2016**, *4*, 12025.
[234] A. Karmakar, M. S. Dodd, S. Agnihotri, E. Ravera, V. K. Michaelis, *Chem. Mater.* **2018**, *30*, 8280.
[235] T. T. Tran, J. R. Panella, J. R. Chamorro, J. R. Morey, T. M. McQueen, *Mater. Horiz.* **2017**, *4*, 688.
[236] F. Wei, Z. Deng, S. Sun, N. T. P. Hartono, H. L. Seng, T. Buonassisi, P. D. Bristowe, A. K. Cheetham, *Chem. Commun.* **2019**, *55*, 3721.
[237] W. Meng, X. Wang, Z. Xiao, J. Wang, D. B. Mitzi, Y. Yan, *J. Phys. Chem. Lett.* **2017**, *8*, 2999.
[238] G. Volonakis, A. A. Haghighirad, R. L. Milot, W. H. Sio, M. R. Filip, B. Wenger, M. B. Johnston, L. M. Herz, H. J. Snaith, F. Giustino, *J. Phys. Chem. Lett.* **2017**, *8*, 772.
[239] J. Zhou, Z. Xia, M. S. Molokeev, X. Zhang, D. Peng, Q. Liu, *J. Mater. Chem. A* **2017**, *5*, 15031.
[240] J. Luo, S. Li, H. Wu, Y. Zhou, Y. Li, J. Liu, J. Li, K. Li, F. Yi, G. Niu, J. Tang, *ACS Photonics* **2018**, *5*, 398.
[241] H. Yin, Y. Xian, Y. Zhang, W. Chen, X. Wen, N. U. Rahman, Y. Long, B. Jia, J. Fan, W. Li, *Adv. Funct. Mater.* **2020**, *30*, 2002225.
[242] F. Ji, F. Wang, L. Kobera, S. Abbrent, J. Brus, W. Ning, F. Gao, *Chem. Sci.* **2021**, *12*, 1730.
[243] A. H. Slavney, L. Leppert, A. Saldivar Valdes, D. Bartesaghi, T. J. Savenije, J. B. Neaton, H. I. Karunadasa, *Angew. Chem., Int. Ed.* **2018**, *57*, 12765.
[244] M. R. Bhawna, H. B. Vikram, A. Alam, M. Aslam, *Chem. Commun.* **2021**, *57*, 1478.
[245] X. J. Liu, K. Matsuda, Y. Moritomo, A. Nakamura, N. Kojima, *Phys. Rev. B* **1999**, *59*, 7925.
[246] J. Kangsabanik, S. Ghorui, M. Aslam, A. Alam, *Phys. Rev. Appl.* **2020**, *13*, 014005.
[247] B. Ghosh, B. Febriansyah, P. C. Harikesh, T. M. Koh, S. Hadke, L. H. Wong, J. England, S. G. Mhaisalkar, N. Mathews, *Chem. Mater.* **2020**, *32*, 6318.
[248] X. Qiu, Y. Jiang, H. Zhang, Z. Qiu, S. Yuan, P. Wang, B. Cao, *Phys Status Solidi Rapid Res Lett* **2016**, *10*, 587.
[249] X. Qiu, B. Cao, S. Yuan, X. Chen, Z. Qiu, Y. Jiang, Q. Ye, H. Wang, H. Zeng, J. Liu, M. G. Kanatzidis, *Sol. Energy Mater. Sol. Cells* **2017**, *159*, 227.
[250] Y. Jiang, H. Zhang, X. Qiu, B. Cao, *Mater. Lett.* **2017**, *199*, 50.
[251] B. Lee, A. Krenselewski, S. I. Baik, D. N. Seidman, R. P. H. Chang, *Sustainable Energy Fuels* **2017**, *1*, 710.
[252] S. T. Umedov, D. B. Khadka, M. Yanagida, A. Grigorieva, Y. Shirai, *Sol. Energy Mater. Sol. Cells* **2021**, *230*, 111180.
[253] M. Chen, M.-G. Ju, A. D. Carl, Y. Zong, R. L. Grimm, J. Gu, X. C. Zeng, Y. Zhou, N. P. Padture, *Joule* **2018**, *2*, 558.
[254] A. E. Maughan, A. M. Ganose, D. O. Scanlon, J. R. Neilson, *Chem. Mater.* **2019**, *31*, 1184.
[255] E. López-Fraguas, S. Masi, I. Mora-Seró, *ACS Appl. Energy Mater.* **2019**, *2*, 8381.

[256] B. Lee, C. C. Stoumpos, N. Zhou, F. Hao, C. Malliakas, C.-Y. Yeh, T. J. Marks, M. G. Kanatzidis, R. P. H. Chang, *J. Am. Chem. Soc.* **2014**, *136*, 15379.
[257] E. Greul, M L. Petrus, A. Binek, P. Docampo, T. Bein, *J. Mater. Chem. A* **2017**, *5*, 19972.
[258] C. Wu, Q. Zhang, Y. Liu, W. Luo, X. Guo, Z. Huang, H. Ting, W. Sun, X. Zhong, S. Wei, S. Wang, Z. Chen, L. Xiao, *Adv. Sci.* **2018**, *5*, 1700759.
[259] G. Longo, S. Mahesh, L. R. V. Buizza, A. D. Wright, A. J. Ramadan, M. Abdi-Jalebi, P. K. Nayak, L. M. Herz, H. J. Snaith, *ACS Energy Lett.* **2020**, *5*, 2200.
[260] B. Xiao, Y. Tan, Z. Yi, Y. Luo, Q. Jiang, J. Yang, *ACS Appl. Mater. Interfaces* **2021**, *13*, 37027.
[261] P. Hou, W. Yang, N. Wan, Z. Fang, J. Zheng, M. Shang, D. Fu, Z. Yang, W. Yang, *J. Mater. Chem. C* **2021**, *9*, 9659.
[262] N. Daem, J. Dewalque, F. Lang, A. Maho, G. Spronck, C. Henrist, P. Colson, S. D. Stranks, R. Cloots, *Sol. RRL* **2021**, *5*, 2100422.
[263] W. Gao, C. Ran, J. Xi, B. Jiao, W. Zhang, M. Wu, X. Hou, Z. Wu, ChemPhysChem **2018**, *19*, 1696.
[264] X. Yang, Y. Chen, P. Liu, H. Xiang, W. Wang, R. Ran, W. Zhou, Z. Shao, *Adv. Funct. Mater.* **2020**, *30*, 2001557.
[265] B. Wang, N. Li, L. Yang, C. Dall'Agnese, A. K. Jena, T. Miyasaka, X.-F. Wang, *J. Am. Chem. Soc.* **2021**, *143*, 14877.
[266] L. Yang, P. Hou, B. Wang, C. Dall'Agnese, Y. Dall'Agnese, G. Chen, Y. Gogotsi, X. Meng, X.-F. Wang, *Chem. Eng. J.* **2022**, *446*, 136963.
[267] Z. Zhang, Q. Sun, Y. Lu, F. Lu, X. Mu, S.-H. Wei, M. Sui, *Nat. Commun.* **2022**, *13*, 3397.
[268] W. Shockley, H. J. Queisser, *J. Appl. Phys.* **2004**, *32*, 510.
[269] Y. Liu, L. Zhang, M. Wang, Y. Zhong, M. Huang, Y. Long, H. Zhu, *Mater. Today* **2019**, *28*, 25.
[270] A. Kumar, S. K. Swami, S. S. Rawat, V. N. Singh, O. P. Sinha, R. Srivastava, *Int. J. Energy Res.* **2021**, *45*, 16769.
[271] W. Tress, M. T. Sirtl, *Sol. RRL* **2022**, *6*, 2100770.
[272] Z. Yang, Y. Liu, Y. Zhang, L. Wang, C. Lin, Y. Lv, Y. Ma, C. Shao, *J. Phys. Chem. C* **2021**, *125*, 22483.
[273] M. Pantaler, K. T. Cho, V. I. E. Queloz, I. García Benito, C. Fettkenhauer, I. Anusca, M. K. Nazeeruddin, D. C. Lupascu, G. Grancini, *ACS Energy Lett.* **2018**, *3*, 1781.
[274] F. Igbari, R. Wang, Z.-K. Wang, X.-J. Ma, Q. Wang, K.-L. Wang, Y. Zhang, L.-S. Liao, Y. Yang, *Nano Lett.* **2019**, *19*, 2066.
[275] Z. Zhang, C. Wu, D. Wang, Q. Zhang, Y. Zhang, X. Guo, Y. Lao, B. Qu, L. Xiao, Z. Chen, *ACS Appl. Energy Mater.* **2020**, *3*, 9594.
[276] M. Ghasemi, L. Zhang, J.-H. Yun, M. Hao, D. He, P. Chen, Y. Bai, T. Lin, M. Xiao, A. Du, M. Lyu, L. Wang, *Adv. Funct. Mater.* **2020**, *30*, 2002342.
[277] B. Wang, N. Li, L. Yang, C. Dall'Agnese, A. K. Jena, S.-i. Sasaki, T. Miyasaka, H. Tamiaki, X.-F. Wang, *J. Am. Chem. Soc.* **2021**, *143*, 2207.
[278] B. Li, X. Wu, S. Zhang, Z. Li, D. Gao, X. Chen, S. Xiao, C.-C. Chueh, A. K. Y. Jen, Z. Zhu, *Chem. Eng. J.* **2022**, *446*, 137144.
[279] M. Kim, J. Jeong, H. Lu, T. K. Lee, F. T. Eickemeyer, Y. Liu, I. W. Choi, S. J. Choi, Y. Jo, H.-B. Kim, S.-I. Mo, Y.-K. Kim, H. Lee, N. G. An, S. Cho, W. R. Tress, S. M. Zakeeruddin, A. Hagfeldt, J. Y. Kim, M. Grätzel, D. S. Kim, *Science* **2022**, *375*, 302.
[280] D. Zhao, C. Liang, B. Wang, T. Liu, Q. Wei, K. Wang, H. Gu, S. Wang, S. Mei, G. Xing, *Energy Environ. Mater.* **2022**, *5*, 1317.
[281] J. Li, F. Yan, P. Yang, Y. Duan, J. Duan, Q. Tang, *Sol. RRL* **2022**, *6*, 2100791.
[282] L. Lanzetta, T. Webb, J. M. Marin-Beloqui, T. J. Macdonald, S. A. Haque, *Angew. Chem., Int. Ed.* **2023**, *62*, e202213966.
[283] M. L. Lai, T. Y. S. Tay, A. Sadhanala, S. E. Dutton, G. Li, R. H. Friend, Z.-K. Tan, *J. Phys. Chem. Lett.* **2016**, *7*, 2653.
[284] W.-L. Hong, Y.-C. Huang, C.-Y. Chang, Z.-C. Zhang, H.-R. Tsai, N.-Y. Chang, Y.-C. Chao, *Adv. Mater.* **2016**, *28*, 8029.
[285] G. Zhang, S. Xing, X. Cao, B. Zhao, D. Di, *Nanoscale* **2023**, *15*, 6954.
[286] Z. Chen, T. P. Dhakal, *Appl. Phys. Rev.* **2023**, *10*.
[287] W. Ke, C. C. Stoumpos, M. Zhu, L. Mao, I. Spanopoulos, J. Liu, O. Y. Kontsevoi, M. Chen, D. Sarma, Y. Zhang, M. R. Wasielewski, M. G. Kanatzidis, *Sci. Adv.* **2017**, *3*, e1701293.
[288] L. Peedikakkandy, P. Bhargava, *RSC Adv.* **2016**, *6*, 19857.
[289] N. Mondal, A. De, A. Samanta, *ACS Energy Lett.* **2019**, *4*, 32.
[290] Z.-G. Lin, L.-C. Tang, C.-P. Chou, *J. Condens. Matter Phys19* 476209.
[291] L.-C. Tang, Y.-C. Chang, J.-Y. Huang, M.-H. Lee, C.-S. Chang, *Jpn. J. Appl. Phys.* **2009**, *48*, 112402.
[292] S. Yue, S. C. McGuire, H. Yan, Y. S. Chu, M. Cotlet, X. Tong, S. S. Wong, *ACS Omega* **2019**, *4*, 18219.
[293] T. Yokoyama, D. H. Cao, C. C. Stoumpos, T.-B. Song, Y. Sato, S. Aramaki, M. G. Kanatzidis, *J. Phys. Chem. Lett.* **2016**, *7*, 776.
[294] M. Konstantakou, T. Stergiopoulos, *J. Mater. Chem. A* **2017**, *5*, 11518.
[295] M. D. Smith, B. A. Connor, H. I. Karunadasa, *Chem. Rev.* **2019**, *119*, 3104.
[296] J. Li, X. Meng, Z. Wu, Y. Duan, R. Guo, W. Xiao, Y. Zhang, Y. Li, Y. Shen, W. Zhang, G. Shao, *Adv. Funct. Mater.* **2022**, *32*, 2112991.
[297] A. Yangui, D. Garrot, J. S. Lauret, A. Lusson, G. Bouchez, E. Deleporte, S. Pillet, E. E. Bendeif, M. Castro, S. Triki, Y. Abid, K. Boukheddaden, *J. Phys. Chem. C* **2015**, *119*, 23638.
[298] S. R. Rondiya, R. A. Jagt, J. L. MacManus-Driscoll, A. Walsh, R. L. Z. Hoye, *Appl. Phys. Lett.* **2021**, *119*.
[299] Y. Liao, Y. Shang, Q. Wei, H. Wang, Z. Ning, *J. Phys. D: Applied Physics* **2020**, *53*, 414005.
[300] X. Zhang, C. Wang, Y. Zhang, X. Zhang, S. Wang, M. Lu, H. Cui, S. V. Kershaw, W. W. Yu, A. L. Rogach, *ACS Energy Lett.* **2019**, *4*, 242.
[301] J.-T. Lin, C.-C. Liao, C.-S. Hsu, D.-G. Chen, H.-M. Chen, M.-K. Tsai, P.-T. Chou, C.-W. Chiu, *J. Am. Chem.y* **2019**, *141*, 10324.
[302] V. Morad, Y. Shynkarenko, S. Yakunin, A. Brumberg, R. D. Schaller, M. V. Kovalenko, *J. Am. Chem. Soc.* **2019**, *141*, 9764.
[303] G. Vescio, J. Sanchez-Diaz, J. L. Frieiro, R. S. Sánchez, S. Hernández, A. Cirera, I. Mora-Seró, B. Garrido, *ACS Energy Lett.* **2022**, *7*, 3653.
[304] C. Zhou, Y. Tian, M. Wang, A. Rose, T. Besara, N. K. Doyle, Z. Yuan, J. C. Wang, R. Clark, Y. Hu, T. Siegrist, S. Lin, B. Ma, *Angew. Chem., Int. Ed.* **2017**, *56*, 9018.
[305] X. Li, X. Gao, X. Zhang, X. Shen, M. Lu, J. Wu, Z. Shi, V. L. Colvin, J. Hu, X. Bai, W. W. Yu, Y. Zhang, *Adv. Sci.* **2021**, *8*, 2003334.
[306] C. Zhou, Y. Tian, Z. Yuan, H. Lin, B. Chen, R. Clark, T. Dilbeck, Y. Zhou, J. Hurley, J. Neu, T. Besara, T. Siegrist, P. Djurovich, B. Ma, *ACS Appl. Mater. Interfaces* **2017**, *9*, 44579.
[307] B. M. Benin, D. N. Dirin, V. Morad, M. Wörle, S. Yakunin, G. Rainò, O. Nazarenko, M. Fischer, I. Infante, M. V. Kovalenko, *Angew. Chem., Int. Ed.* **2018**, *57*, 11329.
[308] C. Zhou, H. Lin, Y. Tian, Z. Yuan, R. Clark, B. Chen, L. J. van de Burgt, J. C. Wang, Y. Zhou, K. Hanson, Q. J. Meisner, J. Neu, T. Besara, T. Siegrist, E. Lambers, P. Djurovich, B. Ma, *Chem. Sci.* **2018**, *9*, 586.
[309] S. Sun, M. Lu, X. Gao, Z. Shi, X. Bai, W. W. Yu, Y. Zhang, *Adv. Sci.* **2021**, *8*, 2102689.
[310] M. M. S. Karim, A. M. Ganose, L. Pieters, W. W. Winnie Leung, J. Wade, L. Zhang, D. O. Scanlon, R. G. Palgrave, *Chem. Mater.* **2019**, *31*, 9430.
[311] J. Li, Z. Tan, M. Hu, C. Chen, J. Luo, S. Li, L. Gao, Z. Xiao, G. Niu, J. Tang, *Front Optoelectron* **2019**, *12*, 352.
[312] Z. Tan, J. Li, C. Zhang, Z. Li, Q. Hu, Z. Xiao, T. Kamiya, H. Hosono, G. Niu, E. Lifshitz, Y. Cheng, J. Tang, *Adv. Funct. Mater.* **2018**, *28*, 1801131.
[313] E. W. J. L. Oomen, G. J. Dirksen, *Mater. Res. Bull.* **1985**, *20*, 453.
[314] E. W. J. L. Oomen, W. M. A. Smit, G. Blasse, *Met. Phys.* **1986**, *19*, 3263.
[315] W.-L. Hong, P.-H. Lo, H.-Z. Chiu, S.-F. Horng, Y.-C. Chao, *Adv. Mater. Interfaces* **2021**, *8*, 2002240.

[316] J.-M. Heo, H. Cho, S.-C. Lee, M.-H. Park, J. S. Kim, H. Kim, J. Park, Y.-H. Kim, H. J. Yun, E. Yoon, D.-H. Kim, S. Ahn, S.-J. Kwon, C.-Y. Park, T.-W. Lee, *ACS Energy Lett.* **2022**, *7*, 2807.
[317] H. Liang, F. Yuan, A. Johnston, C. Gao, H. Choubisa, Y. Gao, Y.-K. Wang, L. K. Sagar, B. Sun, P. Li, G. Bappi, B. Chen, J. Li, Y. Wang, Y. Dong, D. Ma, Y. Gao, Y. Liu, M. Yuan, M. I. Saidaminov, S. Hoogland, Z.-H. Lu, E. H. Sargent, *Adv. Sci.* **2020**, *7*, 1903213.
[318] C.-F. Lai, Y.-C. Chang, Y.-C. Tien, *ACS Appl. Nano Mater.* **2021**, *4*, 1924.
[319] J. Lu, X. Guan, Y. Li, K. Lin, W. Feng, Y. Zhao, C. Yan, M. Li, Y. Shen, X. Qin, Z. Wei, *Adv. Mater.* **2021**, *33*, 2104414.
[320] S. Ghosh, B. Pradhan, *ChemNanoMat* **2019**, *5*, 300.
[321] M. H. Kumar, S. Dharani, W. L. Leong, P. P. Boix, R. R. Prabhakar, T. Baikie, C. Shi, H. Ding, R. Ramesh, M. Asta, M. Graetzel, S. G. Mhaisalkar, N. Mathews, *Adv. Mater.* **2014**, *26*, 7122.
[322] R. Chiara, M. Morana, L. Malavasi, *ChemPlusChem* **2021**, *86*, 879.
[323] A. Fakharuddin, U. Shabbir, W. Qiu, T. Iqbal, M. Sultan, P. Heremans, L. Schmidt-Mende, *Adv. Mater.* **2019**, *31*, 1807095.
[324] K. P. O. Mahesh, C.-Y. Chang, W.-L. Hong, T.-H. Wen, P.-H. Lo, H.-Z. Chiu, C.-L. Hsu, S.-F. Horng, Y.-C. Chao, *RSC Adv.* **2020**, *10*, 37161.
[325] K. P. Marshall, M. Walker, R. I. Walton, R. A. Hatton, *Nat. Energy* **2016**, *1*, 16178.
[326] R. Lin, K. Xiao, Z. Qin, Q. Han, C. Zhang, M. Wei, M. I. Saidaminov, Y. Gao, J. Xu, M. Xiao, A. Li, J. Zhu, E. H. Sargent, H. Tan, *Nat. Energy* **2019**, *4*, 864.
[327] H. Li, L. Tian, Z. Shi, Y. Li, C. Li, J. Feng, H. Zhang, *J. Mater. Chem. C* **2022**, *10*, 10609.
[328] Y. Zhang, Z. Zhang, W. Yu, Y. He, Z. Chen, L. Xiao, J. j. Shi, X. Guo, S. Wang, B. Qu, *Adv. Sci.* **2022**, *9*, 2102895.
[329] Z. Liu, Y. Sun, T. Cai, H. Yang, J. Zhao, T. Yin, C. Hao, M. Chen, W. Shi, X. Li, *Adv. Mater.* **2023**, 2211235.
[330] J. Nie, B. Zhou, S. Fang, H. Zhong, H. Li, Y. Shi, *Chem. Mater.* **2022**, *34*, 6288.
[331] Y. Chen, R. Zeng, Q. Wei, S. Zhang, B. Luo, C. Chen, X. Zhu, S. Cao, B. Zou, J. Z. Zhang, *J. Phys. Chem. Lett.* **2022**, *13*, 8529.
[332] M. Hu, J. Luo, S. Li, J. Liu, J. Li, Z. Tan, G. Niu, Z. Wang, J. Tang, *Opt. Lett.* **2019**, *44*, 4757.
[333] M. B. Gray, J. D. Majher, T. A. Strom, P. M. Woodward, *Inorganic Chem.* **2019**, *58*, 13403.
[334] Y. Liu, A. Nag, L. Manna, Z. Xia, *Angew. Chem.* **2021**, *133*, 11696.
[335] S. Li, Q. Hu, J. Luo, T. Jin, J. Liu, J. Li, Z. Tan, Y. Han, Z. Zheng, T. Zhai, *Adv. Opt. Mater.* **2019**, *7*, 1901098.
[336] Y. Liu, X. Rong, M. Li, M. S. Molokeev, J. Zhao, Z. Xia, *Angew. Chem., Int. Ed.* **2020**, *59*, 11634.
[337] Y. Liu, M. S. Molokeev, Z. Xia, *Energy Mater. Adv.* **2021**, *2021*.
[338] C.-Y. Wang, P. Liang, R.-J. Xie, Y. Yao, P. Liu, Y. Yang, J. Hu, L. Shao, X. W. Sun, F. Kang, *Chem. Mater.* **2020**, *32*, 7814.
[339] W.-q. Deng, T. Fan, X.-t. Wu, J.-t. Lü, W. Fan, T.-t. Deng, H.-y. He, *Ceram. Int.* **2022**, *48*, 29991.
[340] S. Li, Z. Shi, F. Zhang, L. Wang, Z. Ma, D. Wu, D. Yang, X. Chen, Y. Tian, Y. Zhang, *ACS Appl. Mater. Interfaces* **2020**, *12*, 46330.
[341] Z. Zeng, M. Sun, S. Zhang, H. Zhang, X. Shi, S. Ye, B. Huang, Y. Du, C. H. Yan, *Adv. Funct. Mater.* **2022**, *32*, 2204780.
[342] X. Li, W. Li, M. Xia, C. Liu, N. Li, Z. Shi, Y. Xu, X. Zhang, *Inorganic Chem.* **2022**, *61*, 5040.
[343] A. Zhang, Y. Liu, G. Liu, Z. Xia, *Chem. Mater.* **2022**, *34*, 3006.
[344] J. Zhao, G. Pan, Y. Zhu, K. Liu, W. You, X. Chen, H. Song, Y. Mao, *ACS Appl. Mater. Interfaces* **2022**, *14*, 42215.
[345] Y. Pei, D. Tu, C. Li, S. Han, Z. Xie, F. Wen, L. Wang, X. Chen, *Angew. Chem., Int. Ed.* **2022**, *61*, e202205276.
[346] G. Zhang, P. Dang, H. Lian, H. Xiao, Z. Cheng, J. Lin, *Laser Photonics Rev.* **2022**, *16*, 2200078.
[347] F. Zhao, Z. Song, J. Zhao, Q. Liu, *Inorg. Chem. Front.* **2019**, *6*, 3621.
[348] G. Zhang, D. Wang, B. Lou, C. G. Ma, A. Meijerink, Y. Wang, *Angew. Chem., Int. Ed.* **2022**, *61*, e202207454.
[349] L. Clinckemalie, D. Valli, M. B. J. Roeffaers, J. Hofkens, B. Pradhan, E. Debroye, *ACS Energy Lett.* **2021**, *6*, 1290.
[350] E. C. Lin, *Mayo Clin Proc* **2010**, *85*, 1142.
[351] T. Jin, S. Hao, Y. Shang, Z. Lei, C. Yang, *Crystals* **2022**, *12*, 887.
[352] U. Z. D. Walter, U. Ewert, *e-Journal of Nondestructive Testing* **2016**, *21*, https://www.ndt.net/?id=19252.
[353] A. Waleed, M. M. Tavakoli, L. Gu, Z. Wang, D. Zhang, A. Manikandan, Q. Zhang, R. Zhang, Y.-L. Chueh, Z. Fan, *Nano Lett.* **2017**, *17*, 523.
[354] C.-K. Liu, Q. Tai, N. Wang, G. Tang, H.-L. Loi, F. Yan, *Adv. Sci.* **2019**, *6*, 1900751.
[355] F. Cao, W. Tian, M. Wang, M. Wang, L. Li, *InfoMat* **2020**, *2*, 577.
[356] C.-K. Liu, Q. Tai, N. Wang, G. Tang, Z. Hu, F. Yan, *ACS Appl. Mater. Interfaces* **2020**, *12*, 18769.
[357] A. H. Howlader, F. Li, R. Zheng, *Emergent Mater.* **2022**, *5*, 1925.
[358] L. Qian, Y. Sun, M. Wu, C. Li, D. Xie, L. Ding, G. Shi, *Nanoscale* **2018**, *10*, 6837.
[359] L. Qian, Y. Sun, M. Sun, Z. Fang, L. Li, D. Xie, C. Li, L. Ding, *J. Mater. Chem. C* **2019**, *7*, 5353.
[360] I.-H. Park, L. Chu, K. Leng, Y. F. Choy, W. Liu, I. Abdelwahab, Z. Zhu, Z. Ma, W. Chen, Q.-H. Xu, G. Eda, K. P. Loh, *Adv. Funct. Mater.* **2019**, *29*, 1904810.
[361] R. Saran, R. J. Curry, *Nat. Photonics* **2016**, *10*, 81.
[362] L.-Z. Lei, Z.-F. Shi, Y. Li, Z.-Z. Ma, F. Zhang, T.-T. Xu, Y.-T. Tian, D. Wu, X.-J. Li, G.-T. Du, *J. Mater. Chem. C* **2018**, *6*, 7982.
[363] J. Xiu, Y. Shao, L. Chen, Y. Feng, J. Dai, X. Zhang, Y. Lin, Y. Zhu, Z. Wu, Y. Zheng, H. Pan, C. Liu, X. Shi, X. Cheng, Z. He, *Mater. Today Energy* **2019**, *12*, 186.
[364] C. Wu, B. Du, W. Luo, Y. Liu, T. Li, D. Wang, X. Guo, H. Ting, Z. Fang, S. Wang, Z. Chen, Y. Chen, L. Xiao, *Adv. Opt. Mater.* **2018**, *6*, 1800811.
[365] Y. Li, Z. Shi, L. Lei, S. Li, D. Yang, D. Wu, T. Xu, Y. Tian, Y. Lu, Y. Wang, L. Zhang, X. Li, Y. Zhang, G. Du, C. Shan, *Adv. Mater. Interfaces* **2019**, *6*, 1900188.
[366] J. Yang, C. Bao, W. Ning, B. Wu, F. Ji, Z. Yan, Y. Tao, J.-M. Liu, T. C. Sum, S. Bai, J. Wang, W. Huang, W. Zhang, F. Gao, *Adv. Opt. Mater.* **2019**, *7*, 1801732.
[367] G. Yan, B. Jiang, Y. Yuan, M. Kuang, X. Liu, Z. Zeng, C. Zhao, J.-H. He, W. Mai, *ACS Appl. Mater. Interfaces* **2020**, *12*, 6064.
[368] G. Yan, Z. Ji, Z. Li, B. Jiang, M. Kuang, X. Cai, Y. Yuan, W. Mai, *Sci. China Mater.* **2021**, *64*, 198.
[369] F. Fang, H. Li, S. Fang, B. Zhou, F. Huang, C. Ma, Y. Wan, S. Jiang, Y. Wang, B. Tian, Y. Shi, *Adv. Opt. Mater.* **2021**, *9*, 2001930.
[370] W. Pan, H. Wu, J. Luo, Z. Deng, C. Ge, C. Chen, X. Jiang, W.-J. Yin, G. Niu, L. Zhu, L. Yin, Y. Zhou, Q. Xie, X. Ke, M. Sui, J. Tang, *Nat. Photonics* **2017**, *11*, 726.
[371] L. Yin, H. Wu, W. Pan, B. Yang, P. Li, J. Luo, G. Niu, J. Tang, *Adv. Opt. Mater.* **2019**, *7*, 1900491.
[372] Y. Dang, G. Tong, W. Song, Z. Liu, L. Qiu, L. K. Ono, Y. Qi, *J. Mater. Chem. C* **2020**, *8*, 276.
[373] W. Yuan, G. Niu, Y. Xian, H. Wu, H. Wang, H. Yin, P. Liu, W. Li, J. Fan, *Adv. Funct. Mater.* **2019**, *29*, 1900234.
[374] M. Wang, P. Zeng, Z. Wang, M. Liu, *Adv. Sci.* **2020**, *7*, 1903662.
[375] F. Ji, Y. Huang, F. Wang, L. Kobera, F. Xie, J. Klarbring, S. Abbrent, J. Brus, C. Yin, S. I. Simak, I. A. Abrikosov, I. A. Buyanova, W. M. Chen, F. Gao, *Adv. Funct. Mater.* **2020**, *30*, 2005521.
[376] G. Liu, Z. Zhang, C. Wu, Y. Zhang, X. Li, W. Yu, G. Yao, S. Liu, J.-j. Shi, K. Liu, Z. Chen, L. Xiao, B. Qu, *Adv. Funct. Mater.* **2022**, *32*, 2109891.
[377] Z. Zhang, G. Liu, W. Guo, X. Li, Y. Zhang, C. Wu, B. Qu, J.-j. Shi, Z. Chen, L. Xiao, *Mater. Adv.* **2022**, *3*, 4932.
[378] V. Murgulov, C. Schweinle, M. Daub, H. Hillebrecht, M. Fiederle, V. Dědič, J. Franc, *J. Mater. Sci.* **2022**, *57*, 2758.

[379] H. Zhang, Z. Gao, R. Liang, X. Zheng, X. Geng, Y. Zhao, D. Xie, J. Hong, H. Tian, Y. Yang, X. Wang, T. L. Ren, *IEEE Trans. Electron Devices* **2019**, *66*, 2224.
[380] J. A. Steele, W. Pan, C. Martin, M. Keshavarz, E. Debroye, H. Yuan, S. Banerjee, E. Fron, D. Jonckheere, C. W. Kim, W. Baekelant, G. Niu, J. Tang, J. Vanacken, M. Van der Auweraer, J. Hofkens, M. B. J. Roeffaers, *Adv. Mater.* **2018**, *30*, 1804450.
[381] M. Keshavarz, E. Debroye, M. Ottesen, C. Martin, H. Zhang, E. Fron, R. Küchler, J. A. Steele, M. Bremholm, J. Van de Vondel, H. I. Wang, M. Bonn, M. B. J. Roeffaers, S. Wiedmann, J. Hofkens, *Adv. Mater.* **2020**, *32*, 2001878.
[382] H. Li, X. Shan, J. N. Neu, T. Geske, M. Davis, P. Mao, K. Xiao, T. Siegrist, Z. Yu, *J. Mater. Chem. C* **2018**, *6*, 11961.
[383] B. Yang, W. Pan, H. Wu, G. Niu, J.-H. Yuan, K.-H. Xue, L. Yin, X. Du, X.-S. Miao, X. Yang, Q. Xie, J. Tang, *Nat. Commun.* **2019**, *10*, 1989.
[384] Y. Haruta, S. Wada, T. Ikenoue, M. Miyake, T. Hirato, *Cryst Growth Des* **2021**, *21*, 4030.
[385] N. K. Tailor, J. Ghosh, M. A. Afroz, S. Bennett, M. Chatterjee, P. Sellin, S. Satapathi, *ACS Appl. Electron. Mater.* **2022**, *4*, 4530.
[386] Z. Zhang, D. Cao, Z. Huang, E. O. Danilov, C.-C. Chung, D. Sun, G. Yang, *Adv. Opt. Mater.* **2021**, *9*, 2001575.
[387] L. Clinckemalie, R. A. Saha, D. Valli, E. Fron, M. B. J. Roeffaers, J. Hofkens, B. Pradhan, E. Debroye, *Adv. Opt. Mater. n/a*, 2300578.
[388] Y. Yao, H. Jiang, Y. Peng, X. Zhang, S. Chen, X. Liu, J. Luo, *J. Am. Chem. Soc.* **2021**, *143*, 15900.
[389] W. Li, L. Liu, M. Tan, Y. He, C. Guo, H. Zhang, H. Wei, B. Yang, *Adv. Funct. Mater.* **2021**, *31*, 2107843.
[390] W. Guo, X. Liu, S. Han, Y. Liu, Z. Xu, M. Hong, J. Luo, Z. Sun, *Angew. Chem., Int. Ed.* **2020**, *59*, 13879.
[391] L.-Y. Bi, Y.-Q. Hu, M.-Q. Li, T.-L. Hu, H.-L. Zhang, X.-T. Yin, W.-X. Que, M. S. Lassoued, Y.-Z. Zheng, *J. Mater. Chem. A* **2019**, *7*, 19662.
[392] D. Li, X. Liu, W. Wu, Y. Peng, S. Zhao, L. Li, M. Hong, J. Luo, *Angew. Chem., Int. Ed.* **2021**, *60*, 8415.
[393] W. Zhang, M. Hong, J. Luo, *Angew. Chem., Int. Ed.* **2020**, *59*, 9305.
[394] S. Colella, E. Mosconi, P. Fedeli, A. Listorti, F. Gazza, F. Orlandi, P. Ferro, T. Besagni, A. Rizzo, G. Calestani, G. Gigli, F. De Angelis, R. Mosca, *Chem. Mater.* **2013**, *25*, 4613.
[395] F. Brivio, A. B. Walker, A. Walsh, *APL Mater.* **2013**, *1*.
[396] S. De Wolf, J. Holovsky, S.-J. Moon, P. Löper, B. Niesen, M. Ledinsky, F.-J. Haug, J.-H. Yum, C. Ballif, *J. Phys. Chem. Lett.* **2014**, *5*, 1035.
[397] F. Deschler, M. Price, S. Pathak, L. E. Klintberg, D.-D. Jarausch, R. Higler, S. Hüttner, T. Leijtens, S. D. Stranks, H. J. Snaith, M. Atatüre, R. T. Phillips, R. H. Friend, *J. Phys. Chem. Lett.* **2014**, *5*, 1421.
[398] G. Xing, N. Mathews, S. S. Lim, N. Yantara, X. Liu, D. Sabba, M. Grätzel, S. Mhaisalkar, T. C. Sum, *Nat. Mater.* **2014**, *13*, 476.
[399] R. Dhanker, A. N. Brigeman, A. V. Larsen, R. J. Stewart, J. B. Asbury, N. C. Giebink, *Appl. Phys. Lett.* **2014**, *105*.
[400] Q. Zhang, R. Su, W. Du, X. Liu, L. Zhao, S. T. Ha, Q. Xiong, *Small Methods* **2017**, *1*, 1700163.
[401] M. A. Green, A. Ho-Baillie, H. J. Snaith, *Nat. Photonics* **2014**, *8*, 506.
[402] I. Suárez, J. P. Martínez Pastor, in *Halide Perovskites for Photonics*, (Eds: A. Vinattieri, G. Giorgi), AIP Publishing LLC, United States, 0, https://doi.org/10.1063/9780735423633_007.
[403] H. Zhu, Y. Fu, F. Meng, X. Wu, Z. Gong, Q. Ding, M. V. Gustafsson, M. T. Trinh, S. Jin, X. Y. Zhu, *Nat. Mater.* **2015**, *14*, 636.
[404] Z. Liu, J. Yang, J. Du, Z. Hu, T. Shi, Z. Zhang, Y. Liu, X. Tang, Y. Leng, R. Li, *ACS Nano* **2018**, *12*, 5923.
[405] H. Zhou, S. Yuan, X. Wang, T. Xu, X. Wang, H. Li, W. Zheng, P. Fan, Y. Li, L. Sun, A. Pan, *ACS Nano* **2017**, *11*, 1189.
[406] Y. Mi, Z. Liu, Q. Shang, X. Niu, J. Shi, S. Zhang, J. Chen, W. Du, Z. Wu, R. Wang, X. Qiu, X. Hu, Q. Zhang, T. Wu, X. Liu, *Small* **2018**, *14*, 1703136.
[407] L. Yang, Z. Li, C. Liu, X. Yao, H. Li, X. Liu, J. Liu, P. Zhu, B. Liu, T. Cui, C. Sun, Y. Bao, *J. Phys. Chem. Lett.* **2019**, *10*, 7056.
[408] Q. Zhang, S. T. Ha, X. Liu, T. C. Sum, Q. Xiong, *Nano Lett.* **2014**, *14*, 5995.
[409] I. Suárez, E. J. Juárez-Pérez, V. S. Chirvony, I. Mora-Seró, J. P. Martínez-Pastor, *Phys Rev* **2020**, *13*, 064071.
[410] S. Chen, C. Zhang, J. Lee, J. Han, A. Nurmikko, *Adv. Mater.* **2017**, *29*, 1604781.
[411] S. Chen, A. Nurmikko, *ACS Photonics* **2017**, *4*, 2486.
[412] S. Chen, A. Nurmikko, *Optica* **2018**, *5*, 1141.
[413] Y. Wang, X. Li, V. Nalla, H. Zeng, H. Sun, *Adv. Funct. Mater.* **2017**, *27*, 1605088.
[414] N. Pourdavoud, T. Haeger, A. Mayer, P. J. Cegielski, A. L. Giesecke, R. Heiderhoff, S. Olthof, S. Zaefferer, I. Shutsko, A. Henkel, D. Becker-Koch, M. Stein, M. Cehovski, O. Charfi, H.-H. Johannes, D. Rogalla, M. C. Lemme, M. Koch, Y. Vaynzof, K. Meerholz, W. Kowalsky, H.-C. Scheer, P. Görrn, T. Riedl, *Adv. Mater.* **2019**, *31*, 1903717.
[415] T. Byrnes, N. Y. Kim, Y. Yamamoto, *Nat. Phys.* **2014**, *10*, 803.
[416] R. Su, C. Diederichs, J. Wang, T. C. H. Liew, J. Zhao, S. Liu, W. Xu, Z. Chen, Q. Xiong, *Nano Lett.* **2017**, *17*, 3982.
[417] M. Saliba, S. M. Wood, J. B. Patel, P. K. Nayak, J. Huang, J. A. Alexander-Webber, B. Wenger, S. D. Stranks, M. T. Hörantner, J. T.-W. Wang, R. J. Nicholas, L. M. Herz, M. B. Johnston, S. M. Morris, H. J. Snaith, M. K. Riede, *Adv. Mater.* **2016**, *28*, 923.
[418] P. Su, Y. Liu, J. Zhang, C. Chen, B. Yang, C. Zhang, X. Zhao, *J. Phys. Chem. Lett.* **2020**, *11*, 2812.
[419] C. C. Stoumpos, C. D. Malliakas, M. G. Kanatzidis, *Inorganic Chem.* **2013**, *52*, 9019.
[420] Y. Wang, R. Zou, J. Chang, Z. Fu, Y. Cao, L. Zhang, Y. Wei, D. Kong, W. Zou, K. Wen, N. Fan, N. Wang, W. Huang, J. Wang, *J. Phys. Chem. Lett.* **2019**, *10*, 453.
[421] Y. Takahashi, H. Hasegawa, Y. Takahashi, T. Inabe, *J. Solid State Chem.* **2013**, *205*, 39.
[422] N. K. Noel, S. D. Stranks, A. Abate, C. Wehrenfennig, S. Guarnera, A.-A. Haghighirad, A. Sadhanala, G. E. Eperon, S. K. Pathak, M. B. Johnston, L. M. Herz, H. J. Snaith, *Energy Environ. Mater.* **2014**, *7*, 3061.
[423] G. I. Peters, L. Allen, *J. Phys. A: General Phys.* **1971**, *4*, 238.
[424] T. Burgess, D. Saxena, S. Mokkapati, Z. Li, C. R. Hall, J. A. Davis, Y. Wang, L. M. Smith, L. Fu, P. Caroff, H. H. Tan, C. Jagadish, *Nat. Commun.* **2016**, *7*, 11927.
[425] G. Xing, M. H. Kumar, W. K. Chong, X. Liu, Y. Cai, H. Ding, M. Asta, M. Grätzel, S. Mhaisalkar, N. Mathews, T. C. Sum, *Adv. Mater.* **2016**, *28*, 8191.
[426] P. Ščajev, C. Qin, R. n. Aleksiejūnas, P. Baronas, S. Miasojedovas, T. Fujihara, T. Matsushima, C. Adachi, S. Juršėnas, *J. Phys. Chem. Lett.* **2018**, *9*, 3167.
[427] R. L. Milot, M. T. Klug, C. L. Davies, Z. Wang, H. Kraus, H. J. Snaith, M. B. Johnston, L. M. Herz, *Adv. Mater.* **2018**, *30*, 1804506.
[428] E. S. Parrott, R. L. Milot, T. Stergiopoulos, H. J. Snaith, M. B. Johnston, L. M. Herz, *J. Phys. Chem. Lett.* **2016**, *7*, 1321.
[429] R. A. n. P. Ščajev, P. Baronas, D. Litvinas, M. Kolenda, C. Qin, T. Fujihara, T. Matsushima, C. Adachi, S. Juršeňas, *J. Phys. Chem. C* **2019**, *123*, 19275.
[430] Z. Y. Wu, Y. Y. Chen, L.-J. Lin, H.-C. Hsu, *J. Phys. Chem. C* **2021**, *125*, 5180.
[431] V. S. Chirvony, I. Suárez, J. Sanchez-Diaz, R. S. Sánchez, J. Rodríguez-Romero, I. Mora-Seró, J. P. Martínez-Pastor, *Adv. Mater.* **2023**, *35*, 2208293.
[432] I. Suárez, V. S. Chirvony, J. Sánchez-Díaz, R. S. Sánchez, I. Mora-Seró, J. P. Martínez-Pastor, *Adv. Opt. Mater.* **2022**, *10*, 2200458.
[433] H. Cao, X. Jiang, Y. Ling, J. Y. Xu, C. M. Soukoulis, *Phys. Rev. B* **2003**, *67*, 161101.
[434] X. Jiang, S. Feng, C. M. Soukoulis, J. Zi, J. D. Joannopoulos, H. Cao, *Phys. Rev. B* **2004**, *69*, 104202.

[435] Y. Liu, W. Yang, S. Xiao, N. Zhang, Y. Fan, G. Qu, Q. Song, *ACS Nano* **2019**, *13*, 10653.
[436] R. Vidal, J. A. Alberola-Borràs, N. Sánchez-Pantoja, I. Mora-Seró, *Adv. Energy Sustain. Res.* **2021**, *2*, 2000088.
[437] M. V. Khenkin, E. A. Katz, A. Abate, G. Bardizza, J. J. Berry, C. Brabec, F. Brunetti, V. Bulović, Q. Burlingame, A. Di Carlo, *Nat. Energy* **2020**, *5*, 35.
[438] Y. Zhao, F. Ma, Z. Qu, S. Yu, T. Shen, H.-X. Deng, X. Chu, X. Peng, Y. Yuan, X. Zhang, *Science* **2022**, *377*, 531.
[439] B. B. Yu, Z. Chen, Y. Zhu, Y. Wang, B. Han, G. Chen, X. Zhang, Z. Du, Z. He, *Adv. Mater.* **2021**, *33*, 2102055.
[440] R. Szostak, A. de Souza Gonçalves, J. N. de Freitas, P. E. Marchezi, F. L. de Araújo, H. C. N. Tolentino, M. F. Toney, F. das Chagas Marques, A. F. Nogueira, *Chem. Rev.* **2023**, *123*, 3160.
[441] P. Müller-Buschbaum, *Adv. Mater.* **2014**, *26*, 7692.
[442] N. Li, S. Pratap, V. Körstgens, S. Vema, L. Song, S. Liang, A. Davydok, C. Krywka, P. Müller-Buschbaum, *Nat. Commun.* **2022**, *13*, 6701.
[443] X. Meng, X. Tian, S. Zhang, J. Zhou, Y. Zhang, Z. Liu, W. Chen, *Sol. RRL* **2022**, *6*, 2200280.
[444] O. Dyck, M. Ziatdinov, D. B. Lingerfelt, R. R. Unocic, B. M. Hudak, A. R. Lupini, S. Jesse, S. V. Kalinin, *Nat. Rev. Mater.* **2019**, *4*, 497.
[445] T. Kirchartz, J. A. Márquez, M. Stolterfoht, T. Unold, *Adv. Energy Mater.* **2020**, *10*, 1904134.
[446] C. Cho, S. Feldmann, K. M. Yeom, Y.-W. Jang, S. Kahmann, J.-Y. Huang, T. C. J. Yang, M. N. T. Khayyat, Y.-R. Wu, M. Choi, *Nat. Mater.* **2022**, 1.
[447] M. Qin, P. F. Chan, X. Lu, *Adv. Mater.* **2021**, *33*, 2105290.
[448] Q. Wang, B. Chen, Y. Liu, Y. Deng, Y. Bai, Q. Dong, J. Huang, *Energy Environ. Mater.* **2017**, *10*, 516.
[449] J. S. Yun, J. Kim, T. Young, R. J. Patterson, D. Kim, J. Seidel, S. Lim, M. A. Green, S. Huang, A. Ho-Baillie, *Adv. Funct. Mater.* **2018**, *28*, 1705363.
[450] V. J. Y. Lim, A. M. Ulatowski, C. Kamaraki, M. T. Klug, L. M Perez, M. B. Johnston, L. M. Herz, *Adv. Energy Mater.* **2022**, *n/a*, 2200847.
[451] M. I. Saidaminov, J. Kim, A. Jain, R. Quintero-Bermudez, H. Tan, G. Long, F. Tan, A. Johnston, Y. Zhao, O. Voznyy, *Nat. Energy* **2018**, *3*, 648.
[452] Y. Liu, K. Palotas, X. Yuan, T. Hou, H. Lin, Y. Li, S.-T. Lee, *ACS Nano* **2017**, *11*, 2060.
[453] Y.-H. Kye, C.-J. Yu, U.-G. Jong, Y. Chen, A. Walsh, *J. Phys. Chem. Lett.* **2018**, *9*, 2196.
[454] E. Mosconi, J. M. Azpiroz, F. De Angelis, *Chem. Mater.* **2015**, *27*, 4885.
[455] K. Sun, P. Müller-Buschbaum, *Energy Technol.* **2023**, *11*, 2201475.
[456] B. Kim, S. I. Seok, *Energy Environ. Mater.* **2020**, *13*, 805.
[457] C. Otero-Martínez, N. Fiuza-Maneiro, L. Polavarapu, *ACS Appl. Mater. Interfaces* **2022**, *14*, 34291.
[458] Z. Li, F. Zhou, Q. Wang, L. Ding, Z. Jin, *Nano Energy* **2020**, *71*, 104634.
[459] Z. Qiu, N. Li, Z. Huang, Q. Chen, H. Zhou, *Small Methods* **2020**, *4*, 1900877.
[460] Z. Lin, M. C. Folgueras, H. K. Le, M. Gao, P. Yang, *Matter* **2022**, *5*, 1455.
[461] J. Lin, M. Lai, L. Dou, C. S. Kley, H. Chen, F. Peng, J. Sun, D. Lu, S. A. Hawks, C. Xie, *Nat. Mater.* **2018**, *17*, 261.
[462] C. Ma, F. T. Eickemeyer, S.-H. Lee, D.-H. Kang, S. J. Kwon, M. Grätzel, N.-G. Park, *Science* **2023**, *379*, 173.
[463] Q. Sun, P. Fassl, D. Becker-Koch, A. Bausch, B. Rivkin, S. Bai, P. E. Hopkinson, H. J. Snaith, Y. Vaynzof, *Adv. Energy Mater.* **2017**, *7*, 1700977.
[464] N. Aristidou, C. Eames, I. Sanchez-Molina, X. Bu, J. Kosco, M. S. Islam, S. A. Haque, *Nat. Commun.* **2017**, *8*, 15218.
[465] A. J. Pearson, G. E. Eperon, P. E. Hopkinson, S. N. Habisreutinger, J. T. W. Wang, H. J. Snaith, N. C. Greenham, *Adv. Energy Mater.* **2016**, *6*, 1600014.
[466] N. Aristidou, I. Sanchez-Molina, T. Chotchuangchutchaval, M. Brown, L. Martinez, T. Rath, S. A. Haque, *Angew. Chem.* **2015**, *127*, 8326.
[467] Y. Ouyang, L. Shi, Q. Li, J. Wang, *Small Methods* **2019**, *3*, 1900154.
[468] S. Kundu, T. L. Kelly, *EcoMat* **2020**, *2*, e12025.
[469] G. Divitini, S. Cacovich, F. Matteocci, L. Cinà, A. Di Carlo, C. Ducati, *Nat. Energy* **2016**, *1*, 15012.
[470] L. Lanzetta, T. Webb, N. Zibouche, X. Liang, D. Ding, G. Min, R. J. Westbrook, B. Gaggio, T. J. Macdonald, M. S. Islam, *Nat. Commun.* **2021**, *12*, 2853.
[471] L. H Hernandez, L. Lanzetta, S. Jang, J. Troughton, M. A. Haque, D. Baran, *ACS Energy Lett.* **2022**, *8*, 259.
[472] T. Leijtens, R. Prasanna, A. Gold-Parker, M. F. Toney, M. D. McGehee, *ACS Energy Lett.* **2017**, *2*, 2159.
[473] X. Guan, J. Lu, Q. Wei, Y. Li, Y. Meng, K. Lin, Y. Zhao, W. Feng, K. Liu, G. Xing, *ACS Energy Lett.* **2023**, *8*, 1597.
[474] Z. Li, J. Ji, C. Zhang, Q. Hou, P. Jin, *J. Phys. Chem. C* **2020**, *124*, 14147.
[475] D. Meggiolaro, D. Ricciarelli, A. A. Alasmari, F. A. Alasmary, F. De Angelis, *J. Phys. Chem. Lett.* **2020**, *11*, 3546.
[476] K. J. Savill, A. M. Ulatowski, L. M. Herz, *ACS Energy Lett.* **2021**, *6*, 2413.
[477] D. Ricciarelli, D. Meggiolaro, F. Ambrosio, F. De Angelis, *ACS Energy Lett.* **2020**, *5*, 2787.
[478] K. J. Savill, A. M. Ulatowski, M. D. Farrar, M. B. Johnston, H. J. Snaith, L. M. Herz, *Adv. Funct. Mater.* **2020**, *30*, 2005594.
[479] D. J. Kubicki, D. Prochowicz, E. Salager, A. Rakhmatullin, C. P. Grey, L. Emsley, S. D. Stranks, *J. Am. Chem. Soc.* **2020**, *142*, 7813.
[480] G. Xie, L. Xu, L. Sun, Y. Xiong, P. Wu, B. Hu, *J. Mater. Chem. A* **2019**, *7*, 5779.
[481] W. Kaiser, D. Ricciarelli, E. Mosconi, A. A. Alothman, F. Ambrosio, F. De Angelis, *J. Phys. Chem. Lett.* **2022**, *13*, 2321.
[482] L. Lanzetta, N. Aristidou, S. A. Haque, *J. Phys. Chem. Lett.* **2020**, *11*, 574.
[483] E. Jokar, C.-H. Chien, A. Fathi, M. Rameez, Y.-H. Chang, E. W.-G. Diau, *Energy Environ. Mater.* **2018**, *11*, 2353.
[484] X. Xu, C.-C. Chueh, Z. Yang, A. Rajagopal, J. Xu, S. B. Jo, A. K.-Y. Jen, *Nano Energy* **2017**, *34*, 392.
[485] W. Gao, C. Ran, J. Li, H. Dong, B. Jiao, L. Zhang, X. Lan, X. Hou, Z. Wu, *J. Phys. Chem. Lett.* **2018**, *9*, 6999.
[486] W. Peng, J. Yin, K.-T. Ho, O. Ouellette, M. De Bastiani, B. Murali, O. El Tall, C. Shen, X. Miao, J. Pan, *Nano Lett.* **2017**, *17*, 4759.
[487] Y. Liao, H. Liu, W. Zhou, D. Yang, Y. Shang, Z. Shi, B. Li, X. Jiang, L. Zhang, L. N. Quan, *J. Am. Chem. Soc.* **2017**, *139*, 6693.
[488] R. M. I. Bandara, S. M. Silva, C. C. Underwood, K. I. Jayawardena, R. A. Sporea, S. R. P. Silva, *Energy Environ. Mater.* **2022**, *5*, 370.
[489] S. Gu, R. Lin, Q. Han, Y. Gao, H. Tan, J. Zhu, *Adv. Mater.* **2020**, *32*, 1907392.
[490] L. E. Mundt, J. Tong, A. F. Palmstrom, S. P. Dunfield, K. Zhu, J. J. Berry, L. T. Schelhas, E. L. Ratcliff, *ACS Energy Lett.* **2020**, *5*, 3344.
[491] Y. Xing, Z. Deng, T. Guo, Z. Zhang, Q. Tai, R. Zhao, J. Xiong, Q. Wang, L. Huang, X. Liu, *Chem. Eng. J.* **2023**, 142122.
[492] Y. She, Z. Hou, O. V. Prezhdo, W. Li, *J. Phys. Chem. Lett.* **2021**, *12*, 10581.
[493] Z. Xiao, K.-Z. Du, W. Meng, J. Wang, D. B. Mitzi, Y. Yan, *J. Am. Chem. Soc.* **2017**, *139*, 6054.
[494] A. C. Dakshinamurthy, C. Sudakar, *Mater. Adv.* **2022**, *3*, 5813.
[495] H. Li, C. Pi, W. Chen, M. Zhou, J. Wei, J. Yi, P. Song, Y. Alexey, Y. Zhong, X. Yu, *J. Phys. Chem. Lett.* **2021**, *12*, 5682.
[496] N. Li, X. Niu, Q. Chen, H. Zhou, *Chem. Soc. Rev.* **2020**, *49*, 8235.
[497] Q. Dong, L. Lei, J. Mendes, F. So, *J. Phys. Mater.* **2020**, *3*, 012002.
[498] B. Roose, Q. Wang, A. Abate, *Adv. Energy Mater.* **2019**, *9*, 1803140.

[499] R. Prasanna, T. Leijtens, S. P. Dunfield, J. A. Raiford, E. J. Wolf, S. A. Swifter, J. Werner, G. E. Eperon, C. de Paula, A. F. Palmstrom, *Nat. Energy* **2019**, *4*, 939.
[500] M. De Jong, L. Van Ijzendoorn, M. De Voigt, *Appl. Phys. Lett.* **2000**, *77*, 2255.
[501] S.-H. Li, Z. Xing, B.-S. Wu, Z.-C. Chen, Y.-R. Yao, H.-R. Tian, M.-F. Li, D.-Q. Yun, L.-L. Deng, S.-Y. Xie, *ACS Appl. Mater. Interfaces* **2020**, *12*, 20733.
[502] P. Hang, J. Xie, C. Kan, B. Li, Y. Zhang, P. Gao, D. Yang, X. Yu, *Adv. Mater.* **2021**, *33*, 2006910.
[503] K. Zhang, K. Forberich, L. Lüer, J. G. Cerrillo, W. Meng, X. Du, V. M. Le Corre, Y. Zhao, T. Niu, Q. Xue, *Adv. Energy and Sustain. Res.* **2022**, *3*, 2100156.
[504] W. Bai, T. Xuan, H. Zhao, H. Dong, X. Cheng, L. Wang, R.-J. Xie, *Adv. Mater.* **2023**, *n/a*, 2302283.
[505] H.-Y. Ye, Y.-Y. Tang, P.-F. Li, W.-Q. Liao, J.-X. Gao, X.-N. Hua, H. Cai, P.-P. Shi, Y.-M. You, R.-G. Xiong, *Science* **2018**, *361*, 151.
[506] R. Taheri-Ledari, F. Ganjali, S. Zarei-Shokat, M. Saeidirad, F. Ansari, M. Forouzandeh-Malati, F. Hassanzadeh-Afruzi, S. M. Hashemi, A. Maleki, *Energy Fuels* **2022**, *36*, 10702.

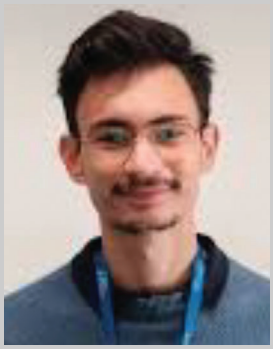

Iago López-Fernández obtained Master's degree from the University of Vigo and the University of Santiago. Currently, he is a Ph.D. student in Materials Chemistry and Physics group and his research is focused on the synthesis and modulation of doped perovskite nanoparticles for their use in LEDs, solar cells, and infrared detectors.

Donato Valli received his M.Sc. degree in chemistry in 2019 from the University of Padua. Currently, he holds a FWO fellowship and is pursuing his Ph.D. within the Molecular Imaging and Photonics group at KU Leuven. His research is centered around the rational design, synthesis, and advanced structural and optical characterization of new lead-free halide perovskite semiconductors towards better performing X-rays and photodetectors.

Chun-Yun Wang is currently a Humboldt Research Fellow at the Institute for Photovoltaics, University of Stuttgart. She obtained her Ph.D. at Hokkaido University. Afterward, she worked at Tshinghua University as a postdoctoral researcher and Peking University as a research scientist, respectively. Her research focuses on the development of novel lead-free perovskite materials and high-performance optoelectronic devices (LED, photodetector and solar cell).

Subarna Samanta received his M.Sc. degree in chemistry from the National Institute of Technology Durgapur. He is currently working as a JRF (Adhoc) project fellow under Dr. Tushar Debnath at the Center for Nanotechnology in the Indian Institute of Technology Guwahati. Currently, his research work focused on the synthesis and optical properties of perovskite nanocrystals for photocatalytic application.

Takuya Okamoto received his Ph. D. degree in molecular materials science from the Graduate School of Science, Osaka City University, Japan, in 2020 under the guidance of Prof. Tomoyuki Yatsuhashi. During this period, he was the recipient of the JSPS Doctoral Fellowship. Subsequently, he was a JSPS Postdoctoral Fellow with Prof. Biju at Hokkaido University, becoming an assistant professor at the Research Institute for Electronic Science in December 2022.

Yi-Teng Huang is currently a postdoctoral researcher at Department of Chemistry of University of Oxford, under the supervision of Prof. Robert Hoye. He completed his Ph.D. in physics at University of Cambridge (2019–2023) before joining Prof. Robert Hoye's group at Oxford. His research interests include understanding the mechanism behind defect tolerance, charge-carrier phonon coupling, charge-carrier dynamics, and developing optoelectronic devices based on novel semiconductors.

Kun Sun is presently a Ph.D. student at the School of Natural Sciences, Technical University of Munich, under the supervision of Professor Peter Müller-Buschbaum. His current research is related to the growth of perovskite films and degradation mechanisms of perovskite solar cells.

Yang Liu is presently a Ph.D. student at the School of Materials Science and Engineering, Nanjing University of Science and Technology, under the supervision of Professor Haibo Zeng and Xiaoming Li. Currently, she is a visiting student in Materials Chemistry and Physics group at the University of Vigo. Her current research is related to the synthesis of DBSA-based $CsPbBr_3$ QDs and lead-free double perovskites.

Vladimir Chirvony, graduated from the Physical Department of the Belarus State University, Minsk. Further worked in the field of molecular photophysics at the Institute of Physics of the Academy of Sciences of Belarus, and since 2009 at the Institute of Material Sciences at the University of Valencia, Spain, in the field of photophysics and optical spectroscopy of semiconductor nanostructures.

Deepika Gaur is currently research assistant in Materials Chemistry and Physics group at the University of Vigo, Spain. She received her Ph.D. in 2023 from NorthCap University, India and M.Sc. degree in physics in 2014 from the J.C. Bose University of Science and Technology University, India. Her research is focused on halide perovskite nanocrystal optoelectronics (Solar cells and LEDs).

Hong-Tao Sun is a principal researcher at Research Center for Materials Nanoarchitectonics (MANA), National Institute for Materials Science (NIMS), Japan. He obtained his Ph.D. in materials science in 2007 from the Chinese Academy of Sciences. His research interests include the synthesis of colloidal nanocrystals, structural chemistry of functional materials, and optoelectronics.

Zhiguo Xia is a professor at the South China University of Technology. He obtained his Bachelor's and Master's degrees from Beijing Technology and Business University, and received his PhD degree from Tsinghua University in 2008. His research interests include the discovery of new rare earth phosphors for LED applications as well as the discovery of new luminescent metal halides for emerging phonic applications.

Xiaoming Li received his Bachelor's and Ph.D. degrees in material science from Nanjing University of Aeronautics and Astronautics in 2013 and 2017, respectively. Now, he is a professor of Nanjing University of Science and Technology. His current research interests include synthesis and optoelectronic applications of all-inorganic halide perovskite nanocrystals.

Haibo Zeng obtained his Ph.D. in material physics from the Institute of Solid State Physics in the Chinese Academy of Sciences in 2006. Following being a visiting scholar at the University of Karlsruhe (with Prof. Claus Kling Shirn and Prof. Heinz Kalt) and then postdoctoral work at the National Institute for Materials Science (with Prof. Yoshio Bando and Prof. Dmitri Golberg), he joined the Nanjing University of Science and Technology in 2011 and initiated the Institute of Optoelectronics & Nanomaterials. His research interests are focused on exploratory design of semiconducting NCs and 2D crystals, with an emphasis on optoelectronic applications.

Iván Mora-Seró (Ph.D. Physics 2004) is professor at Universitat Jaume I de Castelló (Spain). His research is focused on crystal growth, nanostructured devices, transport and recombination properties, photocatalysis, characterization and development of photovoltaic and optoelectronic devices. Recent research activities are focused on new concepts for photovoltaic conversion and light emission (LEDs and light amplifiers) based on nanoscaled devices and semiconductor materials following two main lines: semiconductor quantum dots and halide perovskites, focusing recently on the development of Pb-free systems.

Juan P. Martínez-Pastor is PhD in physics, full professor and director of the Institute of Materials Science at the University of Valencia (ICMUV). Along his career he has launched several research labs at ICMUV, supervised 20 PhDs and published more than 300 papers (235 papers in JCR journals), six monographs and one edited book. He has recognized experience & expertise in semiconductor physics, single quantum dot spectroscopy and single photon, optical sensors based on colloidal metal nanoparticles and quantum dots, photonic waveguide structures, photodetectors based on quantum dots and perovskites, 2D-semiconductors and metal halide perovskites. He has led more than 30 research projects, among regionals, nationals and Europeans (recently coordinator of DROP-IT project: *DRop-on demand flexible Optoelectronics & Photovoltaics by means of Lead-Free halide perovskITes*).

Peter Müller-Buschbaum is full professor in the School of Natural Sciences at Technical University of Munich, Germany, heading the Chair of Functional Materials. Moreover, he is the scientific director of the Munich neutron source FRM II, scientific director of the Heinz Maier Leibnitz Zentrum MLZ and heading the Bavarian key lab TUM.solar. His research interests cover polymer and hybrid materials for energy and sensing applications with a special focus on thin films and nanostructures, including kinetic, in situ, and operando experiments.

Vasudevanpillai Biju is a professor at the Research Institute for Electronic Science at Hokkaido University. He assumed this position after a research career—as a scientist and a senior scientist in AIST, Japan, a PRESTO researcher at Japan Science and Technology Agency (JST), a visiting Scientist at the University of Texas at Austin, USA, a postdoctoral fellow at Pacific Northwest National Laboratory, USA, and a JSPS postdoctoral fellow and a research scientist at AIST, Japan. He was/has been an associate editor of *J. Photochem. Photobiol. C* and *NPG Asia Materials*. His research interests include semiconductor nanomaterials and quantum dots, photo-functional molecules, and single-molecule techniques.

Tushar Debnath is presently working as a principle investigator at the Centre for Nanotechnology, IIT Guwahati, India. He obtained his Ph.D. in chemistry in 2016 from BARC, Mumbai, India. Subsequently, he moved to NTU, Singapore (2016–2018) as a postdoctoral fellow followed by LMU, Munich, Germany (2018 – 2022) with Alexander von Humboldt fellowship. He was optical spectroscopy group leader at the department of physics, LMU from 2019 to 2022, and then he started his independent research group at IIT Guwahati, India (2022–present) with Ramanujan fellowship. Dr. Debnath is an expert in the field of ultrafast spectroscopy. With the state-of-the-art optical spectroscopic setup, he investigates the fundamental photophysics of several nanocrystal materials to small molecules, primarily for energy-related applications. He has co-authored 55 publications in the international journal of reputes.

Michael Saliba is the director of the Institute for Photovoltaics (IPV) at the University of Stuttgart with a dual appointment as the Helmholtz Young Investigator at the Forschungszentrum Jülich, Germany. His research focuses on a deeper fundamental understanding and improvement of optoelectronic properties of emerging photovoltaic materials with an emphasis on perovskites for a sustainable energy future. Previously, he held positions at TU Darmstadt, University of Fribourg, and EPFL. He obtained his Ph.D. at Oxford University. Among others, he received the Heinz-Maier-Leibnitz Award of the German Research Foundation and was names as one of the worldwide 35 innovators under 35 by the MIT Technology Review.

Elke Debroye obtained her Ph.D. in 2013, on developing MRI/optical contrast agents in the Laboratory of Bio-inorganic Chemistry, KU Leuven. After postdoctoral stays with Prof. Liz-Marzán in San Sebastian (Spain), Prof. Majima at Osaka University (Japan) and Prof. Bonn at MPI Mainz (Germany), she returned to the Laboratory of Photochemistry and Spectroscopy, KU Leuven. Currently, she is an assistant Professor exploring new (lead-free) perovskite structures with advanced structural and optical characterization techniques, and consequently optimizing their performance toward their application in new generation optoelectronics, with a special focus on radiation detection.

Robert L. Z. Hoye is an associate professor in the Department of Chemistry at the University of Oxford. There, he also holds a Royal Academy of Engineering Research Fellowship, and is a Fellow of St. John's College. He completed his PhD at the University of Cambridge (2012–2014), before working as a postdoctoral researcher at the Massachusetts Institute of Technology (2015–2016). He subsequently received two College Research Fellowships at Cambridge, firstly at Magdalene College (2016–2019), then at Downing College (2019–2020), before taking up a Lectureship at Imperial College London in 2020. He moved to Oxford in 2022. His research focusses on defect-tolerant semiconductors, and their development into optoelectronic devices.

Liberato Manna obtained his Bachelor degree in chemistry in 1996 from the University of Bari and the Ph.D. in Chemistry in 2001 from the same University, and worked at UC Berkeley (USA) as a visiting Student (1999-2000) and subsequently at the Lawrence Berkeley Lab (USA) as a postdoctoral fellow (2001-2003). He then started his career as independent PI at the National Nanotechnology Lab in Lecce (Italy, 2003–2009) and later moved to the Istituto Italiano di Tecnologia (IIT), Genova (Italy) as head of the Nanochemistry Group. Since 2016 he regularly teaches at the University of Genova. Since 2015, he is also associate director of IIT for the Materials and Nanotechnology programs. His research interests include the synthesis and assembly of colloidal nanocrystals, the structural, chemical and surface transformations in nanoscale materials, and their applications in energy, photonics, and electronics.

Lakshminarayana Polavarapu is the principal investigator of the Materials Chemistry and Physics Research group at the Centro De Investigaciones Biomédicas (CINBIO), University of Vigo. He obtained an M.Sc. in Chemistry from the University of Hyderabad (India) and Ph.D. from the National University of Singapore. After being a postdoctoral fellow at CIC biomaGUNE and University of Vigo in Spain, he joined the Chair for Photonics and Optoelectronics at the Ludwig-Maximilians-University of Munich (Germany) as an Alexander von Humboldt postdoctoral fellow and later continued as a junior group leader until May 2020. His research interests include shape-controlled synthesis and self-assembly of metal and semiconductor nanocrystals for exploring their optical properties and optoelectronic applications.